JGR Planets

RESEARCH ARTICLE
10.1029/2025JE009556

Special Collection:
Aeolian-Fluvial Interactions across the Solar System

An Aeolian Depositional Sequence Shaped by Near-Surface Water at the Base of the Layered Sulfate Unit, Gale Crater, Mars

Amelie L. Roberts[1], Sanjeev Gupta[1], Aster Cowart[2], Lauren A. Edgar[3], William Rapin[4], William E. Dietrich[5], Edwin Kite[6], Steven G. Banham[1], Joel M. Davis[1], Claire A. Mondro[7], Dave M. Rubin[8], John P. Grotzinger[7], William Farrand[9], Linda Kah[2], Kevin Lewis[10], Alexander Bryk[5], Catherine Weitz[11], Rachel Y. Sheppard[11], Gwénaël Caravaca[4], Stéphane Le Mouélic[12], Emma R. Harris[1,13], Patrick J. Gasda[14], Aileen Yingst[15], Deirdra Fey[15], Jeffrey R. Johnson[16], Gerhard P. Paar[17], Abigail A. Fraeman[18], and Ashwin R. Vasavada[18]

[1]Department of Earth Science & Engineering, Imperial College London, London, UK, [2]Planetary Science Institute, Tucson, AZ, USA, [3]NASA Johnson Space Centre, Houston, TX, USA, [4]Institut de Recherche en Astrophysique et Planétologie (IRAP), UMR 5277, Université Paul Sabatier Toulouse III, CNRS, CNES, Toulouse, France, [5]Department of Earth & Planetary Science, University of California, Berkeley, CA, USA, [6]Department of Geophysical Sciences, University of Chicago, Chicago, IL, USA, [7]Division of Geological and Planetary Sciences, California Institute of Technology, Pasadena, CA, USA, [8]Department of Earth and Planetary Sciences, University of California, Santa Cruz, CA, USA, [9]Space Science Institute, Boulder, CO, USA, [10]Earth and Planetary Sciences, Johns Hopkins University, Baltimore, MD, USA, [11]University of Tennessee Knoxville, Knoxville, TN, USA, [12]Laboratoire de Planétologie et Géosciences, Nantes, France, [13]Department of Earth Sciences, Natural History Museum, London, UK, [14]Los Alamos National Laboratory, Los Alamos, NM, USA, [15]Malin Space Science Systems, San Diego, CA, USA, [16]Johns Hopkins University Applied Physics Laboratory, Laurel, MD, USA, [17]JOANNEUM RESEARCH Institute for Information- and Communication Technology, Graz, Austria, [18]Jet Propulsion Laboratory, California Institute of Technology, Pasadena, CA, USA

Key Points:

- The basal section of the Layered Sulfate unit in Gale crater records a transition from aeolian dunes to sandsheet depositional environments
- The tabular geometry, extent, and the intermittent damp and wet conditions suggest that the sandsheets were controlled by near-surface water
- Aeolian sand sheet deposition under these conditions likely required a continuously rising water table during their formation in the Hesperian

Supporting Information:

Supporting Information may be found in the online version of this article.

Correspondence to:

A. L. Roberts,
arobe116@jh.edu

Citation:

Roberts, A. L., Gupta, S., Cowart, A., Edgar, L. A., Rapin, W., Dietrich, W. E., et al. (2026). An aeolian depositional sequence shaped by near-surface water at the base of the layered sulfate unit, Gale crater, Mars. *Journal of Geophysical Research: Planets*, *131*, e2025JE009556. https://doi.org/10.1029/2025JE009556

Received 14 NOV 2025
Accepted 20 APR 2026

Author Contributions:

Conceptualization: Amelie L. Roberts, Sanjeev Gupta, Lauren A. Edgar, William E. Dietrich, Edwin Kite, Steven G. Banham, Dave M. Rubin, John P. Grotzinger, William Farrand, Abigail A. Fraeman, Ashwin R. Vasavada
Data curation: Amelie L. Roberts, Aster Cowart, Lauren A. Edgar, William Rapin, William E. Dietrich, Edwin Kite, Claire A. Mondro, Linda Kah, Kevin Lewis, Alexander Bryk,

Abstract The basal strata of the orbitally defined Layered Sulfate unit (LSu) in Gale crater, Mars, marks the end of a major mineralogical transition from clay-to sulfate-bearing stratigraphy. This has previously been attributed to a period of significant aridification of Gale's climate. Here, we present ground-based observations by the Curiosity rover of the sedimentary facies and architecture of the basal strata of the LSu, and reconstruct the past depositional environments. The succession predominantly comprises four members of the Mirador formation: the Contigo, Catrimani, Amapari, and Chenapau members. The Contigo member records the migration of simple aeolian dunes. The Catrimani and Chenapau members record a facies characteristic of wind-ripple migration in aeolian sand sheets. Periodic damp sand sheet deposition is inferred through candidate adhesion structures and evaporite crystals. Evidence for periodic surface water occurs as lacustrine deposits (the Amapari member) and an embedded fluvial lens. Near-surface water likely restricted the availability of loose sediment, suppressing dune formation and promoting the accumulation of a thick sandsheet succession that, at ~60 m, exceeds known terrestrial equivalents. Deposition under these conditions would have required a continuously rising water table, but the rate of sediment accumulation was likely high enough for a predominantly aeolian environment. Contrary to earlier aridification models for the LSu, this basal succession likely records an overall aeolian environment controlled by a rising water table in Gale crater during the Hesperian.

Plain Language Summary The base of the Layered Sulfate unit (LSu) in Gale crater reflects a major change in surface minerals, from clay-bearing rocks to sulfate-bearing ones. This transition has been thought to record the long-term drying of Gale's climate. Using data from NASA's Curiosity rover, we describe the first detailed view of ~100 m of this sedimentary rock and reconstruct Gale crater's regional climate at the time of the LSu's formation. These rocks comprise four members of the Mirador formation: the Contigo, Catrimani, Amapari, and Chenapau members. Most of this succession was built by wind. The Contigo member records small migrating desert dunes. The overlying Catrimani and Chenapau members record a flat-lying desert environment called a sand sheet. The Amapari member records a shallow lake environment, showing that water was once present at the surface. We also find evidence that the sand sheet was periodically damp, suggesting a near-surface and fluctuating water table. These damp conditions likely limited the supply of loose sand, allowing a thick desert sand sheet to accumulate instead of large dunes—thicker than any known example on

Catherine Weitz, Rachel Y. Sheppard, Gwénaël Caravaca, Stéphane Le Mouélic, Patrick J. Gasda, Aileen Yingst, Deirdra Fey, Jeffrey R. Johnson, Gerhard P. Paar, Abigail A. Fraeman, Ashwin R. Vasavada
Formal analysis: Amelie L. Roberts, Sanjeev Gupta, Aster Cowart, Lauren A. Edgar, Edwin Kite, Steven G. Banham, Claire A. Mondro, Dave M. Rubin, John P. Grotzinger, William Farrand, Linda Kah, Kevin Lewis, Alexander Bryk, Catherine Weitz, Patrick J. Gasda, Abigail A. Fraeman, Ashwin R. Vasavada
Funding acquisition: Sanjeev Gupta
Investigation: Amelie L. Roberts, Sanjeev Gupta, Aster Cowart, Lauren A. Edgar, William Rapin, William E. Dietrich, Edwin Kite, Steven G. Banham, Joel M. Davis, Claire A. Mondro, Dave M. Rubin, John P. Grotzinger, William Farrand, Linda Kah, Kevin Lewis, Alexander Bryk, Catherine Weitz, Rachel Y. Sheppard, Gwénaël Caravaca, Emma R. Harris, Patrick J. Gasda, Aileen Yingst, Deirdra Fey, Jeffrey R. Johnson, Gerhard P. Paar, Abigail A. Fraeman, Ashwin R. Vasavada
Methodology: Amelie L. Roberts, Sanjeev Gupta, Aster Cowart, William E. Dietrich, Steven G. Banham, William Farrand, Abigail A. Fraeman, Ashwin R. Vasavada
Project administration: Abigail A. Fraeman, Ashwin R. Vasavada
Resources: Amelie L. Roberts, Sanjeev Gupta, Aster Cowart, Lauren A. Edgar, William E. Dietrich, Linda Kah, Kevin Lewis, Alexander Bryk, Catherine Weitz, Rachel Y. Sheppard, Gwénaël Caravaca, Stéphane Le Mouélic, Aileen Yingst, Deirdra Fey, Jeffrey R. Johnson, Gerhard P. Paar, Abigail A. Fraeman, Ashwin R. Vasavada
Supervision: Sanjeev Gupta, Steven G. Banham, Joel M. Davis
Visualization: Amelie L. Roberts, Sanjeev Gupta
Writing – original draft: Amelie L. Roberts
Writing – review & editing: Amelie L. Roberts, Sanjeev Gupta, Lauren A. Edgar, William Rapin, Edwin Kite, Steven G. Banham, Joel M. Davis, Claire A. Mondro, Dave M. Rubin, John P. Grotzinger, William Farrand, Rachel Y. Sheppard, Gwénaël Caravaca, Stéphane Le Mouélic, Emma R. Harris, Patrick J. Gasda, Ashwin R. Vasavada

Earth. Overall, this part of the LSu records alternating dry and damp conditions, when the water table was likely rising in Gale crater.

1. Introduction

Across Mars, younger, sulfate-bearing sedimentary rocks are often found to overlie older, clay-bearing sedimentary rocks from orbit (e.g., Ehlmann & Edwards, 2014), leading to a hypothesis that a global change in climate, associated with the aridification of Mars, caused this broad shift in mineralogy (e.g., Bibring et al., 2006; Ehlmann & Edwards, 2014). Sedimentary rocks are the only physical record available to understand how Mars evolved from a once "warm and wet" paleoclimate, potentially suitable for supporting life, to the "cold and dry" climate present on Mars today (Fairén, 2010; Grotzinger et al., 2014; Hurowitz et al., 2017; Malin & Edgett, 2000). Aeolis Mons—the central mound within Gale crater—hosts an exceptional example of a clay-bearing to sulfate-bearing sedimentary succession (Fraeman et al., 2016; Milliken et al., 2014; Sheppard et al., 2021) which was one of the reasons why Gale crater was selected as the landing site for the Mars Science Laboratory (MSL)'s rover *Curiosity* (Golombek et al., 2012). A central goal of the mission is to use *Curiosity* to test whether this shift in minerology is linked to an overall aridification of the region and whether habitable environments could persist through periods of climate change (e.g., Golombek et al., 2012; Milliken et al., 2010; Vasavada, 2022). Rover observations of lacustrine and fluvial deposits in the clay-bearing unit, and aeolian deposits with interbedded fluvial/lacustrine lenses in a mixed clay–sulfate unit, support this overall regional "drying out" (Caravaca et al., 2022a, 2022b, 2025; Edgar et al., 2020; Grotzinger et al., 2014; Gupta, Dietrich, Lewis, Mondro, et al., 2023; Rivera-Hernández et al., 2019; Stack et al., 2019).

The orbitally defined Layered Sulfate unit (LSu) which forms part of this succession is composed of distinct, planar-parallel, laterally extensive layers that are visible from orbit (e.g., Anderson & Bell, 2010; Fraeman et al., 2016), analogous to other thick successions of layered sulfate terrain across Mars (Gendrin et al., 2005). Multiple formational mechanisms–from depositional processes to diagenesis post-dating lithification–have been suggested to explain both the minerology and appearance of these layered sulfates (e.g., Ehlmann & Edwards, 2014; Gendrin et al., 2005). In 2022, *Curiosity* explored the basal section of the LSu in a canyon where a ∼100 m thick succession is exposed in local buttes. This stratigraphic succession represents an ideal location to study the depositional environments at the base of the LSu because of the excellent outcrop exposures of the sedimentary architecture and the lateral continuity of the layers across the rover's traverse, allowing for on-ground facies characterization.

The aim of this work was to reconstruct the depositional processes and environments that created the sedimentary succession of the basal section of the layered sulfate-bearing unit. The main objectives are to: (a) describe and characterize the sedimentary structures, facies, and architecture recorded in the basal section of the Layered Sulfate unit; (b) reconstruct the depositional processes and environments for each member; (c) evaluate the evolution of these depositional environments over the formation of this succession; and (d) discuss the implications for the formation of the layered sulfate-bearing unit at Gale crater and their broader regional significance.

2. Geologic Context

Gale crater (Figure 1a) is a partially infilled impact crater approximately ∼155 km in diameter, located within the heavily cratered southern highlands near the dichotomy boundary with the comparatively smoother northern lowlands. Crater counting of its ejecta blanket places its formation at around 3.7–3.8 billion years (Ga) during the Noachian-Hesperian transition period (e.g., Le Deit et al., 2013; Thomson et al., 2011). Following its formation, Gale was progressively infilled by sedimentary deposits over a 200–500 million year (Myr) period (e.g., Grant et al., 2014; Thomson et al., 2011), punctuated by several episodes of aeolian erosion (Dromart et al., 2021). The infilling material in Gale crater was later exhumed by predominantly aeolian processes (Anderson & Day, 2017; Day & Kocurek, 2016; Grotzinger et al., 2015; Kite, Lewis, et al., 2013; Malin & Edgett, 2000), leaving behind the ∼5.5 km tall central mound, Aeolis Mons. This mound, informally known as "Mount Sharp," is comprised of distinctive layered stratigraphy (Anderson & Bell, 2010; Malin & Edgett, 2000; Figure 1a). Reflectance spectral data from orbit indicate a transition up-section from clay-bearing to layered sulfate-bearing strata, which are themselves unconformably overlain by anhydrous mineral-bearing strata (Figure 1b; Fraeman et al., 2016;

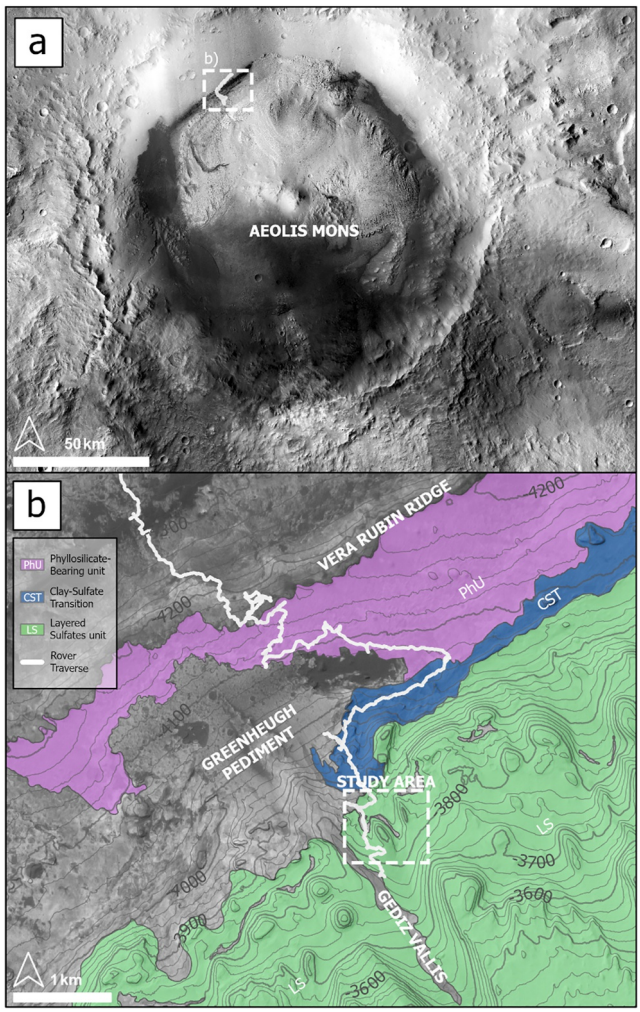

Figure 1. (a) A Mars Reconnaissance Orbiter (MRO) Context Camera (CTX) mosaic (~5 m per pixel resolution; Dickson et al., 2018) showing the regional context of Gale crater and Aeolis Mons. White dashed box shows the Curiosity's rover's exploration extent. (b) The CTX mosaic overlain by a Mars Orbital Laser Altimeter (MOLA) and High Resolution Imaging Science Experiment (HiRISE) derived Digital Terrain Model (DTM) hillshade (~1 m per pixel resolution; Calef & Parker, 2016; Smith et al., 2001) shows the local extent of Curiosity's traverse within Gale crater (Sols 3576 to Sol 3749. Mapped major Mount Sharp orbital units modified from Fraeman et al. (2016) on the northern flank of Aeolis Mons are displayed for context. White dashed box shows the study area at the base of the layered sulfates within Marker Band valley (sols 3576 to 3749). Image credit: NASA/JPL/MSSS/The Murray Lab.

Milliken et al., 2014). This clay-to-sulfate transition is found to be a spatially variable and inconsistent gradational boundary, with discontinuous inclusions of clay-bearing strata amongst the layered sulfate-bearing strata in further orbital studies (Sheppard et al., 2021).

By August 2025, *Curiosity* had traversed over 850 m of vertical stratigraphy since its landing in August 2012 (Figure 2). Three major stratigraphic groups have been documented at the time of writing: the Bradbury, Mount Sharp, and Siccar Point groups. The Bradbury group consists of fluvial sandstones and conglomerates outcropping across the crater floor and the lower slopes of the mound (Aeolis Palus; Rice et al., 2017; Stack et al., 2016; Vasavada, 2022; Williams et al., 2013). The Bradbury group is inferred to interfinger with strata of the Mount Sharp group (Grotzinger et al., 2015). The Mount Sharp group consists of stratigraphy which bears hydrated minerals identified from orbit prior to landing (e.g., Milliken et al., 2010). These groups are unconformably overlain by the Siccar Point group. The Stimson formation (Banham et al., 2022; Watkins et al., 2022) and Long Valley formations (Figure 2) are the only units assigned to the Siccar Point group so far (Figure 2). The Stimson formation is composed of large-scale aeolian cross-bedded units indicating an arid desert environment (Banham et al., 2018), although minor soft sediment deformation structures show that near-surface fluid was locally present before lithification (Banham et al., 2024b) and chemical and mineralogic evidence show that fluids persisted long after deposition (e.g., Bedford et al., 2020). The Long Valley formation is composed of variably consolidated gravel and boulders attributed to debris flows and dry granular flows (Davis et al., 2025; Dietrich et al., 2024).

The Mount Sharp group is comprised of three formations (Figure 2). The Murray formation is comprised of clay-bearing strata with lacustrine mudstones and subordinate aeolian and fluvial sandstones (e.g., Edgar et al., 2020; Grotzinger et al., 2014; Rivera-Hernández et al., 2019; Schieber et al., 2024; Stack et al., 2019). This is conformably overlain by the Carolyn Shoemaker formation, which contains interbedded mudstones and cross-bedded sandstones interpreted as an intermittent fluvial and lacustrine environment (Caravaca, Mangold, et al., 2022; Cardenas et al., 2022; Fedo et al., 2022; Gwizd et al., 2024). The Carolyn Shoemaker formation is overlain by the Mirador formation, possibly unconformably (e.g., Meyer et al., 2025), and corresponds to where the orbitally identified layered sulfate-bearing strata are observed from orbit (Fraeman et al., 2016).

The Mirador formation is currently subdivided into 6 members (Figure 2): the Dunnideer, Port Logan, Contigo, Catrimani, Amapari, and Chenapau members. Meter-scale cross-sets occur at the base of the Mirador formation (Rapin et al., 2021), specifically in the Dunnideer, Port Logan, and Contigo members with varying degrees of diagenetic alteration (Edgar et al., 2024; Meyer et al., 2025; Rapin et al., 2023b). The Contigo member also contains isolated, resistant lenses that record intermittent fluvial and lacustrine deposition (Caravaca, Le Mouelic, et al., 2022; Gupta, Dietrich, Lewis, Kite, et al., 2023; O'Connell-Cooper et al., 2025). The Catrimani member exhibits planar, laterally extensive laminae interpreted to be from the migration of wind ripples in aeolian sand sheets (Edgar et al., 2024; Roberts et al., 2023). Sharply overlying the Catrimani member is the thin (~0.5 m thick) Amapari member—originally identified from orbit and called the Marker Band for its distinctive dark-toned appearance, and laterally extensive trace (Weitz et al., 2022)—containing symmetric ripples interpreted to be formed in a shallow lake (Gupta, Dietrich, Lewis, Mondro, et al., 2023; Mondro, Fedo, et al., 2025; Mondro, Grotzinger, et al., 2025; Thompson et al., 2024; Weitz et al., 2023). The Amapari member is then overlain by the Chenapau member, which consists of planar strata and is truncated by large-scale scours interpreted to be from aeolian scouring of sandsheet deposits (Roberts et al., 2025). Mg-sulfate was first identified by CheMin within the upper-

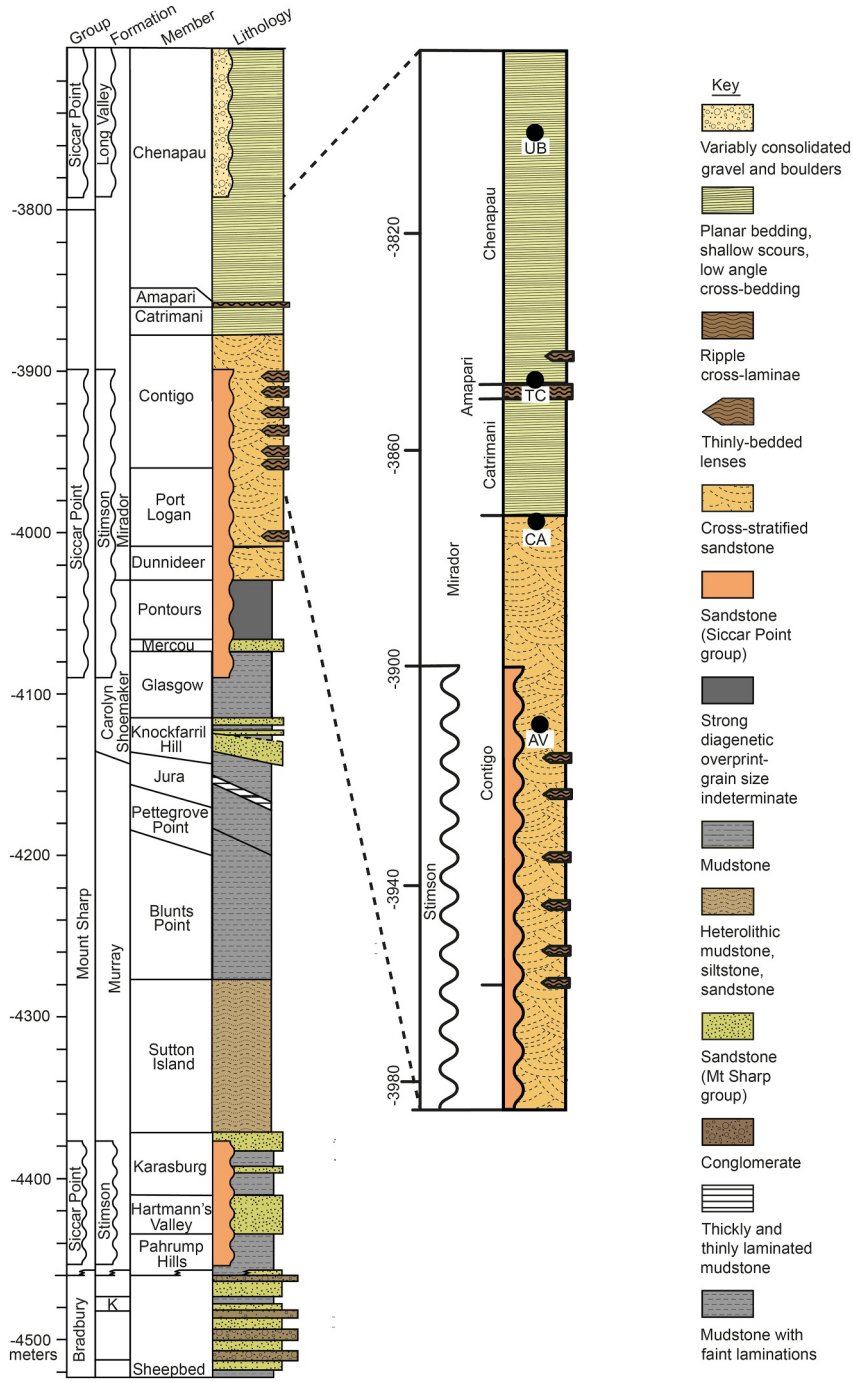

Figure 2. Stratigraphic column modified from the Mars Science Laboratory (MSL) Team's Sedimentology and Stratigraphy Working Group displays the vertical extents of the Bradbury, Mount Sharp and Siccar Point groups as encountered along the rover traverse. The inset stratigraphic column illustrates the stratigraphic context for Marker Band valley, the Contigo, Catrimani, Amapari, and Chenapau members of the Mirador formation, and locations of drill holes AV—Avanavero, CA—Canaima, TC—Tapo Caparo, and UB—Ubajara. Note: the Canaima drill hole was performed on an out-of-situ block from the Catrimani member.

most section of the Contigo member (Chipera et al., 2023), coinciding with the base of the orbitally defined Layered-Sulfate unit (LSu). LSu therefore coincides with the upper-most section of the Contigo member, along with the Catrimani, Amapari, and Chenapau members, which we discuss in depth in this manuscript.

3. Methodology and Data Sets

3.1. Instruments and Data Products

Architecture and unit relationships of the stratigraphy exposed in the buttes of Marker Band valley were investigated primarily using far-field images (>50 m) taken by the Mastcam, Navcam, and ChemCam instruments aboard the *Curiosity* rover. When stratigraphic units extended outside of the range of the rover's viewshed, stratigraphic unit correlation was investigated using orbital imaging data products. Detailed analysis of the sedimentary facies was performed using near-field images (<50 m) taken by the Mastcam, ChemCam, and MAHLI instruments.

3.1.1. Rover Instruments and Data Products

The two Mast Cameras (Mastcams—left and right; Bell et al., 2017; Malin et al., 2017) are located ∼1.9 m above ground level. High resolution RGB color images are provided by the 0.075 mRad/pixel sampling of the M100 camera (∼3.7 mm/pixel at 50 m viewing distance). Stereo photomosaics are possible due to the ∼24.2 cm separation between the M34 and M100 cameras, enabling spatial sampling of 0.22 mRad/pixel (∼10.9 mm/pixel at 50 m viewing distance). A white color balance was performed using *Adobe Photoshop* to ensure color consistency between images, to highlight subtle contrasts that record changes in surface properties, and to provide Earth-like lighting conditions for better representation of colors for interpretation and comparisons with terrestrial analogs.

The Navigation cameras (Navcams; Maki, 2018; Maki et al., 2012) provide 360° monochromatic (greyscale) context stereo mosaics at every rover waypoint with a resolution of 0.82 mrad/pixel (41.0 mm/pixel at 50 m viewing distance). With an interocular length of ∼42.4 cm between the two navigation cameras, stereo 3D-mesh products were derived (Alexander et al., 2006) typically accurate to a distance of ∼30–50 m from the rover.

The Chemistry and Camera instrument suite (ChemCam: Maurice et al., 2016) has the capability to take long distance image mosaics with its Remote Micro-Imager (LD RMIs; Le Mouelic et al., 2015, 2019). At 0.0205 mrad/pixel (1.0 mm/pixel at 50 m viewing distance), LD RMIs were sometimes used to supplement Mastcam data where instrument pointing safety restrictions were allowed. Panchromatic sharpening of high-resolution LD RMIs using lower-resolution color Mastcam photomosaics was occasionally performed in *ArcGIS Pro 3.1.1* to enhance color detail at certain outcrops outside of the rover's traverse.

The Mars Hands Lens Imager (MAHLI) is attached to *Curiosity's* arm turret and can be maneuvered to take close-up color images of outcrops. Standard procedures involve a sequence of images taken at nominal distances of 1 cm (spatial sampling of 16–21 μm per pixel), 5 cm (spatial sampling of 31 μm per pixel), and 25 cm (spatial sampling of 100 μm per pixel) (Edgett et al., 2012, 2015; Yingst et al., 2016). "Dog's eye" observations orient MAHLI orthogonal to the sedimentary structure within the outcrop. MAHLI can resolve grain sizes of coarse silt, ∼62.5 μm, or larger (Edgett et al., 2015; Yingst et al., 2016).

3.1.2. Orbital Data Products

The rover-derived data products were supplemented with ∼25 cm/pixel orbital images from the High Resolution Imaging Science Experiment (HiRISE; McEwen et al., 2007). For 3D data, a ∼1 m/pixel Digital Terrain Model (DTM) generated from HiRISE stereo pairs and the Mars Orbiter Laser Altimeter data products (Calef & Parker, 2016; Smith et al., 2001) was used.

3.2. Data Collection and Imaging Strategy

3.2.1. Far-Field Imaging Strategy

The rover entered Marker Band valley (Figure 3), the study area of this manuscript, on Sol 3575 (number of Martian days since *Curiosity* first landed in Gale crater). Marker Band valley is bracketed by the buttes informally named Orinoco, Chenapau, Bela Vista, Deepdale, and Bolivar (Figure 3), all of which contain portions of the ∼100 m thick sedimentary succession described in this manuscript. As the rover traversed along an optimal route to navigate through the terrain—known as the Mount Sharp Ascent Route (MSAR)—photomosaics of these buttes were planned at multiple angles to maximize coverage along the rover's closest approach when permitted by time, data volume, and energy constraints (e.g., Vasavada, 2022).

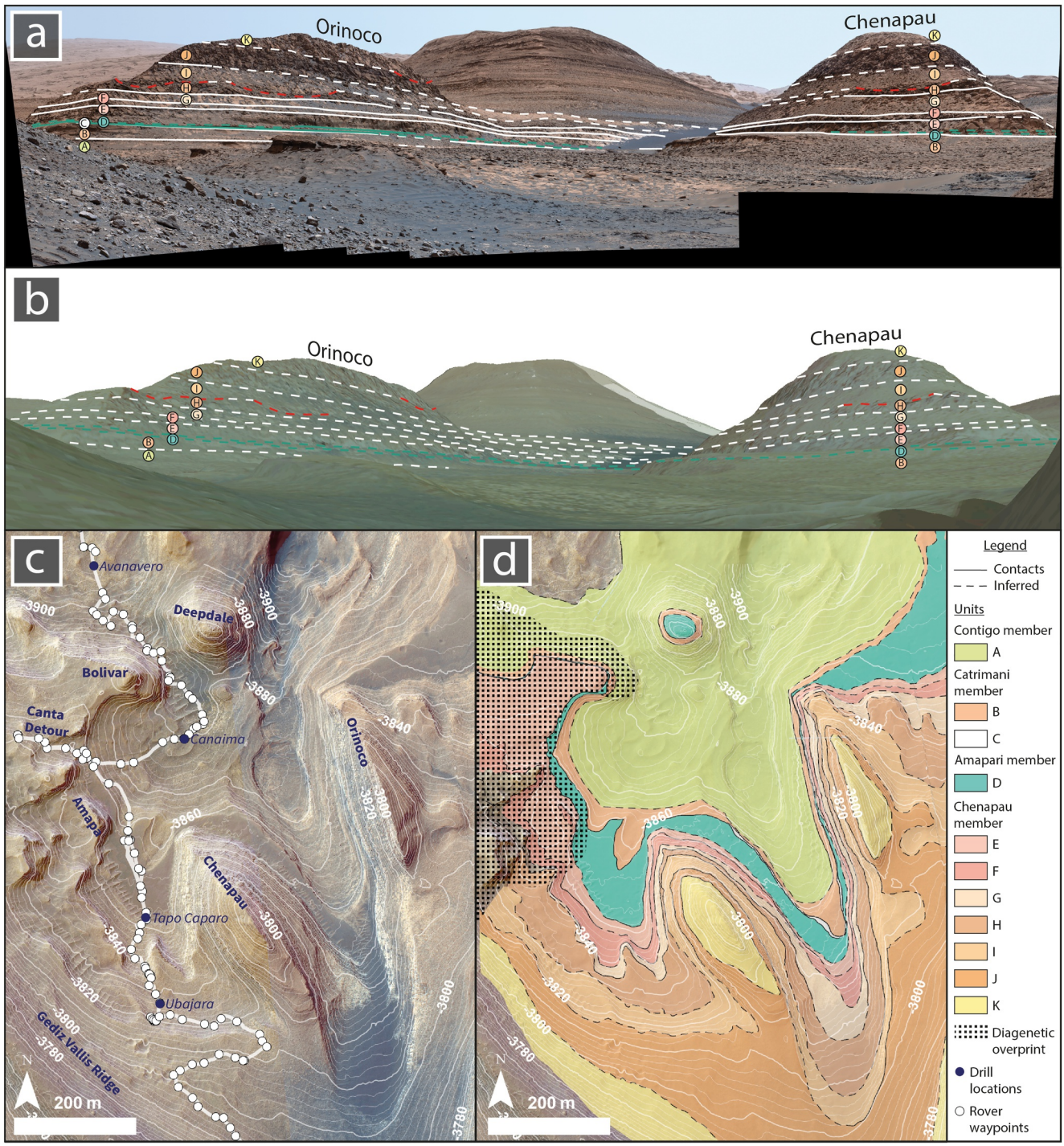

Figure 3. Geologic context used in planning. (a) Overview mosaic showing mapped geologic units in the Orinoco and Chenapau buttes in the Marker Band valley study area used in planning. Contact boundaries (white). The Amapari member (unit D) is in blue. Erosional scours are in red. Inferred boundaries are dashed. (Mastcam mosaic MR_mcam102554, acquired on Sol 3562, at Sol 3650 end-of-drive location). (b) Annotated *ArcGIS Pro 3.1.1* scene view of (a) showing the High Resolution Imaging Science Experiment (HiRISE) mosaic (~25 cm per pixel; Calef & Parker, 2016) draped across the HiRISE derived digital terrain model (DTM) (~1 m per pixel resolution; Calef & Parker, 2016; Smith et al., 2001). (c) Overview HiRISE map of the Marker Band valley region of the rover's traverse (from sols 3504 to 3910). White line shows Curiosity's traverse. Black-rimmed circles show the key imaging locations. Navy-filled circles show drilling locations. Note: the Canaima drill hole was performed on an out-of-situ block from unit B. (d) Geologic map of the Marker Band valley region used in planning. Note: the diagenetic overprint correlates with areas of the traverse overprinted by significant amounts of diagenesis (Figure 9e; e.g., Roberts et al., 2025). Image credits: NASA/JPL-Caltech/MSSS.

3.2.2. Geologic Map Creation for Strategic Planning

Distinct alternating "dark-toned" and "light-toned" stratigraphic packages—tonal differences that were also visible in HiRISE mosaics (Figure 3c)—were identified on each butte. These stratigraphic packages have different sedimentary textures, weathering patterns, and elevations visible from surface and orbit, which allowed for the subdivision of this stratigraphic succession into 11 distinct units (as described in Section 4). To spatially contextualize these units, we created shapefiles of unit outcrops through comparisons of Mastcam mosaics with 3D local scene views in *ArcGIS Pro 3.1.1*, employing the same coordinates, elevation, heading, roll, pitch and extent parameters as the rover's mast camera at each location. We then correlated these units identified in Mastcam mosaics to distinct tones, surficial textures, apparent induration, and elevations of rocks in HiRISE mosaics. Only a small amount of vertical elevation changes were identified for each unit between nearby buttes, consistent with the gentle dips of 2–4° for bedding in the Mount Sharp group (Stein et al., 2020; Turner & Lewis, 2023). A geological map was created for this study area and these stratigraphic units were projected across the planned traverse (Figure 3d), allowing the rover to document the lateral equivalent of each unit for workspace imaging and contact science.

3.2.3. Rover Workspace Imaging and Contact Science

The rover traversed the study area from Sols 3575 to 3919 (Figure 3c). Rover waypoints were planned for each of the stratigraphic units in the geologic map (Figure 3d) along the MSAR for contact science and targeted imaging when engineering constraints allowed (e.g., Rankin et al., 2020). Representative outcrops were identified in Navcam mosaics and subsequently targeted with Mastcam or ChemCam's RMI for more detailed facies analysis when planning constraints allowed. MAHLI image coverage had additional planning constraints associated with deployment of the arm (Yingst et al., 2016). In total, 337 Mastcam, LD RMI, and MAHLI mosaics were used in identifying the sedimentary textures and lithofacies of each unit as described in Section 4.

3.3. Data Analysis

3.3.1. Mastcam Image Analysis

Mastcam data products (Table S1 in Supporting Information S1) were processed to remove the effect of lens distortion and surface radiation, merged into mosaics, and white-balanced to optimize both visibility and accuracy of the sedimentary textures and architecture for analysis. Analysis of the stratigraphy was predominantly performed using stereo pair images from M34 and M100. Interpreted data products used M100 mosaics as the base image. As the range to outcrops varied relative to the rover (Figure S1 in Supporting Information S1), different approaches were required to assess sedimentary textures at different scales. For "farfield" outcrops—predominantly coverage of the stratigraphic cross-sections exposed in the local buttes—spatial sampling ranged from ∼17 to 0.5 mm/pixel and were only used to examine bulk stratigraphic architecture, sedimentary architectures (if visible at that scale), unit contacts, and location and extent of unit outcrops. For "nearfield" outcrops—coverage of outcrops near to or within the rover workspace—spatial sampling ranged from ∼0.5 to 0.1 mm/pixel and were used for more detailed facies analysis, and sedimentary architecture. Mosaics were interpreted using vector graphic software to highlight facies, sedimentary architecture, and relationships between depositional surfaces.

Quantitative information on sedimentary architecture and facies was derived from the 3D Navcam mesh (Alexander et al., 2006) when outcrops were within ∼50 m. At distances further than 50 m, quantitative information was provided using *ArcGIS Pro 3.1.1* on the HiRISE orthomosaic to correlate features of interest visible in both the HiRISE and Mastcam mosaics (Table S4 in Supporting Information S1). This was supplemented with GIS projected viewsheds using the HiRISE DEM based on the rover co-ordinates and imaging specifications, and were quantitatively assessed using the HiRISE DTM. To account for foreshortening when measuring apparent dips, we only measured the parts of the image mosaic oblique to outcrops.

3.3.2. MAHLI Image Analysis

MAHLI images helped resolve fine-scale sedimentary structures in the stratigraphy for a more detailed facies characterization. Measurements of laminae thickness could be performed on MAHLI images orthogonal to bedding as described by Edgar et al. (2020). Grayscale pixel intensity was assessed as a proxy for laminae

thickness as described by Gwizd et al. (2022) using the open-source image processing program, ImageJ (Schneider et al., 2012). Python code was developed using the scipy library (Virtanen et al., 2020) using the "find_peaks" function on the grayscale pixel intensity with the difference between peaks used as a proxy for laminae thickness as described in Figure S1 in Grotzinger et al. (2015). The arithmetic mean, median, minimum, maximum, and standard deviation values for each measured section were then calculated (Table 2; Figures S2–S9 in Supporting Information S1).

4. Stratigraphy and Sedimentology

The Contigo, Catrimani, Amapari, and the Chenapau members are exposed as a ∼100 m thick sedimentary succession across the seven buttes that define Marker Band valley (Figure 4). Within this succession, 11 distinct stratigraphic units, designated units A through K from oldest to youngest, were identified based on distinct bedrock textures, observable contacts, sedimentary architecture, and stratigraphic distribution (summarized in Table 1). Here, we describe the stratigraphic architecture and facies of units A through K and provide interpretations of their depositional processes in stratigraphic order.

4.1. Contigo Member

4.1.1. Unit A

4.1.1.1. Architectural Elements

Unit A, approximately 40 m-thick, is characterized by repetitive, vertically stacked tabular beds that are characterized by low-angle crossbedding and range from 2 to 6 m in thickness (Figure 5). These beds are laterally continuous and traceable for up to ∼350 m along the western extent of the valley (Figure 5a), while maintaining consistent thicknesses (Figures 5b and 5c). Crossbedding is evident in four of the beds, with strata sets dipping at apparent dips of ∼4–5° to the north. Each cross-bed is disconcordantly truncated by sharp, planar, laterally extensive bounding surfaces (Figures 5c and 5d). While strata at the top of each cross-bed appeared light-toned and recessive, horizons of thin, dark-toned, erosion-resistant strata separate the light-toned strata sets higher up in the succession as they asymptotically tapered against the underlying bounding surface (Figures 5d and 5e). In northeast-facing sections, crossbedding could not be identified (Figure 5e).

At similar elevations across the rover traverse (Figure 6), distinct planar bedding was identified separated by cm-thick, resistant, dark-toned bands (Figure 6a). Each bed was comprised of light-toned sets separated by thin, mm-scale, erosion-resistant, dark-toned laminae (Figures 6a and 6b). The light-toned sets consisted of parallel, laterally extensive laminae with apparent thicknesses of ∼0.7 ± 0.3 mm. Occasional weathered sections show thin, protruding, light-toned horizons between each laminae in a pinstripe pattern (Figures 6b and 6c). These light-toned laminae could be scratched by the DRT. The dark-toned strata truncated the sets of light-toned laminae and occasionally formed protruding fins (Figure 6b). In plan view, the resistant strata appeared dark gray, pitted, had a slight lustre in dust-free surfaces, and could not be scratched with the Dust Removal Tool (DRT) before MAHLI imaging. Given both the northward dip of the cross-bedding and how nearfield observations by the rover were made on a north-facing slope, the viewing angle was likely parallel to the strike of the cross-bedding, and thus perpendicular to the transport direction of these primary bedforms, thus explaining the absence of cross-stratification in nearfield images.

A lower contact of unit A was not observed in Marker Band valley due to poor exposure. However, an irregular surface was observed in a butte to the north of Deepdale (Figure 7). This irregular surface, displaying ∼1 m of paleotopographic variation, can be traced across outcrops for over 75 m in disparate outcrops. This surface sharply truncates the underlying trough cross-stratified strata (Figure 7) and is overlain by cross-stratified tabular beds with consistent set thicknesses and sharp planar bounding surfaces. As the sedimentary architecture was characteristic of unit A and these tabular beds occurred at elevations similar to exposures of unit A in Marker Band valley, we infer that this irregular surface marks the lower contact of unit A.

4.1.1.2. Interpretation

The geometry of the vertically stacked, north-dipping cross-beds suggests that the deposits originated from lateral accretion of simple, migrating dunes. As the beds appear planar and lack observable cross-bedding in south- and north-facing outcrops, the primary bedforms were likely simple, two dimensional, and migrating toward the north

Table 1
Sedimentary Facies for Units A Through K

Member	Unit	Thickness (m)	Dominant stratification	Architectural elements	Unit contact	Lithofacies	Interpretation
Contigo	A	~40	Low angle cross-bedding.	Vertically stacked, laterally continuous tabular beds (2–6 m thick) of low-angle cross-stratification, dipping north, abutting sharp planar bounding surfaces (Figure 5).	Irregular contact with underlying clay-sulfate transition; ~1 m paleo-topographic relief (Figure 7).	Interbedded resistant dark-toned laminae and cm-scale light-toned sets at bed base; top composed of homogeneous, laterally extensive planar laminae (Figure 6).	Lateral accretion of simple migrating aeolian dunes. The irregular lower contact marks a candidate aeolian supersurface above the clay-sulfate transition.
Catrimani	B	~5	Light-toned, planar bedded lithofacies with occasional pervasive overprinting.	Laterally extensive tabular bed; consistent thickness (for ~350 m extent laterally) (Figure 8).	Sharp, planar boundary with unit A (Figure 8).	Uniform, laterally continuous, planar laminae; occasional overprinting by pervasive nodules (~3–4 mm) (Figure 9).	Continuous deposition in a dry aeolian sandsheet environment with limited sand supply and near-surface water.
	C	~0.3	Structureless, mottled, light-toned lithofacies.	Mottled outcrop with cycloidal lower contact pattern; infills of V-shaped wedges (Figures 10a–10c).	Irregular lower contact forming a cycloidal pattern against unit B (Figures 10a–10c).	Cycloidal base pattern; south-dipping fractures (Figures 10a–10c); mottled appearance in uppermost ~0.05 m (Figures 10d and 10e).	Contraction-expansion processes potentially thermal contraction on a regional scale above a supersurface with surface alteration, possibly linked to groundwater fluctuations.
Amapari	D	~1	Lower: dark-toned, rippled lithofacies; upper: light-toned, planar bedded lithofacies with laminae organized in ~cm thick bundles.	Tabular ledge/platform forming unit; laterally continuous (~250 m extent) (Figure 11a).	Planar lower contact with underlying unit C (Figure 10a).	Lower: symmetric ripple forms (~4.5 cm wavelength) in chevron stacks (Figures 11b–11d); Upper: ~cm thick bundles of planar and indeterminate laminae (Figures 11d and 11e).	Lacustrine deposition in a shallow lake.
Chenapau	E	~3.6	Light-toned, planar bedded lithofacies with pervasive nodular overprinting.	Scarp-forming tabular bed; sharp, planar basal boundary with subtle overhang; laterally continuous (~125 m extent) (Figures 12a–12c). Embedded dark-toned lens with cm-scale cross-bedding and lateral pinching (Figure 13).	Sharp basal, planar contact marked by a resistant band (Figures 12a–12c).	Planar stratification with minimal upwarping at the contact (Figures 12b and 12c); laminae overprinted by diagenesis (Figures 12d and 12e).	Subaerial deposition as an aeolian sandsheet following a transition from lacustrine conditions. Embedded fluvial lens.
	F	~4.2	Planar bedded lithofacies with corrugated textures.	Tabular bed; consistent thickness (across a ~350 m extent laterally); corrugated textures present (Figure 14a).	Sharp conformable basal contact with unit E (Figure 14a).	Planar bedded lithofacies with wavy laminae with preserved and climbing ripple forms; mm-scale nodules. (Figures 14b and 14c).	Deposition of supercritically climbing ripples that can be attributed to either aeolian or damp conditions.
	G	~2.7	Light-toned, planar bedded lithofacies.	Slope-forming, recessive unit with homogenous appearance and rounded weathering profile; laterally continuous (~250 m extent) (Figure 14a).	Gradational contact from underlying unit F; absence of wavy bedding (Figure 14a).	Uniform, planar, low-angle to horizontal laminations; pinstripe laminae; resistant "fins" or protrusions creating corrugated textures; mm-scale nodules (Figure 15).	Continuous deposition in a dry aeolian sandsheet environment with limited sand supply and near-surface water.

Journal of Geophysical Research: Planets
10.1029/2025JE009556

Journal of Geophysical Research: Planets

10.1029/2025JE009556

Table 1
Continued

Member	Unit	Thickness (m)	Dominant stratification	Architectural elements	Unit contact	Lithofacies	Interpretation
	H	~5.3	Dark-toned, planar bedded lithofacies.	Scarp-forming unit of recessive sets interbedded with thin resistant horizons; laterally continuous (~250 m extent) (Figure 16a). Truncated by ~60 m wide aeolian scours (Figure 16b).	Gradational contact with unit G; marked by introduction of indurated beds (Figure 16a).	Planar, parallel laminae in sets (1–12 cm thick) bound by resistant laminae forming fins (Figure 17a); pinstripe laminae (Figure 17b); discontinuous horizons of wavy and irregularly undulating laminae (Figures 17b–17e); occasional frozen ripples (Figure 17b); possible pseudo cross-laminae (Figure 17d); thin needle-like forms (Figure 17f).	Intermittent damp aeolian sandsheet deposition with candidate adhesion structures. Indurated laminae suggest preferential cementation, formed by later diagenetic processes.
	I	~4.9	Light-toned, planar bedded lithofacies.	Light-toned, smooth, rounded blocks; often appears massive due to diagenetic overprint; laterally continuous (~250 m extent) (Figures 16a and 18a).	Drapes over unit H with associated scours (Figure 18a).	Uniform, planar, laterally continuous laminae; mm-scale nodules (Figures 18b–18d); pinstripe laminae (Figure 18d).	Continuous deposition in a dry aeolian sandsheet environment with limited sand supply and near-surface water.
	J	~7.3	Dark-toned, planar bedded lithofacies.	Dark-toned, interval comprised of resistant and recessive interbedded beds; laterally continuous (~250 m extent); laterally continuous with minor truncation by large scours (Figure 19a).	Gradational contact with unit I; marked by introduction of indurated beds.	Planar, parallel laminae in sets (1–12 cm thick) bound by resistant, corrugated or irregular laminae (Figures 19a, 19b and 20a–20e); pinstripe laminae (Figures 20a and 20b); discontinuous horizons of wavy and irregularly undulating laminae (Figure 19c); occasional frozen ripples (Figure 19d).	Intermittent damp aeolian sandsheet deposition with candidate adhesion structures. Indurated laminae suggests preferential cementation, formed by later diagenetic processes.
	K	~12.9	Light-toned, planar bedded lithofacies.	Slope-forming; light-toned unit forming, smooth, rounded blocks (Figure 19a).	Overlies unit I with sharp contacts where visible (Figure 19a).	Uniform, laterally extensive planar laminae; mm-scale nodules (Figure 21).	Continuous deposition in a dry aeolian sandsheet environment with limited sand supply and near-surface water.

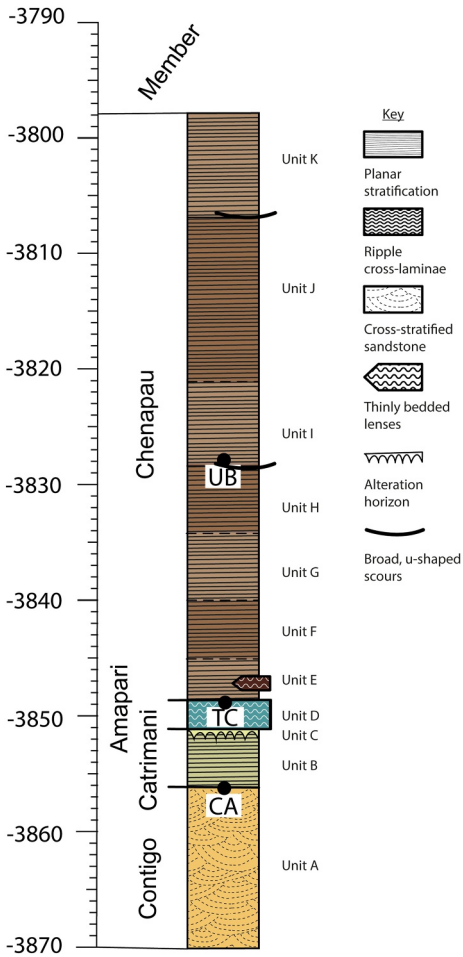

Figure 4. The stratigraphic column of the Contigo (yellow), Catrimani (green), Amapari (blue), and Chenapau (brown) members of the Mirador formation in the study area and units A through K as discussed in this manuscript. Black circles represent the drillholes: UB—Ubajara; TC—Tapo Caparo; and CA—Canaima. Note: the light- and dark-toned planar bedded lithofacies in the Chenapau member are represented by light and dark brown shading, respectively. Additional stratigraphic unit elevations across major buttes and along the rover traverse within the study area are provided in Table S4 of Supporting Information S1.

(e.g., Figure 5 in Rubin & Hunter, 1982). Due to the observed low-angle of the cross-bedding, only the lower portion of the dune was preserved, and their asymptotic bases are consistent with aeolian dunes (e.g., Kocurek, 1986; Mountney, 2012). The bounding surfaces between sets were caused by truncation by scouring along interdune corridors preceding dunes (Kocurek, 1996; Mountney & Howell, 2000). The planar appearance could indicate that the dunes are two-dimensional (i.e., straight-crested) or migrate at a constant rate of migration (e.g., Mesquita et al., 2021; Mountney & Howell, 2000; Rubin, 1987) or as a result of dune scour eroding down to the water table (Kocurek & Day, 2018; Kocurek & Havholm, 1993b; Veiga et al., 2002). An absence of interdune deposits between cross-sets, however, suggests that the dunes were deposited in an aeolian system where groundwater may have controlled the limits on precedent dune scour (e.g., Kocurek, 1996; Mountney, 2012).

In the light-toned sets, the uniformity, lateral persistence, and planar nature of the laminae closely resemble the laminae formed by the migration of wind ripples on Earth (e.g., Ferronatto et al., 2019; Kocurek & Nielson, 1986) and elsewhere on Mars (Banham et al., 2018; Grotzinger et al., 2005; Roberts et al., 2025; Yingst et al., 2023). Thin, resistant layers between the laminae create a pinstripe pattern, a characteristic feature emerging from differing permeability-related properties in inversely graded wind ripples (Fryberger & Schenk, 1988). In wind ripples, fine silts deposited within migrating troughs retain moisture more effectively than the coarser grains in the ripple cores, which have larger pore spaces (Fryberger & Schenk, 1988; Mountney, 2006a). This moisture retention leads to preferential cementation and the formation of thin pin-like lines (Fryberger & Schenk, 1988; Mountney, 2006a). These have previously been identified and associated with sulfate-bearing deposits on Mars (e.g., Grotzinger et al., 2005; Roberts et al., 2025). The cm-scale, low-angle, cross-laminated sets are likely a result of the reactivation of wind-ripple deposition after slight changes in wind dynamics (Kocurek, 1996; Mountney, 2006b). Due to the lateral association with the cross-bedding observed in the Orinoco butte, these light-toned sets originated from migration and climbing of wind ripples over slip faces of dunes (e.g., Hunter, 1977; Mountney, 2006a). The predominance of wind-ripple laminae also supports the idea that only the apron of the dune is preserved (e.g., Kocurek, 1986).

The induration of the dark-toned laminae—often found truncating sets of wind-ripple strata—may have occurred after lithification through preferential diagenesis or cementation. As fine-grained lithofacies preserved in pinstripe laminae that taper concordantly across set bounding surfaces are more tightly packed, more water is retained often leading to preferential cementation and diagenesis (e.g., Carr-Crabaugh & Dunn, 1996; Fischer et al., 2012; Heidsiek et al., 2020). We interpret that this process formed the resistant horizons in unit A and could explain how similar the dark-toned, resistant appearance of the pinstripes in unit A are to the slightly thicker, indurated laminae that occur at the bounding surfaces (Figures 5d and 6a, 6b).

An irregular surface was identified to underlie tabular crossbedding with a similar appearance to unit A prior to entering Marker Band valley (Figure 7), and is interpreted as an unconformity. The strata underlying this surface is comprised of trough cross-stratification with a similar appearance to the trough cross-stratification which dominates the clay-sulfate transition sedimentary succession (Figure 7; e.g., Edgar et al., 2024; Gupta et al., 2022; Rapin et al., 2021). Given the irregularity of this surface, its lateral extent across hundreds of meters, and how it marks a distinct change in cross-stratification style from trough cross-stratification to tabular cross-stratification, the base of unit A likely represents deposition following a regionally significant aeolian supersurface (e.g., Havholm & Kocurek, 1994; Kocurek, 1996) that marks the base of the layered sulfate succession.

Table 2
Measurements of Apparent Average Laminae Thickness for Units A Through K

Member	Unit	Apparent laminae thickness (mm)	s.d (mm)	Count	Resolution	Target (camera sequence/Product code)
Contigo	A	~0.7	0.3	219	0.099 mm/pixel	Marshall Falls (3596MH0001900011300680C00_MhliImage_0716740069-45544-1)
Canaima	B	~1[a]	0.3	92	0.3 mm/pixel	Waioklepalul (mcam102798)
	C	N/A	N/A	N/A	N/A	Mamupi (3642MH0003690001301560R00_MhliZstack_0720811892-06470-1)
Amapari	D	4 to 10				See Mondro, Fedo, et al. (2025), Mondro, Grotzinger, et al. (2025)
Chenapau	E	~1[b]	N/A	N/A		Chenapau valley extension (mcam103681)
	F	~1[b]	N/A	N/A		Cauame (mcam103808)
	G	~1[a]	0.3	34	0.5 mm/pixel	Teotonio (mcam103899)
	H	~3[a]	1.35	25	0.6 mm/pixel	Camopi (mcam103951)
	H/I contact	~1[a]	0.4	52	0.3 mm/pixel	Ubajara extension (mcam104018)
	I	~0.76	0.058	180	0.1 mm/pixel	Kastria Spring (3866MH0001900011400878C00_MhliImage_0740708055-51665-1)
	J	~1.5[a]	0.8	58	0.3 mm/pixel	Zarelia (mcam104420)
	K	<1 mm[b]	N/A	N/A		Workspace extension (mcam104608)

Note. This table presents the average laminae thickness for each unit, as determined through various methods. Unit I was measured manually using analogue techniques; comparison with automated methods yielded identical average values but an increased standard deviation of 0.34 (Figures S2–S9 in Supporting Information S1). [a]Measurements derived from Mastcam images, potentially affecting accuracy. [b]Units with poor outcrop exposure, lacking cross-sections of laminae.

4.2. Catrimani Member

4.2.1. Unit B

4.2.1.1. Architectural Elements

Unit B comprises a scarp-forming, ~5-m-thick, planar stratified, tabular bed, marked by a prominent sharp, planar, and laterally extensive lower contact with the underlying unit A. In vertical exposures, this unit maintains a consistent thickness for nearly 350 m along the western extent of Marker Band valley in the Orinoco butte (Figure 8a), ~120 m along the northern face of Bolivar (Figures 8c and 8d), and elsewhere in vertical exposures in Marker Band valley.

Along the rover's traverse, unfavorable exposure, weathering and overprinting by diagenesis, obscured fine-scale primary structures. Overprinting was most evident in the form of pervasive, rounded nodules ~3–4 mm in diameter that disrupted finer primary sedimentary textures (Figure 9e). However, evidence of planar stratification was still preserved (Figure 9e). The contact between unit A and B was inferred where crossbedding and the resistant bands of unit A were no longer visible.

Displaced blocks interpreted as derived from unit B exhibiting a lower degree of diagenetic alteration were also encountered along the rover traverse (Figures 9a and 9c). These blocks were characterized by homogenous, light-toned planar bedding composed of distinctly uniform, parallel, laterally extensive laminae with apparent thicknesses of ~1 ± 0.3 mm (3–4 pixels thick, or approximately 0.9–1.2 mm; Figures 9b and 9d). Notably, these laminae did not include the fin-forming, dark-toned, resistant laminae or horizons characteristic of unit A (Figures 6a and 6b). Unit B was relatively soft, as confirmed by DRT scratches, and exhibited a bright white tone when driven over by the rover. Rounded nodular textures, ~3–4 mm in diameter, were also present but less pervasive than those observed in in situ exposures (Figure 9b). Based on the light-toned appearance, planar stratigraphy, absence of resistant dark-toned laminae observed in unit A, and presence of nodular textures similar to those seen in situ within unit B, we infer these blocks as fragments from unit B.

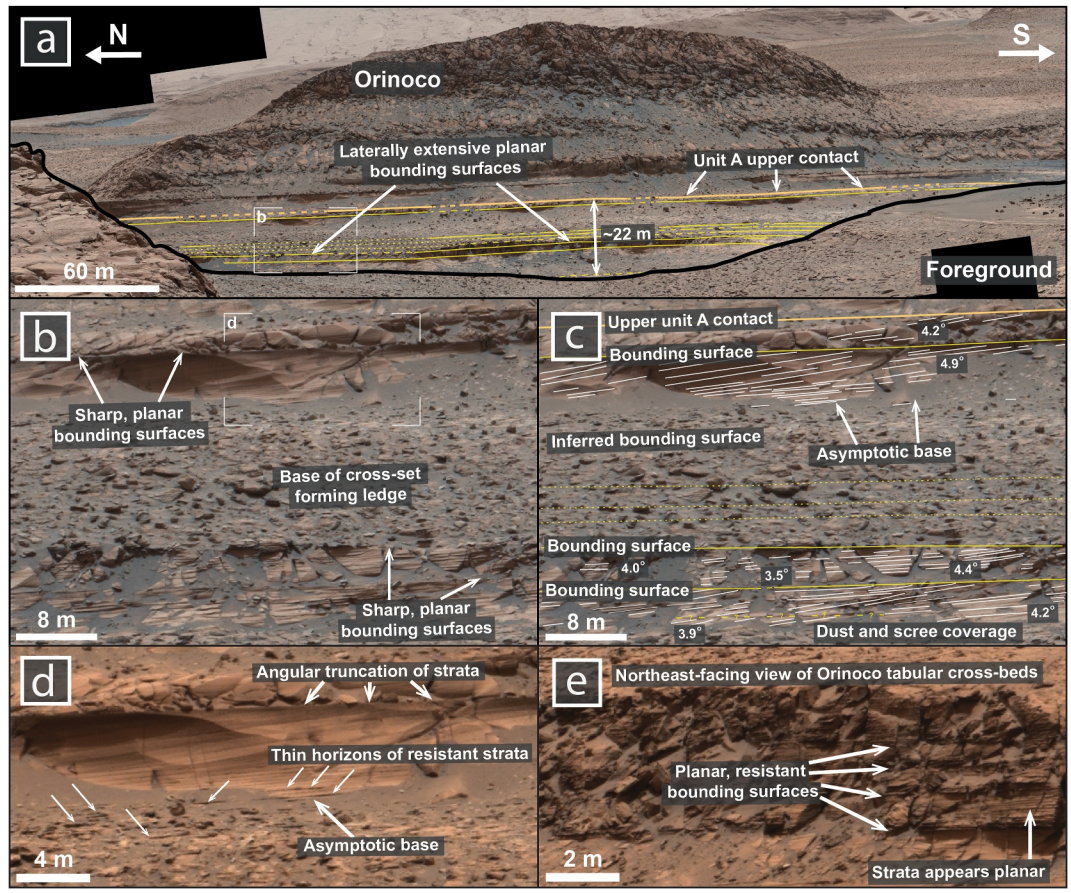

Figure 5. Orinoco butte mosaic showing Unit A. (a) Mastcam mosaic of Unit A illustrating Unit A's upper contact (thick cream line) and bounding surfaces (yellow lines) where visible truncation of cross-strata (continuous), visible no truncation (dashed), and inferred (dotted) (Mastcam mosaic MR_mcam103144 acquired on Sol 3662, at Sol 3658 end-of-drive location) (b) Detail of uninterpreted cross-bedded sets. (c) Interpretation of cross-bedded sets showing the upper contact, bounding surfaces, and cross-bedding (white). (d) Detail of cross-bedding showing angular truncation of strata, asymptotic bases of cross-sets, and thin horizons of resistant strata. (e) Northeast facing view of Orinoco tabular beds highlighting the absence of identifiable cross-bedding at different outcrop orientations and resistant strata concentrated at the planar bounding surfaces (Mastcam mosaic MR_mcam103184 acquired on Sol 3667, at Sol 3665 end-of-drive location). Image credits: NASA/JPL-Caltech/MSSS.

4.2.1.2. Interpretations

The homogeneity and lateral continuity of the laminae in unit B—along with unit B's direct association with the underlying dune cross-bedding—are diagnostic of subcritically climbing translatent strata, formed by the migration of wind-ripples (Chakraborty & Chakraborty, 2001; Fryberger et al., 1979; Fryberger & Schenk, 1988; Hunter, 1977; Kocurek & Nielson, 1986). The uniformity of laminae thickness both laterally across the same lamina and vertically compared to preceding and anteceding laminae may reflect steady winds and near-constant deposition rates (Hunter, 1977; Trewin, 1993). Alternatively, the laminae could reflect plane bed lamination, formed under high wind velocities on flat, smooth surfaces (Clemmensen & Abrahamsen, 1983; Hunter, 1977; Kocurek & Dott, 1981; Ventra et al., 2017). A third possibility is that the laminae were deposited as aeolian loess; however, this interpretation is less likely due to the absence of massive bedding, which is typically observed in such deposits (e.g., Pécsi, 1990). Although diagenesis and weathering have obscured finer-scale primary structures within in situ outcrops, features commonly linked to wetter interdune conditions—such as symmetrical ripples and adhesion laminae (e.g., Kocurek & Nielson, 1986)—are absent.

The planar and tabular geometry of unit B indicates either a flat-lying interdune or sandsheet depositional environment (Kocurek & Nielson, 1986; Langford & Chan, 1989; Mountney, 2006b; Mountney & Jagger, 2004; Mountney & Russell, 2009). The lateral continuity of unit B, extending for hundreds of meters both parallel and

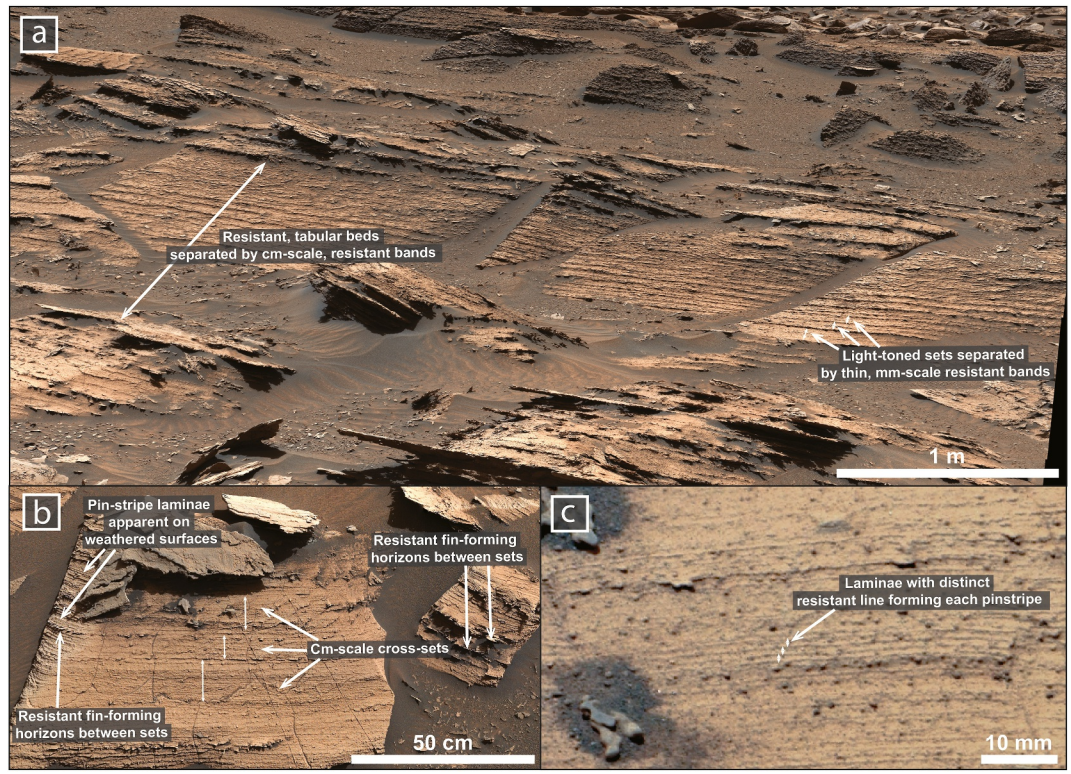

Figure 6. Examples of select facies characteristic of unit A as encountered across the traverse. (a) Mastcam mosaic of the tabular, m-scale bedding. Note the grouped thick dark-toned resistant bands that separate each bed. Beds are comprised of cm-scale sets separated by thinner mm-scale, resistant bands. (mastcam mosaic MR_mcam102756 acquired on Sol 3596, at Sol 3594 end-of-drive location). (b) Mastcam mosaic showing low-angle truncation of cm-scale sets. Note how resistant laminae between sets can form fins. (mastcam mosaic MR_mcam102748 acquired on Sol 3594, at Sol 3594 end-of-drive location). (c) Mastcam mosaic of the planar, laterally extensive, mm-scale laminae. Note how thin, resistant lines between each of the laminae form a pinstripe pattern. (mastcam mosaic MR_mcam102757 acquired on Sol 3596, at Sol 3594 end-of-drive location). Image credits: NASA/JPL-Caltech/MSSS.

perpendicular to the wind transport direction, and the absence of any lateral transitions or contacts with dune cross-beds, favors the laterally extensive aeolian sandsheet interpretation over the interdune environment bounded by dunes interpretation (e.g., Kifumbi et al., 2022; Kocurek & Nielson, 1986; Mountney, 2006b; Rodríguez-López et al., 2010; Veiga & Spalletti, 2007). A sandsheet depositional environment would suggest limited sand supply leading to wind-driven sand accumulation and deposition through the migration of wind-ripples instead of larger dunes (Kocurek & Nielson, 1986; Loope & Simpson, 1992; Mountney, 2006a). Sand availability may have been restricted by the presence of near-surface water (e.g., Kocurek & Nielson, 1986), or slight cementation by salt (Nickling, 1984). In Marker Band valley, sulfate cementation likely occurred near the surface, as chemical data suggests for underlying sulfate enrichments (e.g., Rapin et al., 2019, 2023b).

The basal contact of unit B is interpreted as a major bounding surface. As this same bounding surface can be traced continuously for hundreds of meters, this surface could represent a period of scale erg deflation or contraction (Kocurek, 1988; Loope & Simpson, 1992; Mountney, 2006b). Sandsheets are not uncommon after regional deflation (Kifumbi et al., 2022; Kocurek & Nielson, 1986; Mountney, 2006b), as rising groundwater levels accompanied by sediment availability at an equivalent rate can lead to promotion of aeolian sand accumulation without dune development. Alternatively, a transition into a sandsheet dominated erg marginal environment (e.g., Kocurek & Nielson, 1986) is also equally as likely.

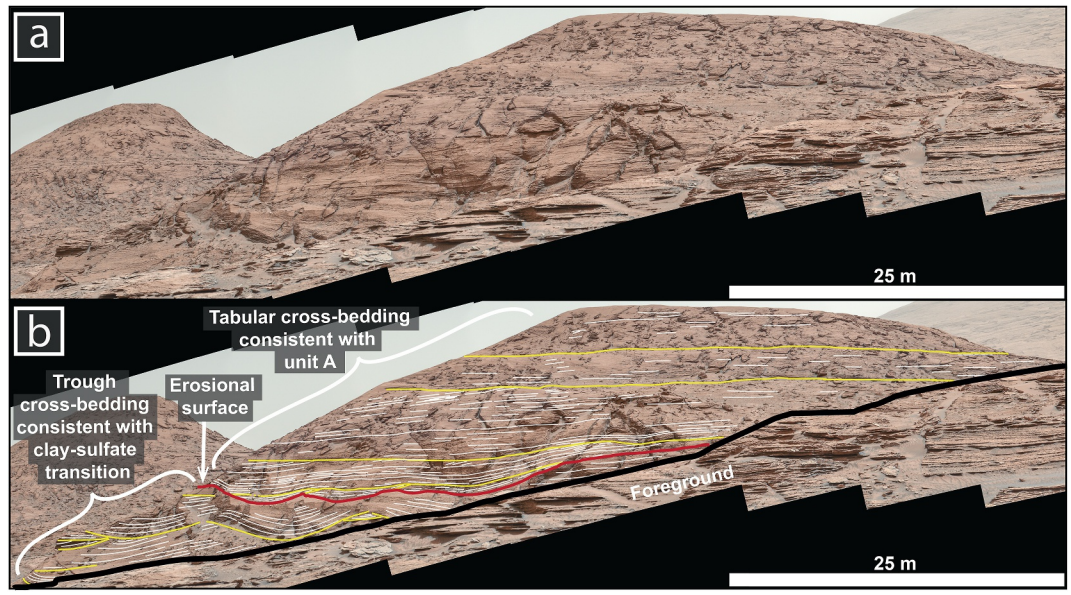

Figure 7. Mastcam mosaic of inferred boundary between the underlying Clay-Sulfate transition and the overlying unit A. (a) the uninterpreted mosaic of the butte north of Deepdale (mastcam mosaic MR_mcam102097 acquired on Sol 3485, at Sol 3483 end-of-drive location) and (b) the interpretation of the erosional surface that separates trough cross-bedding consistent with bedding expression in the clay-sulfate transition (Edgar et al., 2024; Gupta, Dietrich, Lewis, Mondro, et al., 2023, Gupta, Dietrich, Lewis, Kite, et al., 2023) and tabular cross-bedding consistent with the lithofacies observed in unit A. This erosional surface (red) expresses ∼1 m of paleo-topographic relief. Bounding surfaces (yellow lines) separate and truncate cross-strata (white lines). Note how overlying bounding surfaces and stratigraphy drape across the erosional surface. Image credits: NASA/JPL-Caltech/MSSS.

4.2.2. Unit C

4.2.2.1. Architectural Elements

Unit C, approximately ∼0.3 m thick, outcrops as a light-toned structureless unit and shows an irregular lower contact with unit B that forms a pronounced, cycloidal-like pattern against the underlying strata (Figure 10). Laterally, the unit appears to extend up to ∼350 m across Orinoco's eastern flank (Figure 10) and ∼120 m across the northern and southern faces of Bolivar. HiRISE images suggest this unit continues beyond Marker Band valley, with possible exposures over ∼2 km away (Farrand et al., 2025). In cross-section, unit C is characterized by a mottled, light-toned, structureless strata that overlies and infills V-shaped wedges (∼0.03 m thick, ∼0.02 m width; Figures 10b and 10e). Rounded, concave-down sections of undisturbed planar stratification from unit B separate each wedge (Figures 10b and 10e). Although wedge spacing is not clearly uniform, these wedges consistently recur across the total extent of Orinoco. Pronounced south-dipping fractures delineate the south side of each tapered wedge, rarely exceeding a vertical extent of 0.3 m—matching the total unit thickness—and appear to cross-cut adjacent wedges (Figure 10c). The uppermost ∼0.05 m of unit C lacks visible fractures, protrudes slightly, and shows a nodular mottled texture (Figure 10b).

Whilst mostly covered in regolith, in one location, the rover encountered bedrock with a purple and light-toned mottling directly below unit D (Figures 10d and 10e). MAHLI images of DRT target Mamupi (Figure 10e) nearby also revealed a soft, structureless, and mottled texture. Localized mottling was observed in nearfield images as ∼5 mm diameter patches of light-toned material and ∼1 mm gray-green semi-circular spots against a background that was predominantly reddish in color (Figure 10e). The mottled, structureless appearance and stratigraphic context lead us to infer that this target was an outcrop of unit C.

4.2.2.2. Interpretations

Unit C is interpreted to represent an alteration horizon. Its lateral extent suggests this horizon is at least locally significant. As the fracture sets are predominantly confined to unit C, penetrating only minimally into the top of unit B, and the overlying bedding in unit D is undisturbed, fracturing would have been temporally localized

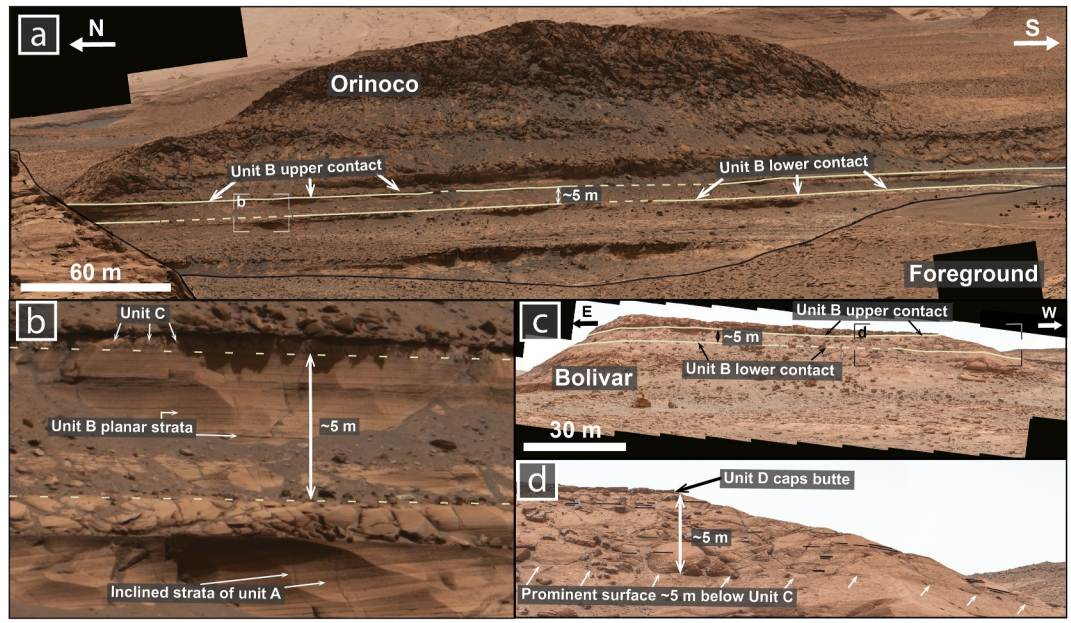

Figure 8. Mastcam mosaics of Orinoco and Bolivar buttes illustrating unit B. (a) Mastcam mosaic of the western face of Orinoco butte, showing tabular unit B, which is laterally extensive (and can be traced across ~350 m) with a consistent thickness of ~5 m (Mastcam mosaic MR_mcam103144 acquired on Sol 3662, at Sol 3658 end-of-drive location). (b) Detail of unit B from (a), highlighting planar strata parallel to the underlying unit contact and contrasting with the inclined strata of unit A (Mastcam mosaic MR_mcam102254 acquired on Sol 3562, at Sol 3560 end-of-drive location). (c) Mastcam mosaic of the north face of Bolivar butte, showing light-toned planar strata of unit B, extending laterally for ~100 m (Mastcam mosaic MR_mcam102214 acquired on Sol 3507, at Sol 3506 end-of-drive location). (d) Detail of unit B from (c) showing a prominent surface ~5 m below unit C (white arrows) and planar strata delineated by black lines. Image credits: NASA/JPL-Caltech/MSSS.

between the deposition of the sandsheets in unit B (Section 4.2.1) and the subsequent deposition of unit D. Unit B must have also been sufficiently coherent and indurated to fracture in a brittle manner without significant deformation of the original sedimentary structures (e.g., Banham et al., 2024b; Kocurek & Hunter, 1986; McMahon et al., 2017). Cross-cutting relationships, where south-dipping fractures intersect adjacent V-shaped wedges, may suggest multiple fracturing phases. Reactivation and propagation of original fracture sets could also have been caused by subsequent loading stresses (e.g., McMahon et al., 2017). The geometry of the lower contact of unit C, characterized by a cycloidal-like pattern and downward-tapering V-shaped wedges (Figure 10c), along with the fracture sets, is consistent with contraction or contraction-expansion processes (e.g., Kocurek & Hunter, 1986). In aeolian settings, such processes can result from wetting-drying cycles, thermal contraction, or freeze-thawing (Banham et al., 2024b; Dal Bó et al., 2010; Kocurek & Hunter, 1986; Mescolotti et al., 2019; Rodríguez-López et al., 2022).

The mottled texture, softness, and coloration identified in unit C, coupled with heterogenous chemistry identified in the ~0.4 m of elevation below unit D (Thompson et al., 2024), reflects surface alteration at the time of fracture formation. This is supported by elevated Cl, the presence of hematite, and distinct multispectral variations compared to the surrounding strata (Farrand et al., 2025; Thompson et al., 2024). Farrand et al. (2025) proposed that this alteration may be attributed to wetting-drying cycles due to the association with the overlying unit D that has been interpreted as a lacustrine environment (Section 4.3.1; Gupta, Dietrich, Lewis, Kite, et al., 2023; Mondro, Grotzinger, et al., 2025; Weitz et al., 2023). Short-lived wetting-drying cycles can produce wedge-shaped desiccation cracks reaching depths of 0.3 m that can be infilled with contrasting facies (e.g., Mescolotti et al., 2019). More prolonged wetting-drying cycles may lead to in situ alteration, characterized by wedge-shaped peds and paleosol development (Ahmad, 1996; Dal Bó et al., 2010). However, formation of V-shaped wedges in both scenarios requires significant clay content (Basilici & Dal'Bó, 2010; Basma et al., 1996; Harianto et al., 2008), which is absent in unit C (e.g., Farrand et al., 2025; Thompson et al., 2024), making wetting-drying cycles an unlikely source of the fracturing.

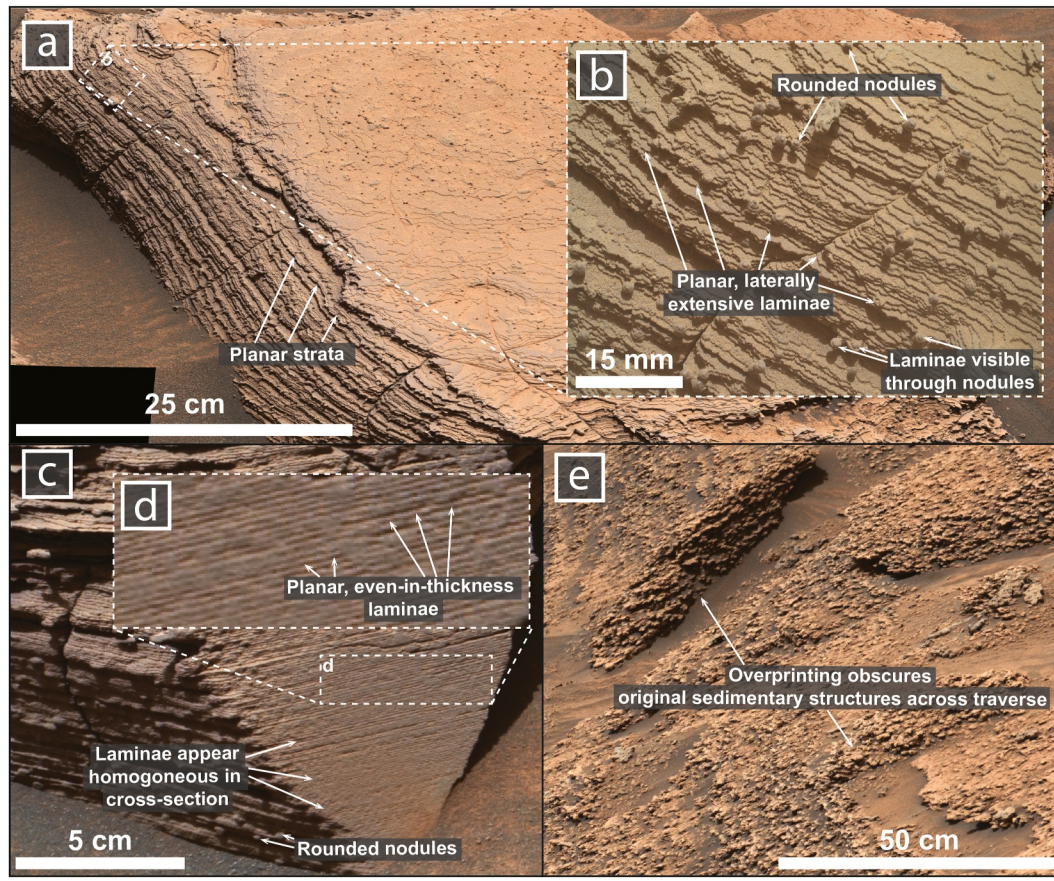

Figure 9. Examples of select facies characteristic of unit B as encountered across the traverse. (a) Mastcam mosaic of the light-toned, planar, laterally extensive laminae at the Canaima drill location on an out-of-situ block. (Mastcam mosaic MR_mcam102841 acquired on Sol 3610, at Sol 3608 end-of-drive location.) (b) MAHLI detail of (a). Note how planar the laminae appear in planform. (c). Mastcam mosaic showing cross-section view of the laminae on an out-of-situ block. (mastcam mosaic MR_mcam102798 acquired on Sol 3602, at Sol 3601 end-of-drive location.) (d) Detail of (c). Note how homogenous laminae appear in cross-section. (e) Mastcam mosaic of unit B bedrock as encountered across the rover's traverse when in situ. Extensive overprinting obscures the original sedimentary structures (Mastcam mosaic MR_mcam103352 acquired on Sol 3705, at Sol 3703 end-of-drive location.) Image credits: NASA/JPL-Caltech/MSSS.

Other contraction-expansion mechanisms that do not require clay, such as thermal contraction (Kocurek & Hunter, 1986) or even freeze-thaw cycles (Banham et al., 2024b; Benison, 2019), also align well with the cycloidal geometry of the contact and the downward-tapering wedges and their regional extent. In both cases, sediment cemented by sulfates from evaporated groundwater was proposed as the mechanism for early cohesion (Benison, 2019; Kocurek & Hunter, 1986). Tapered fractures have also been found in modern day salar flats which experience both wetting-drying cycles and extreme temperature variations (Benison, 2019). Mg sulfate has been identified in the Catrimani member (Chipera et al., 2023; Farrand et al., 2025; Thompson et al., 2024) and early cementation of this salt may have provided the necessary cohesion for fracturing and V-shaped wedge formation in unit C. Without grain size information on these wedges, this is the preferred interpretation. Subsequent fine sediment may have been windblown or waterlain to infill and overlay these cracks and then recrystallized or diagenetically altered through wetting-drying cycles and/or temperature extremes.

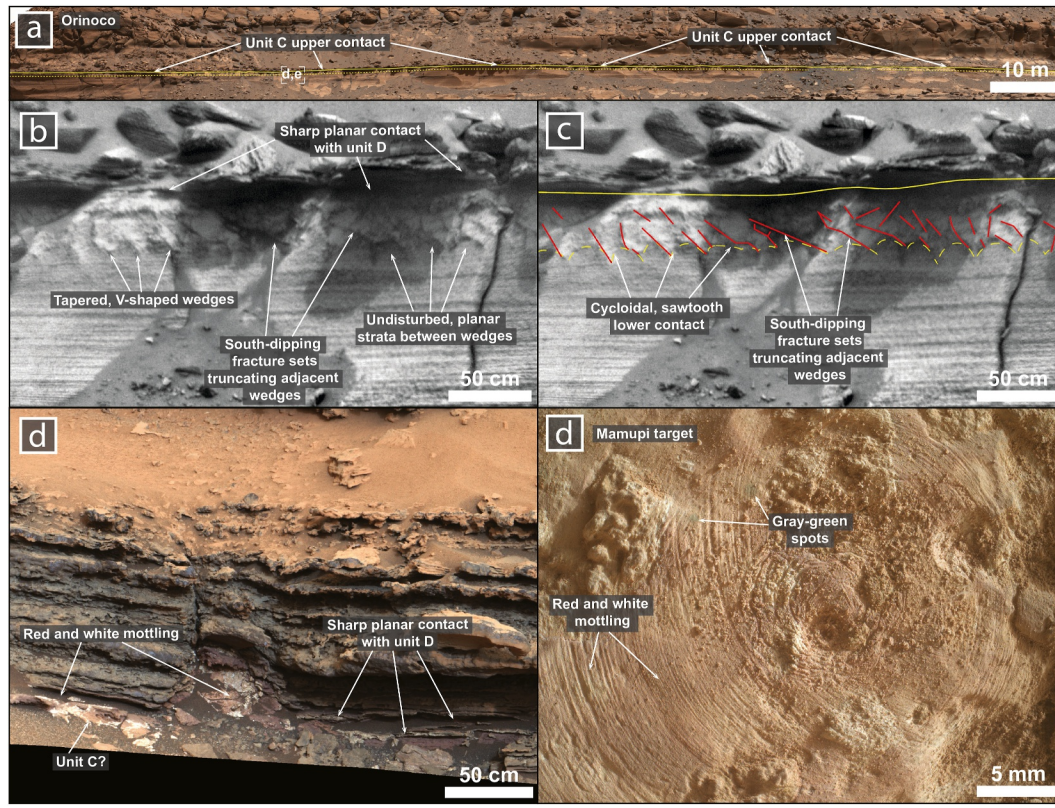

Figure 10. Outcrop expression and lithofacies of unit C. (a) Mastcam mosaic of the western face of Orinoco butte showing unit C, which is laterally extensive (~350 m) and has a thickness around ~0.3 m (Mastcam mosaic MR_mcam102754 acquired on Sol 3596, at Sol 3594 end-of-drive location). (b) Long Distance Remote Micro-Imager (LD RMI) mosaic detail of unit C from (a), highlighting a mottled, light-toned unit underlying the indurated Amapari member. (Ccam_03625, acquired on Sol 3623, at Sol 3608 end-of-drive location). (c) Interpretation of (b) showing the unit boundaries (yellow dashed lines) and inclined fracture sets (red). (d) Mastcam mosaic of bedrock with a mottled red and white texture identified under the Amapari member encountered across the traverse (Mastcam mosaic MR_mcam103019 acquired on Sol 3642, at Sol 3640 end-of-drive location). (e) A MAHLI mosaic acquired at same location as (d) showing a red and white mottled texture. (Mamupi target, taken on sol 3605 at a 5 cm stand-off). Image credits: (a, d, e) NASA/JPL-Caltech/MSSS; (b, c) NASA/JPL/LANL/CNES/IRAP.

4.3. Amapari Member

4.3.1. Unit D

4.3.1.1. Architectural Elements

Unit D, otherwise known as the Amapari Marker Band (extensively covered in: Gupta, Dietrich, Lewis, Kite, et al., 2023; Mondro, Fedo, et al., 2025; Mondro, Grotzinger, et al., 2025; Thompson et al., 2024), outcrops as a tabular bed (~0.5–1 m) with a lower, dark-toned, rippled, resistant component and a recessive, light-toned, planar-laminated upper component. The contact between the lower and upper components is gradational. In Marker Band valley, the lower contact of unit D is predominantly planar, parallel to the underlying bounding surfaces. Outside the study area, the lower contact appears more irregular (see Mondro, Grotzinger, et al., 2025; Rapin et al., 2021). This unit is preserved as a protruding shelf in the buttes around Marker Band valley where it can be traced laterally for up to ~250 m in Mastcam images of Orinoco's eastern flank. Elsewhere, this unit acts as a cap, forming a distinctive platform over buttes and valleys, including the valley west of Chenapau where the rover traversed. Orbital mapping shows that this unit can be traced for ~80 km laterally without significant changes in morphology or composition (Meyer et al., 2025; Weitz et al., 2022).

Nearfield observations of unit D show a lower facies comprised of four resistant bedsets of symmetric ripple forms (with a ~4.5 cm wavelength; Gupta, Dietrich, Lewis, Kite, et al., 2023; Mondro, Grotzinger, et al., 2025),

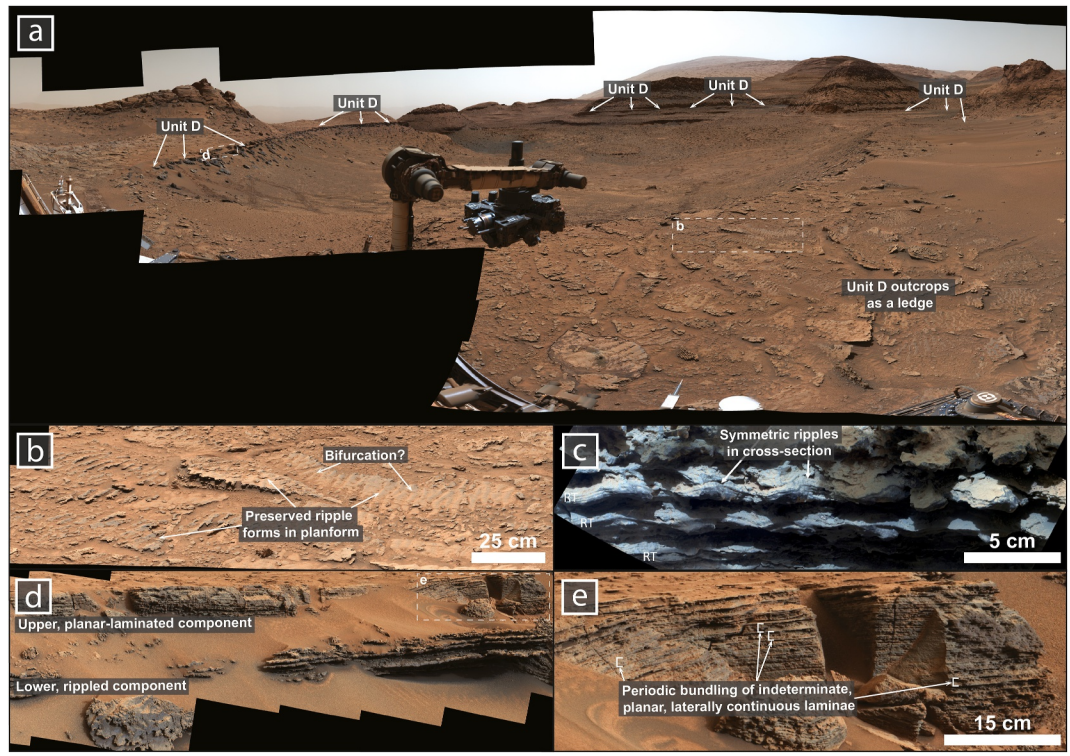

Figure 11. Outcrop expression and lithofacies of unit D (the Amapari member). (a) Mastcam panorama mosaic of unit D showing the lateral extent and outcrop expression as either a thin indurated ledge or bench (Mastcam mosaic MR_mcam103274 acquired on Sol 3684, at Sol 3672 end-of-drive location). (b) Detail of unit D from (a), highlighting 2D preserved ripple forms in planform view. (Mastcam mosaic MR_mcam103228 acquired on Sol 3674, at Sol 3672 end-of-drive location). (c) A MAHLI dogseye mosaic of the symmetrical ripples that comprise the lower-component of the Amapari member. (Mixiguana target, 25 cm stand-off). (d) Mastcam mosaic of the lower rippled component and the upper planar-laminated component that comprise unit D. Note the more recessed appearance of the upper component. (Mastcam mosaic MR_mcam103019 acquired on Sol 3642, at Sol 3640 end-of-drive location). (e) Detail of (d) showing the periodic bundling of the planar, laterally continuous laminae of the upper component of unit D. Image credits: NASA/JPL-Caltech/MSSS.

that are organized as stacked or upbuilding chevrons (Gupta, Dietrich, Lewis, Kite, et al., 2023; Mondro, Grotzinger, et al., 2025). In plan-view, ripple crestlines are 2D, generally straight, with strikes orientated at ∼120°/300° that occasionally bifurcate (Gupta, Dietrich, Lewis, Kite, et al., 2023; Mondro, Grotzinger, et al., 2025). The upper component of unit D comprises periodic, ∼1 cm thick bundles of laminae (Lewis et al., 2023; Mondro, Grotzinger, et al., 2025). These sets are planar, homogenous, laterally continuous over meters (Figures 11d and 11e), and overlie underlying laminae sets concordantly with no visible truncations. Laminae are often indeterminate. However, when visible, a single lamina often preserves a thickness that is smaller than 0.5 mm, ranging between 0.2 and 0.4 mm thickness. These laminae are dark gray in color and have a slight lustre. Laminae sets thin upwards to 0.4 cm thick laminae at the contact with the overlying unit (Figure 11; Lewis et al., 2023; Mondro, Grotzinger, et al., 2025).

4.3.1.2. Interpretations

Unit D, is interpreted as a shallow lake deposit dominated by symmetrical wave ripples formed under oscillatory wave action (Mondro, Grotzinger, et al., 2025). The presence of symmetrical ripple forms, with rounded crests and stacked chevrons, indicates sediment accretion through vertical upbuilding in response to wave-driven oscillatory flow (Gupta, Dietrich, Lewis, Kite, et al., 2023). The short crest-to-crest wavelengths (∼4.5–5 cm) suggest formation in shallow water depths, where the lake surface was open to the atmosphere and being acted upon by wind (Gupta, Dietrich, Lewis, Kite, et al., 2023; Mondro, Grotzinger, et al., 2025). To form wave-generated ripples, a water depth of less than ∼2 m would have been required (Mondro, Fedo, et al., 2025).

While the planar and laterally extensive nature of the laminae in the upper component of unit D is superficially similar to the laminae identified in units B and A, the color, thickness, absence of any preserved truncation, and distinct bundling into cm-scale sets are distinct from unit D alone. These characteristics and the gradational contact with the underlying rippled lower component are consistent with the subaqueous settling of fines in a deepening lake (Gupta, Dietrich, Lewis, Kite, et al., 2023). The 0.2–0.4 mm thicknesses of the laminae are also consistent with previously identified lacustrine laminae on Mars (Edgar et al., 2020). Depositional cyclicity is also inferred from the presence of the repeated bundles of laminae (Lewis et al., 2023; Rapin et al., 2025). The lateral continuity of the ripples in this unit, traceable for hundreds of meters (Mondro, Grotzinger, et al., 2025), and as this dark-toned band is visible for over 80 km in orbital data may imply that this shallow lake was large, potentially rising and expanding outside of Marker Band valley (Mondro, Grotzinger, et al., 2025).

4.4. Chenapau Member

4.4.1. Unit E

4.4.1.1. Architectural Elements

Unit E outcrops as a scarp-forming, ∼3.6 m thick, tabular bed, that is, planar stratified. The basal contact of unit E is marked by a resistant band (∼1–2 cm thick) that maintains lateral continuity for over 100 m without interruptions, overprinting both the contact and overlying laminae and corresponding with a subtle overhang. Immediately above the resistant band, the lower component of this unit (∼20 cm thick) is comprised of undulatory, parallel laminae that appear to have been upwarped, forming occasional cusps (Figure 12c; individual cusps are up to ∼10 cm in width). Resistant and recessive bands, primarily associated with these undulatory laminae, are observed locally but are not consistently across all near-field outcrops. These laminae transition upwards into facies comprising planar, parallel laminae (∼1 mm thick) that are laterally extensive on a meter to decameter scale (Figure 12c). Up section, unit E transitions from an overhanging escarpment to a more gently sloped and recessed profile (Figure 12a).

An indurated, dark-toned lens (∼7 m × ∼0.5 m) is embedded near the uppermost extent of unit E (Figure 13). The lens exhibits a sharp upper and lower contact with the surrounding bedrock. The lens is U-shaped, asymmetric, and exhibits a lateral pinching to the south with a wing-shaped geometry (Roberts et al., 2025). Internally, the lens is composed of amalgamated bedsets of centimetre-scale tabular cross-bedding dipping to the northeast (Figures 13b and 13c). This feature contrasts sharply with the surrounding unit E material in both tone and resistance.

The contact between unit D and unit E is defined by an abrupt change from planar laminae to a massive nodular zone (Figures 12d and 12e). The nodules commonly obscure primary sedimentary structures and, at the basal contact, are organized into irregular, branching forms, which vary in size (1–10 mm thick; Figure 12e). These nodules are roughly aligned in layers and become smaller and less abundant higher in the section, where planar laminae are more apparent (Figure 12d).

4.4.1.2. Interpretations

We interpret that the sharp, planar, laterally extensive basal contact and the change in lithofacies marks a transition from the lacustrine conditions of unit D. The steep, overhanging escarpment at the base of unit E also has a differential erosional pattern to the underlying unit D, further supporting a change in sedimentary texture such as grain size, sorting, or cementation (e.g., Edgett & Sarkar, 2021). However, the original sedimentary structures have been overprinted by diagenesis, making its precise depositional setting uncertain. Roberts et al. (2025) interpreted that the dark-toned lens embedded within unit E–with the asymmetric central body, wing-shaped features, and cm-scale amalgamated bedsets of tabular cross-stratification–is consistent with fluvial erosion and infill. We subsequently interpret that fluvial scouring and infill within unit E indicates that the unit must have been deposited in a subaerial environment.

At the base of unit E, diagenetic overprinting complicates direct evidence of a typical regressive sequence expected from a transition from lacustrine to aeolian deposition. Parallel, undulating laminae laterally transition into a massive bed comprised of branching nodular aggregates which appear superficially similar to salt-crust draping and popcorn salt aggregates from primary evaporite deposition (Goodall et al., 2000). However, the planar transitions of laminae into nodules suggest that these nodules were formed primarily through overprinting by

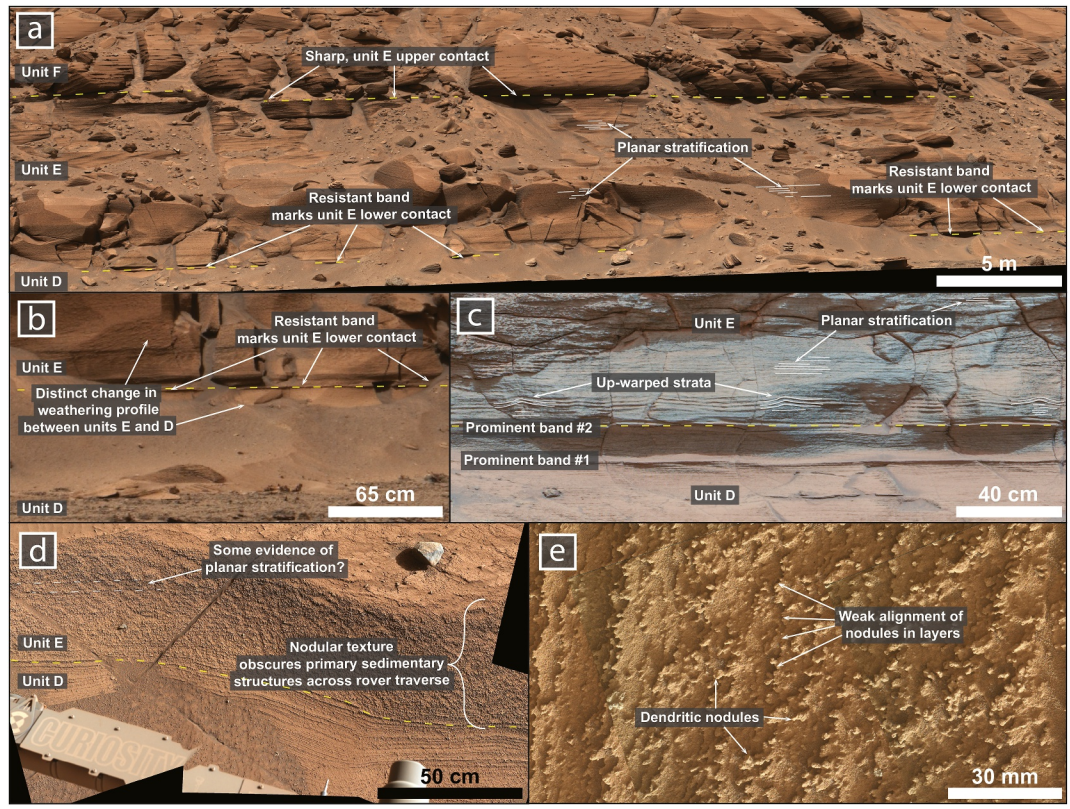

Figure 12. Outcrop expression and lithofacies of unit E. (a) Mastcam mosaic of the western face of Chenapau, showing the laterally extensive, sharp upper and lower contacts of unit E (mastcam mosaic MR_mcam103485 acquired on Sol 3727, at Sol 3724 end-of-drive location). (b) Detail of (a), highlighting the distinct change from a more recessed and slope forming weathering profile of the upper component of unit D to the more resistant and scarp-forming weathering profile of unit E. Note the resistant band, which marks the lower contact of unit E (Mastcam mosaic MR_mcam103386 acquired on Sol 3710, at Sol 3708 end-of-drive location). (c) Mastcam mosaic of the Amapa butte showing the continuous planar stratification of unit E in cross-section. Note localized upwarping at the base and the two prominent bands which delineate the lower contact with unit D. (Mastcam mosaic MR_mcam103387 acquired on Sol3711, at Sol 3708 end-of-drive location). (d) Mastcam mosaic showing a sharp transition from unit D into a nodular texture which obscures primary sedimentary structures as encountered across the rover traverse, inferred as the contact with unit E. (Mastcam mosaic MR_mcam103736 acquired on Sol 3771, at Sol 3771 end-of-drive location). (e) MAHLI mosaic at the location of (d) showing that nodules exhibit a weak alignment into apparent layers. (Santa Elena de Uairen target, 25 cm stand off). Image credits: NASA/JPL-Caltech/MSSS.

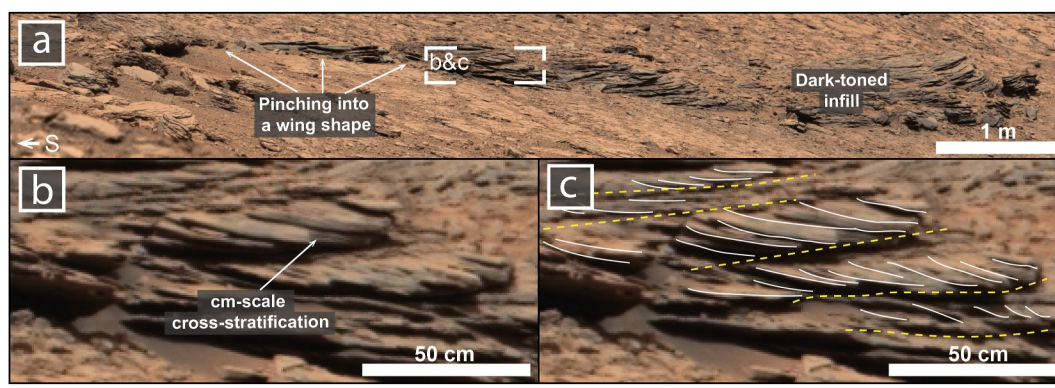

Figure 13. U-shaped scour embedded in unit E as encountered along the Canta detour. (a) Mastcam mosaic of the scour-and-fill structure. Note the dark-toned infill and how the scour pinches out into a wing-shape (mastcam mosaic MR_mcam103090 acquired on Sol 3653, at Sol 3651 end-of-drive location). (b) Detail showing the dark-toned scour fill. (c) Interpretation showing the cm-scale cross-bedding as described in the text. Image credits: NASA/JPL-Caltech/MSSS.

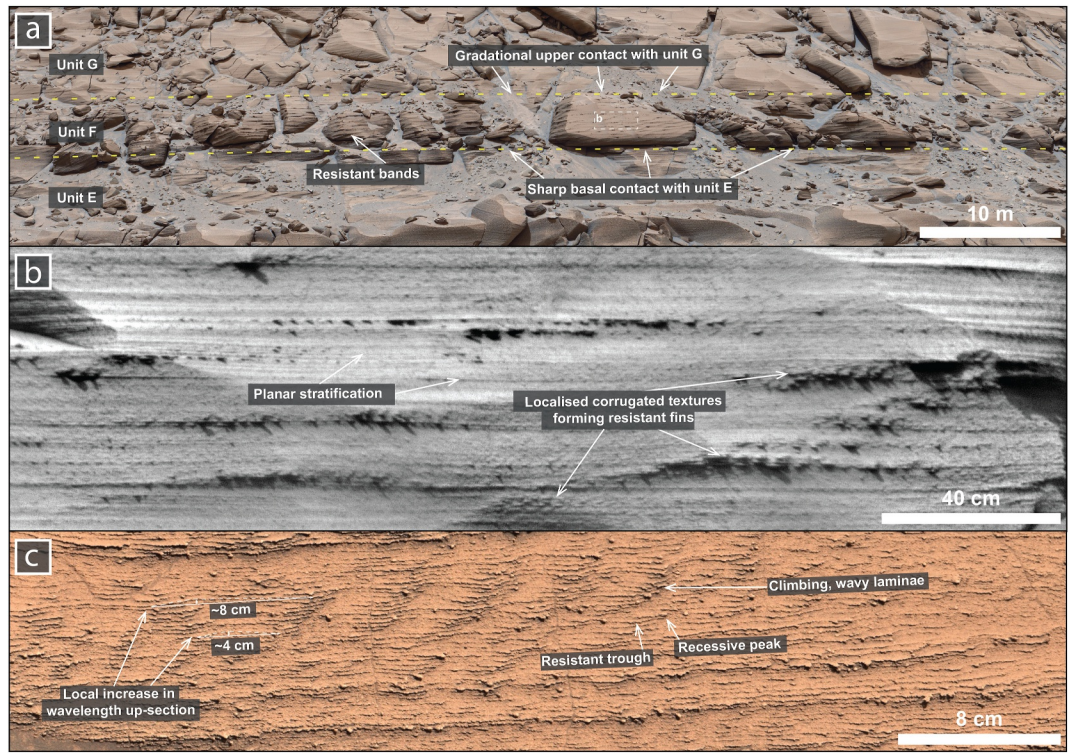

Figure 14. Outcrop expression and lithofacies of unit F. (a) Mastcam mosaic of Chenapau showing the laterally extensive sharp basal contact of unit F and the gradational upper contact with unit G. Note the dark-toned north-dipping bands. (Mastcam mosaic MR_mcam103485 acquired on Sol 3727, at Sol 3724 end-of-drive location). (b) LD RMI detail of (a) showing planar stratification and how the dark-toned resistant bands are comprised of localized, resistant, corrugated textures. (ccam_02728, acquired on sol 3728, at sol 3727 end-of-drive location). (c) Localized corrugated textures as encountered across the rover's traverse. (Mastcam mosaic MR_mcam103808 acquired on Sol 3783, at Sol 3781 end-of-drive location.) Image credits: (a, c) NASA/JPL-Caltech/MSSS; (b) NASA/JPL/LANL/CNES/IRA.

disruptive crystal growth (e.g., Ahlbrandt & Fryberger, 1981). Later, diagenesis acted to overprint the original sedimentary structures. This direct switch from lacustrine to subaerial, with no preserved regressive sequence, indicates that the wind eroded lacustrine or sabkha deposits prior to subsequent aeolian deposition, a common type of supersurface called a sand-drift surface (Clemmensen & Tirsgaard, 1990; Kocurek, 1998).

4.4.2. Unit F

4.4.2.1. Architectural Elements

Unit F is a ~4.2 m thick, planar-stratified, scarp-forming unit with corrugated textures arranged in north-dipping ridges (Figure 14). The basal contact is sharp, planar, and conformable, marked by a slight overhang as unit F overlies the recessed unit E below (Figure 14a). Unit F is traceable for approximately ~350 m laterally across Orinoco, ~125 m in Chenapau, and across the valley walls (Figure 14). In cross-section, unit F is characterized by light- and dark-toned interbedded sets (1–4 cm thick; Figure 14b) and localized corrugated textures. The corrugated textures are comprised of rounded protrusions (2–4 cm wide), relatively uniform in spacing, that are aligned along laminae.

Nearfield observations of in situ outcrops of Unit F reveal a facies composed of sets (~2–14 cm thick) of localized wavy and planar laminae (Figure 14c). Troughs protrude, while crests are more recessed, creating a corrugated appearance. These wavy laminae have small, mm-scale amplitudes and are irregular in both symmetry (3.58–2.17 ripple-symmetry index) and wavelength (ripple crest-to-crest spacing between ~2 and 8 cm) both laterally and vertically (Figure 14c). Ripple-forms appear to climb in an atypical fashion, appearing to upbuild against the stoss side and gradually increasing in wavelength up section (Figure 14c). Millimeter-scale nodules are interspersed throughout and often overprint original sedimentary structures.

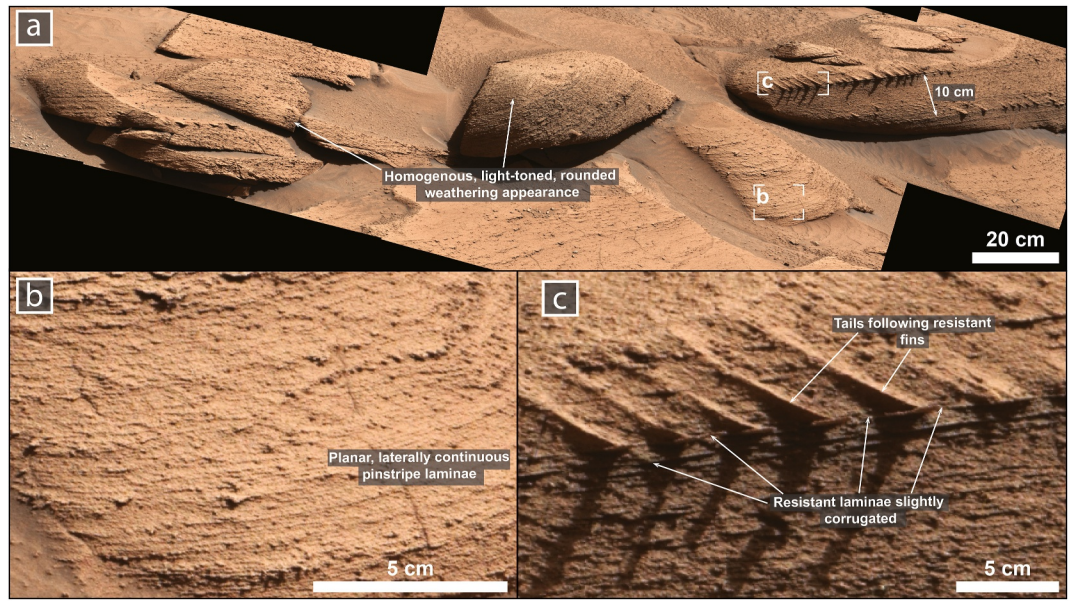

Figure 15. Outcrop expression and lithofacies of unit G. (a) Mastcam mosaic of unit G as encountered across the rover traverse. Note the distinctive, light-toned, rounded, homogenous appearance of the blocks. (Mastcam mosaic MR_mcam103899 acquired on Sol 3798, at Sol 3797 end-of-drive location). (b) Detail of (a) showing the homogenous, mm-scale, planar, laterally extensive laminae which comprise unit G. (c) Detail of (a) showing how the sporadic, discontinuous, resistant, fin-forming laminae have a slight corrugation. Note the tails following the resistant fins caused by subsequent wind erosion. Image credits: NASA/JPL-Caltech/MSSS.

4.4.2.2. Interpretations

The wavy laminae comprise candidate climbing ripple forms (Figures 14b and 14c). If deposited under dry aeolian conditions, the asymmetric appearance, amplitudes only a few mm thick, and wavelengths between 2 and 4 cm could be consistent with supercritically climbing aeolian wind-ripples (Clemmensen & Dam, 1993; Hunter, 1977). Thick successions of supercritically climbing wind ripples are also not unusual in terrestrial aeolian sandsheet deposits (Basilici & Dal'Bó, 2014; Simplicio & Basilici, 2015). Alternatively, a damp aeolian origin is also consistent with the observed sedimentary structures. The small-amplitude, upwind-aggradational climbing geometry, combined with irregular ripple spacing and variable symmetry index, aligns with climbing adhesion ripples, where sediment accumulates vertically on a damp ripple surface rather than migrating laterally (Clemmensen et al., 1989; Goodall et al., 2000; Jones et al., 2016; Kocurek & Fielder, 1982; Mountney & Thompson, 2002). Such adhesion deposits can form thick, laterally extensive successions in terrestrial aeolian sandsheets (Mesquita et al., 2021). The wavy laminae appear superficially similar to supercritically climbing aqueous ripples in non-channelized fluvial deposits from flooding of interdunes (Chakraborty & Chakraborty, 2001; Trewin, 1993). However, no other associated fluvial features are observed; aqueous conditions rarely persist long enough to generate more than a couple of sets of supercritically climbing ripples; the irregularity of ripple forms and spacing is inconsistent with water-lain deposition; and these wavy laminae appear distinct to aqueous ripples formed within the dark-toned, indurated unit D, the fluvial lens in unit E, and other fluvial lenses observed in the Mirador formation (Caravaca et al., 2025; Gupta, Dietrich, Lewis, Kite, et al., 2023; Mondro, Grotzinger, et al., 2025; O'Connell-Cooper et al., 2025). Thus, a subaqueous origin is unlikely. Consequently, we interpret unit F as a product of sustained aeolian sedimentation, where wind or adhesion processes may have controlled the accumulation of the wind ripple strata.

4.4.3. Unit G

4.4.3.1. Architectural Elements

Unit G outcrops as a 2.7 m thick, slope-forming, light-toned tabular bed comprised of planar stratification with sporadic, discontinuous horizons of resistant fins (Figure 15). Unit G exhibits a gradational, basal contact from the underlying unit F marked by the gradual absence of wavy or corrugated strata.

Along the rover traverse, outcrops of unit G are distinct for their homogenous, light-toned, rounded weathering profiles (Figure 15). Near-field images revealed lithofacies marked by horizontal to low-angle, planar-parallel laminae organized into sets ∼40 cm in thickness but thin to ∼11 cm up section. These laminae were remarkably even in thickness (∼1 mm), homogenous, and laterally extensive (Figure 15b), similar in appearance to the planar laminae observed in unit B (Section 4.2.1). Individual laminae could be traced over several meters (Figure 15a). These laminae were occasionally, disconcordantly truncated by planar bounding surfaces at a low angle.

Discontinuous laminae of resistant "fins" or "protrusions" are sporadically distributed throughout the unit, aligned with set bounding surfaces (Figure 15c). These resistant laminae extend laterally over distances of 40 cm to 1 m. The fin-forming, dark-toned, indurated horizons have a slight corrugation on the mm-scale (Figure 15). Equally spaced fins (∼4 cm spacing) protrude for 5–10 cm from the rock and are associated with troughs in the corrugations. Rover-disturbed surfaces showed that the laminae were medium gray in color (Figure 15c). Randomly distributed, millimeter-scale nodules are also common throughout this unit. Occasionally, raised "tails" emerge from protrusions, pointing upslope and to the south (e.g., Zhou et al., 2025).

4.4.3.2. Interpretations

Both the sedimentary architecture and lithofacies of unit G, with the planar stratification and the fine, even-in-thickness, parallel, laterally extensive laminae are similar in appearance to unit B (Section 4.2.1), indicating a return to deposition in an aeolian sandsheet environment. The widespread occurrence of these deposits, laterally continuous for hundreds of meters across Marker Band valley, would mean that sand supply or availability was too restricted for extensive dune construction when these deposits accumulated (Kocurek & Lancaster, 1999; Loope & Simpson, 1992; Mountney, 2006b).

We interpret that the induration and dark-coloring of the "fin-forming" resistant laminae occurred after lithification, through early cementation or diagenesis exploiting variations in sedimentary texture that influenced fluid flow. Their alignment along bounding surfaces implies a connection between erosive events that truncated the lamina sets and the development of these indurated horizons. The corrugated appearance of these surfaces could have resulted from wind action when the otherwise dry sand-sheet deposits were intermittently damp, where capillary action results in mm to cm-scale topography during erosion (Kocurek, 1981). Discontinuous deposition of even a small amount of fine-clays, cements, or adherence of fine sand settling from suspension at the surface during damp or wet intervals (e.g., Chakraborty & Chakraborty, 2001; Murton et al., 2025) may have impacted the fluid retention properties, leading to preferential diagenesis or cementation at these intervals.

Tails carved into the bedrock behind the fins formed when these more resistant ridges shielded the adjacent laminae from upslope wind erosion, resulting in differential exhumation (e.g., Zhou et al., 2025).

4.4.4. Unit H

4.4.4.1. Architectural Elements

Unit H, ∼5.3-m-thick, appears as a dark-toned scarp-forming stratigraphic interval characterized by light-toned recessive sets of planar laminae separated by thin indurated strata (Figures 16 and 17). This unit is laterally extensive, traceable for approximately 250 m in the Orinoco butte and 125 m in the Chenapau butte, and forms a cap on the first ledge in Ascent Valley. The basal contact of unit H is gradational, marked by both an increase in the number of horizons of interbedded indurated laminae and their lateral extents. Truncating unit H are a set of nine distinct, broad, concave-up scour-and-fill structures (∼60 to ∼40 m × ∼1–4 m). The scours are simple, symmetric, with occasional planar bases, infilled by Unit I (Figure 16a; Roberts et al., 2025).

Across the traverse, unit H was easily recognized for the distinct weathering appearance of more angular blocks with interbedded recessive and thin resistant strata that give a distinctly "etched" appearance (Figure 16c). Nearfield images revealed that unit H is comprised of tabular sets that are between ∼1 and 12 cm thick, consisting of planar-parallel laminae, each composed of a thicker light-toned component and a thin dark-toned component, forming a "pinstripe" pattern (Figure 17a). In some sections (Figure 17a), the laminae were heterogenous in thickness (ranging from ∼1 to ∼3 mm), differing from the homogenous laminae that comprise units B and G but were still laterally extensive. Thicker laminae are often associated with more etched surfaces (Figures 17a and 17b). In other sections, the laminae appeared more like the homogenous "pinstripe" laminae in units B and G, with

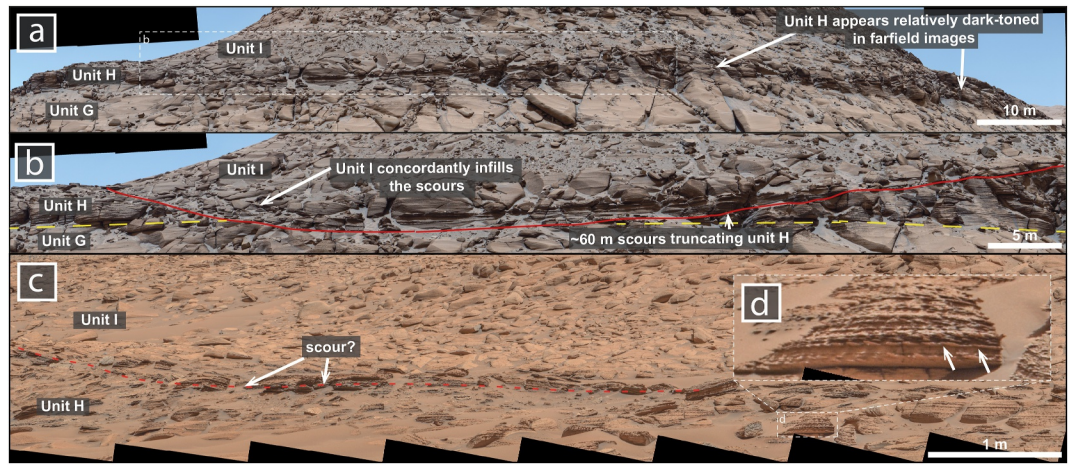

Figure 16. Outcrop expression and lithofacies of unit H. (a) Mastcam mosaic of the western face of Chenapau, showing the lateral extent of unit H (mastcam mosaic MR_mcam103485 acquired on Sol 3727, at Sol 3724 end-of-drive location). (b) Detail of (a) showing one of the ∼60 m scours truncating unit H and concordantly infilled by unit I. (c) Mastcam mosaic of unit H as encountered across the rover traverse. Note the characteristic dark-toned, interbedded resistant and recessive weathering expression and the potential scour truncating the unit H. (Mastcam mosaic MR_mcam103913 acquired on Sol3800, at Sol 3799 end-of-drive location). (d) Detail of (c) showing how resistant strata have a corrugated appearance. White arrows point out the apparent micro-paleotopography of the surfaces. Image credits: NASA/JPL-Caltech/MSSS.

the laminae themselves exhibiting less pronounced etching (Figure 17b). Occasional isolated ripple structures with planar bases were also identified (Figures 17b and 17c). Overlying laminae commonly drape over the "frozen" ripple form.

Sets are often separated by indurated dark-toned laminae. These indurated laminae appear dark-toned, flaky, and often weather to form elongated, parallel fins spaced at ∼4–5 cm intervals. Occasionally, these appear to have a slight corrugated appearance (Figure 17a) and can be traced across the outcrop for up to ∼3 m. In plan view, the resistant laminae appear dark-toned and comparatively smooth at a mm scale. In contrast, the light-toned laminae have a rougher surface texture, composed of sub-rounded, sub-mm-scale protrusions that appear granular.

Toward the upper portion of the unit, a distinctive 1 m-thick interval contains small disc- or "coin"-shaped fragments that spall from bedding planes (Figure 17d–17g). This interval is predominantly composed of irregular, laterally extensive laminae (Figures 17d and 17e). Small lenses of corrugated, discontinuous laminae are also present. These corrugated laminae were more indurated and resistant and were the source of the spalling clasts. Sets of weakly undulating and irregular cross-strata measuring 0.7–1 cm thick and dipping to the north/north-east were also identified (Figure 17d). Plan view observations of bedding surfaces at the clast-bearing interval show mm-scale needle- or diamond-shaped particles aligned horizontally along the bedding plane (Figure 17f). Displaced, rounded light-toned blocks comprised of planar laminae with cm-scale lenses of dark-toned planar laminae were also identified within this upper portion, but their relationship with the stratigraphy is unknown.

4.4.4.2. Interpretations

Similar to unit A (Section 4.1.1), we interpret that the "pinstripe" appearance is a result of wind-ripple deposits undergoing preferential early diagenesis or cementation (Fryberger & Schenk, 1988; Mountney, 2006a). We interpret that these pinstripe laminae become distinctly "etched" on more weathered faces, creating a resistant-recessive appearance, where wind exploits subtle changes in weathering resistance over long periods of time (e.g., Fryberger & Schenk, 1988). The planar-parallel appearance of the laminae and the tabular nature of the beds led us to interpret that unit H is still deposited in a sandsheet environment.

We also interpret that there was a gradual shift in the surface conditions to explain the differences with the lithofacies of unit G. The textural heterogeneity of unit H compared to unit G, however, represents less uniform and less sand-saturated conditions during deposition of unit H (Fryberger et al., 1979; Kocurek, 1981). Sets were also smaller, marking an increase in truncation surfaces and the termination of aeolian deposition (Kocurek & Nielson, 1986) supporting less continuous wind conditions and sediment-supply limited systems (Kocurek &

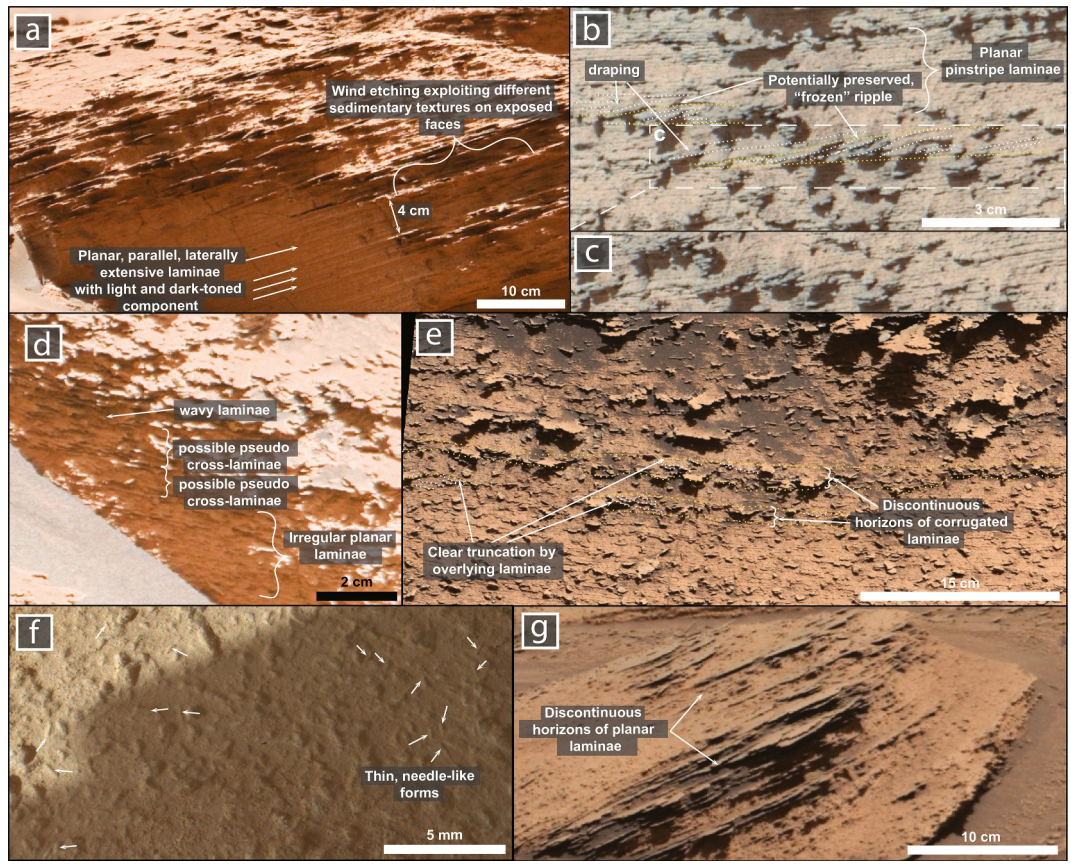

Figure 17. Examples of select facies characteristic of unit H as encountered across the traverse. (a) Mastcam mosaic showing resistant laminae separating cm-scale sets of recessive laminae (mastcam mosaic MR_mcam103951 acquired on Sol 3807, at Sol 3805 end-of-drive location). (b) Annotated mastcam mosaic showing sporadic "frozen" ripple forms interbedded with planar pinstripe laminae (mastcam mosaic MR_mcam104018 acquired on Sol 3819, at Sol 3815 end-of-drive location). (c) Detail of (b) showing an unannotated frozen ripple. (d) Mastcam mosaic showing wavy and irregularly undulating laminae and candidate pseudo cross-laminae (mastcam mosaic MR_mcam103987 acquired on Sol 3812, at Sol 3810 end-of-drive location). (e) Annotated mastcam mosaic showing discontinuous lenses of corrugated laminae (mastcam mosaic MR_mcam103987 acquired on Sol 3812, at Sol 3810 end-of-drive location). (f) MAHLI mosaic showing randomly orientated thin needle-like forms (MAHLI mosaic of target Anortosito Repartimento, 5 cm stand-off, taken on sol 3810.) (g) Discontinuous horizons of planar, dark-toned, resistant laminae (mastcam mosaic MR_mcam104069 acquired on Sol 3831, at Sol 3815 end-of-drive location). Image credits: NASA/JPL-Caltech/MSSS.

Lancaster, 1999; Loope & Simpson, 1992; Mountney, 2006b). Occasional isolated ripples represent some sort of stabilization from grain armoring, cementation (Fryberger et al., 1979), or a rising capillary fringe "freezing" the ripple in stasis before subsequent deposition of the aeolian sand sheets (Anderson, 1990; Kocurek & Nielson, 1986).

Several processes are linked to the dark indurated laminae. As the indurated, dark-toned, fin-forming laminae appear similar in appearance to the sporadic ones identified in unit G and retain what appears to be a slight corrugation, we also interpret that many of these bounding surfaces are linked to intermittent intervals of damp conditions and irregular deflation (Figures 15c and 17; Section 4.4.3). Thick successions of interbedded damp and dry sandsheets are also common on Earth and can cause a similar "etched" resistant and non-resistant appearance (Figure 11 in Mesquita et al., 2021; also see Chakraborty & Chakraborty, 2001; Galanin, 2021; Murton et al., 2025).

Fin-forming, resistant laminae are also associated with the thicker, heterogenous pinstripe laminae. These fin-forming laminae have a slightly different appearance due to their apparent planar form and less regularly spaced fins (Figure 17). Pinstripe laminae in unit H also appear more prominent than pinstripe laminae in units B and G, leading us to interpret that a slight change in grain provenance, organization, or packing in the wind-ripple

deposits caused more pronounced preferential cementation at these intervals (Banham et al., 2024a; Besly et al., 2018; Fryberger & Schenk, 1988).

In the uppermost interval of unit H, the irregular, wavy geometry of the pseudo-cross-laminations closely resembles climbing adhesion ripples (Goodall et al., 2000; Hunter, 1973; Kocurek & Fielder, 1982). The needle/diamond shaped features observed in the MAHLI images resemble euhedral sulfate crystals that have a platy and needle-like habitat previously identified on Mars (Kah et al., 2018; Schieber et al., 2022). While we cannot determine whether these needle/diamond shaped features were detrital or synsedimentary interstitial crystals growing amongst pore spaces, both could indicate crystallization through evaporation at the surface or near the surface when the sediment was deposited (Cohen et al., 2022; Kocurek & Nielson, 1986). Discontinuous lenses of dark-toned laminae may also support brief ponding (Chakraborty & Chakraborty, 2001). Put together, we tentatively infer that these features may represent a damp or salt-cemented sabkha-like environment at the top of unit H.

The concave-up scour-and-fill structures that truncate unit H are interpreted as blowouts (further described in Roberts et al., 2025) formed by episodes of localized deflation by strong, sediment unsaturated winds (Hesp, 2002; Hugenholtz & Wolfe, 2006, 2009). Similar sized and shaped "saucer" blowouts are often associated with sabkha environments, where surficial salt cements can act to stabilize the surface (Hesp, 2002). The planar base observed in one of these scours may indicate deflation down to the water table/salt-cemented surface (Roberts et al., 2025).

4.4.5. Unit I

4.4.5.1. Architectural Elements

Unit I, with a thickness of ~4.9 m, is a light-toned slope-forming interval characterized by planar stratification appearing similar to unit G (Figure 18). The basal contact with unit H is sharp, particularly where the unit drapes across the embedded scours (Figures 16a and 18a). Unit I is laterally extensive, continuous for approximately 125 m in the Chenapau butte and 250 m in the Orinoco butte and appears homogenous in cross-section.

Along the rover's traverse, unit I is observed to be gently sloped, with weathering commonly forming rounded, smooth, light-toned blocks, similar to the weathering patterns observed in unit G and a distinct contrast to the "etched" underlying unit H (Figures 18a and 18b). However, unlike unit G, unit I lacks the discontinuous horizons of protrusions or fins, except for indurated strata in the paleo-topographic lows at the centers of the scours. The lithofacies of unit I are characterized by planar, homogenous, and laterally extensive laminae similar to unit G (Figures 18c and 18d). Like unit G, individual laminae—traced laterally for ~3 m across outcrops—demonstrate planar geometry with no thickness variation. As a MAHLI dog's eye was taken of this unit, detailed measurements of the laminae could be made showing a consistent laminae thickness, with an average thickness of ~0.76 mm and a standard deviation of 0.058 mm (Figure 18d). Like unit G, sporadic mm-scale nodules are also common in this unit.

4.4.5.2. Interpretations

The planar-parallel, homogenous laminae lithofacies arranged into tabular, planar sets observed in unit I are interpreted to represent the same lithofacies present in units B and G. We therefore interpret that unit I also represents aeolian sandsheet deposition under continuous wind conditions and a consistent sediment supply (Section 4.2). The observed concordance of the strata within unit I as they infill the underlying blowout scours that truncate unit H (Roberts et al., 2025) suggests that these deposits accumulated and draped across pre-existing paleotopographic relief—an observation consistent with accumulations of ancient terrestrial sandsheets (e.g., Langford et al., 2008). Concordant, isolated, cm-scale scours could also suggest minor erosion by either strong winds (Hesp & Hyde, 1996; Schwan, 1988) or local turbulence (Grotzinger et al., 2005) concurrent with sandsheet deposition.

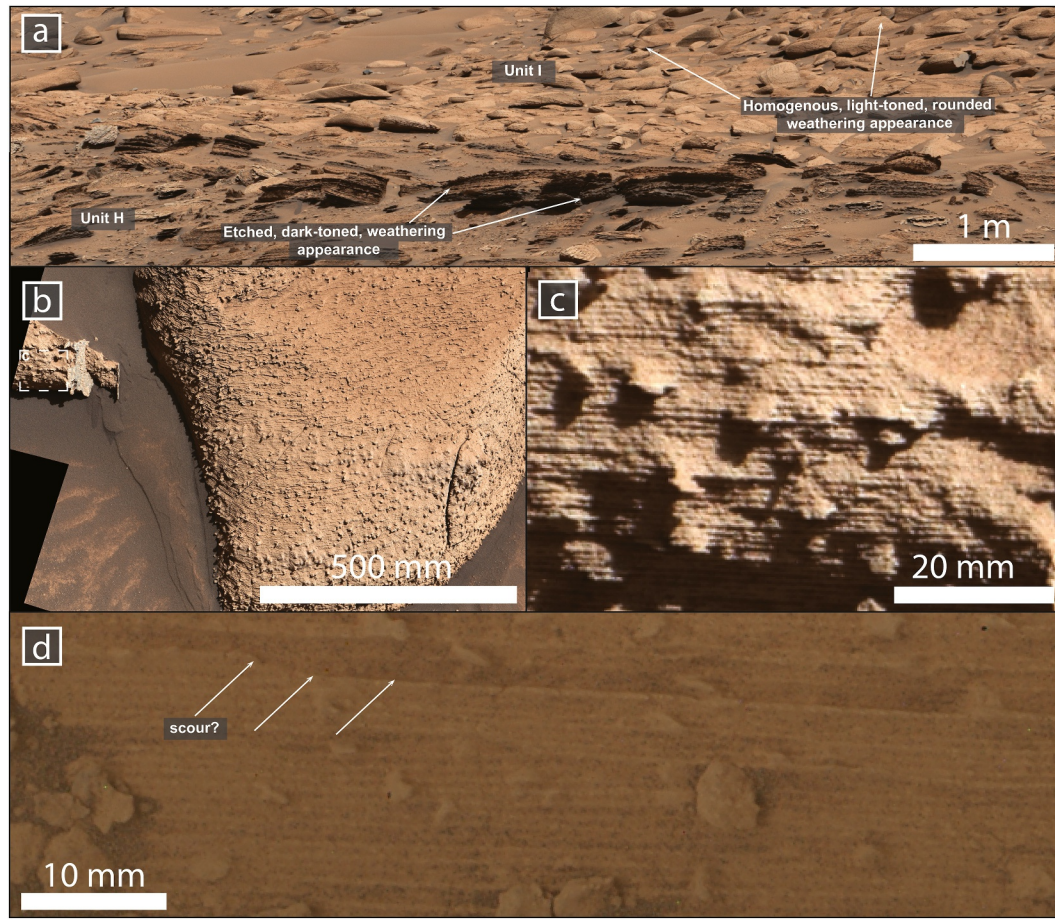

Figure 18. Outcrop expression and lithofacies of unit I. (a) Mastcam mosaic showing the difference in weathering appearance of unit I and unit H. Note how unit I appears homogenous, light-toned and weathers as rounded blocks compared to the dark-toned, etched weathered appearance of the underlying unit H. (Mastcam mosaic MR_mcam103913 acquired on Sol 3800, at Sol 3799 end-of-drive location.) (b) Mastcam mosaic showing the light-toned and homogenous appearance of unit H. (Mastcam mosaic MR_mcam104131 acquired on Sol 3845, at Sol 3843 end-of-drive location.) (c) Detail of (b) showing how the light-toned, homogenous appearance is caused by fine, equal-in-thickness, homogenous laminae. (d) MAHLI dogseye mosaic showing the homogenous, equal-in-thickness laminae. Note a potential ~cm scale scour that appears to truncate the laminae. (Kastria Spring target, 25 cm stand off.) Image credits: NASA/JPL-Caltech/MSSS.

4.4.6. Unit J

4.4.6.1. Architectural Elements

Unit J, ~7.3 m thick, is a dark-toned scarp-forming stratigraphic interval, characterized by interbedded recessive and thin resistant strata sets similar in appearance to unit H. The basal contact of unit J is gradational with the underlying unit I and is defined by an increased presence of laterally continuous resistant strata. Unit J extends across ~250 m of Orinoco and ~125 m of Chenapau. One scour (~60 m wide, ~5 m thick) is observed in Orinoco, truncating the planar stratification of unit J. This scour is also symmetric and infilled with the light-toned planar strata characteristic of unit K (Figure 19a).

Like unit H, unit J was easily recognized across the traverse for the distinct weathering pattern that formed angular blocks with an etched appearance similar to unit H (Figures 19a, 19b and 20a, 20b). Unit J was also comprised of tabular sets of recessive light-toned laminae separated by discontinuous resistant fin-forming laminae that occasionally appeared corrugated (Figures 19b and 19c) and occasional "frozen ripples" (Figure 19d). Unlike unit H, unit J exhibits occasional scours truncating the strata (Figure 19c).

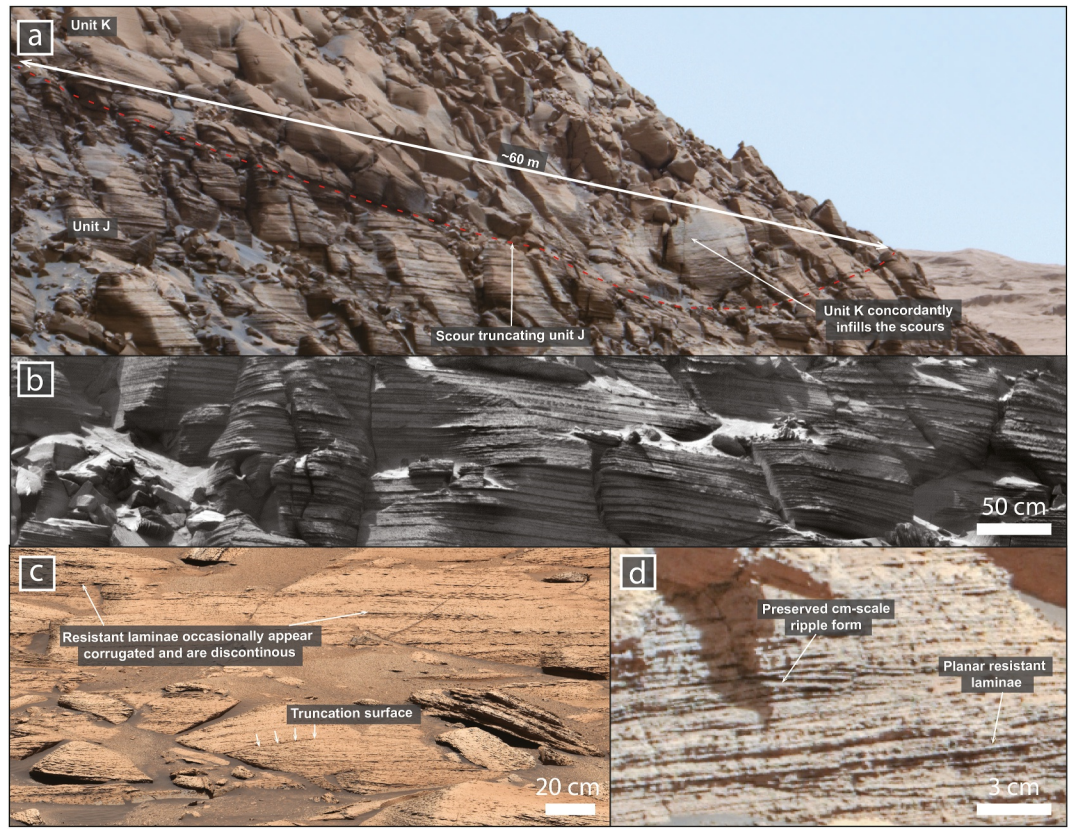

Figure 19. Outcrop expression and lithofacies of unit J. (a) Mastcam mosaic showing the dark-toned planar lithofacies of unit J within the western face of Chenapau. Note the ~60 m scour (see Roberts et al., 2025). (mastcam mosaic MR_mcam103485 acquired on Sol 3727, at Sol 3724 end-of-drive location). (b) LD RMI showing how the dark-toned planar-bedded lithofacies comprise interbedded resistant and recessive strata (ccam_02737, acquired on sol 3737, at sol 3735 end-of-drive location). (c) Interbedded resistant and recessive packages as encountered along the rover traverse. Note how the resistant laminae occasionally appear corrugated and discontinuous and the truncated surface. (mastcam mosaic MR_mcam104297 acquired on Sol 3871, at Sol 3870 end-of-drive location). (d) Preserved cm-scale ripple form identified in one of the sets (mastcam mosaic MR_mcam104379 acquired on Sol 3885, at Sol 3880 end-of-drive location). Image credits: (a, c, d) NASA/JPL-Caltech/MSSS; (b) NASA/JPL/LANL/CNES/IRAP.

The light-toned, recessive sets are comprised of planar-parallel, laterally extensive laminae that have a pinstripe pattern (Figures 20a and 20b). Like unit H, these laminae are heterogeneous in thickness but are not associated with an etched appearance. The dark-toned laminae separating the sets correspond to bounding surfaces that truncate the light-toned laminae (Figure 20a). The dark-toned resistant laminae have a variety of textures. Some have gently irregular and undulating surfaces (Figure 20c), while others form parallel finger-like ridges that occasionally display a dendritic pattern, in one case associated with raised dark-toned polygonal ridges (Figure 20d). Other surfaces appear to drape across U-shaped grooves in the light-toned recessive laminae (Figure 20e). Similar to unit H, the resistant laminae appear smoother on a micro-meter scale and lack the distinctive granular or nodular appearance.

4.4.6.2. Interpretations

The resistant-recessive, planar-parallel, heterogenous laminated sets observed in unit J resemble the lithofacies observed in unit H (Section 4.4.4). Similarly, we interpret that unit J was deposited in a similar aeolian sandsheet environment as unit H characterized by non-uniform winds undersaturated in sand.

The mm-scale corrugated and irregular appearance of the dark-toned laminae in plan-view appears superficially similar to adhesion surfaces in plan-view (Basilici et al., 2021; Kocurek & Fielder, 1982). The finger-like, dendritic, dark-toned ridges and draping appear superficially similar to textures/facies that result from brief ponding during termination of aeolian deposition (e.g., Chakraborty & Chakraborty, 2001; Kocurek &

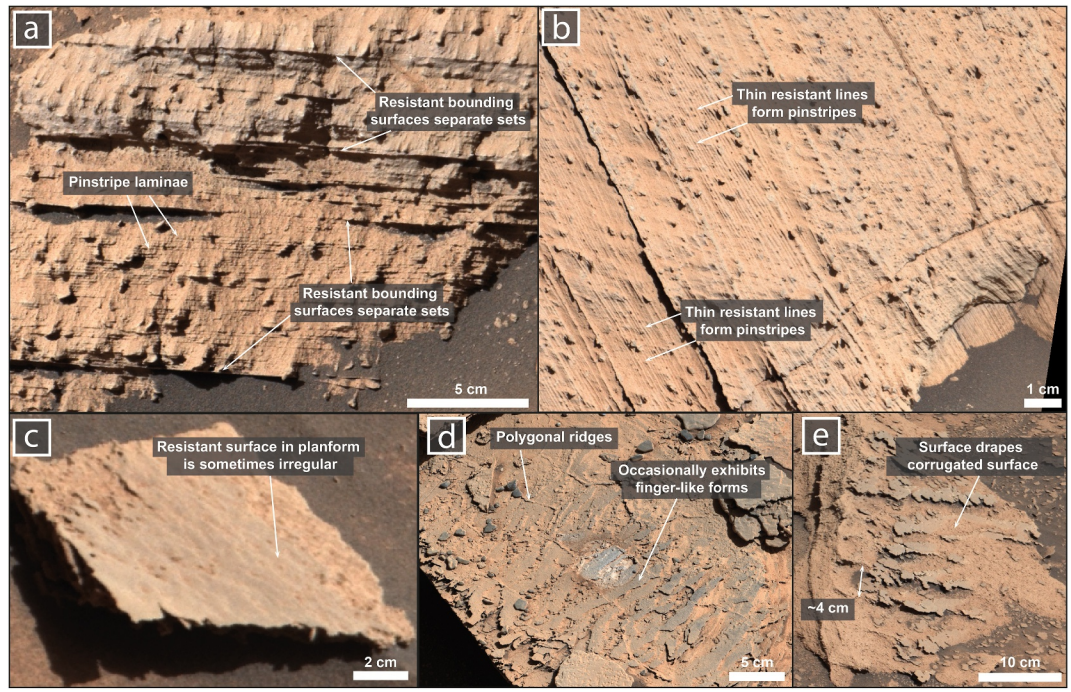

Figure 20. Examples of select facies characteristic of unit J as encountered across the traverse. (a) Mastcam mosaic of the light-toned, planar, laterally extensive laminae separated by resistant bounding surfaces. (Mastcam mosaic MR_mcam104278 acquired on Sol 3867, at Sol 3865 end-of-drive location.) (b) Mastcam mosaic showing the pinstripe pattern of the light-toned laminae. (Mastcam mosaic MR_mcam104420 acquired on Sol 3892.) (c–e) Mastcam mosaics showing planform views of the various textures exhibited by the resistant bounding surfaces. (c) Surface with a gently irregular and undulating topography on the mm to cm-scale (mastcam mosaic MR_mcam104328 acquired on Sol 3876, at Sol 3873 end-of-drive location.) (d) Surface comprised of parallel ridges with a dendritic pattern. Note the overlying light-toned polygonal ridges. (Mastcam mosaic MR_mcam104461 acquired on Sol 3898, at Sol 3897 end-of-drive location.) (e) Surface comprised of u-shaped grooves truncating light-toned laminae and draped by the dark-toned resistant surface. (Mastcam mosaic MR_mcam104403 acquired on Sol 3889, at Sol 3887 end-of-drive location.) Image credits: NASA/JPL-Caltech/MSSS.

Nielson, 1986). The polygonal ridges of light-toned material over the dark-toned indurated laminae (Figure 20d) appear similar to other polygonal patterns identified in the clay-sulfate transition attributed to either desiccation (Rapin et al., 2023a) or diagenesis post-dating lithification (Seeger & Grotzinger, 2024).

Unit J also shows meter-scale cross-bedding which may represent migration of small isolated dunes common in some sandsheet environments (Kocurek & Nielson, 1986). The large, ∼63-m-wide scour that truncates unit J resembles the scours identified truncating the strata within unit H and we similarly interpret that these represent localized deflation from paleo-blowouts.

4.4.7. Unit K

4.4.7.1. Architectural Elements

Unit K, ∼12.9 m thick, outcrops as a light-toned slope-forming stratigraphic interval with uniform planar stratification (Figure 21). Unit K marks the top of the stratigraphic succession observed in Orinoco and Chenapau, draping across a sharp planar contact with the underlying unit J and associated scour (Figure 20a).

Across the traverse, unit K outcrops as light-toned, rounded, smooth blocks similar to units G and I. The lithofacies are also similar, characterized by light-toned, laterally extensive, planar, even-in-thickness laminae. While poor outcrop exposure prevented more detailed measurements of these laminae, they were consistently ∼1 mm where measured (Figure S9 in Supporting Information S1) and appeared homogenous. Similar mm-scale nodules were also observed here.

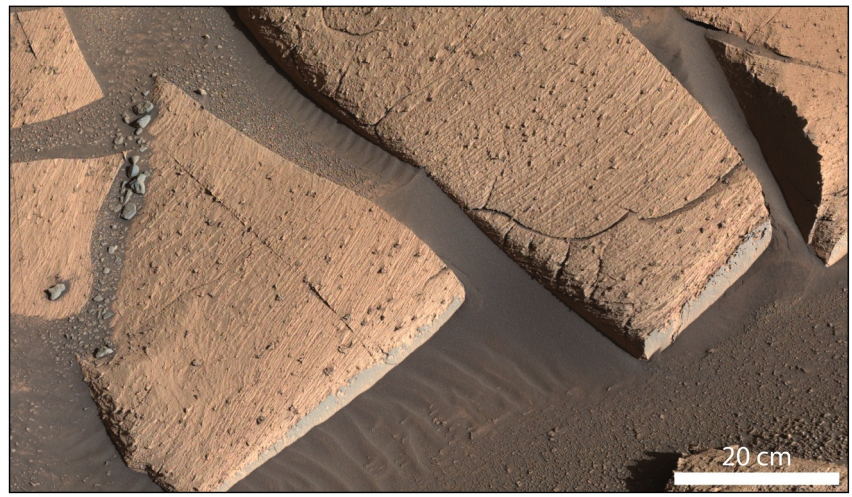

Figure 21. Example of unit K lithofacies as encountered across the traverse. (Mastcam mosaic MR_mcam104581 acquired on Sol 3914, at Sol 3912 end-of-drive location.) Image credits: NASA/JPL-Caltech/MSSS.

4.4.7.2. Interpretations

The planar-parallel, homogenous laminae lithofacies observed in unit K are similar to the lithofacies observed in units B, G, and I (Sections 4.2, 4.4.3, and 4.4.5) and represent aeolian deposition in an aeolian sandsheet environment. The uniformity of the laminae reflects steady winds and near-constant deposition rates.

5. Discussion

5.1. What Was the Paleoenvironmental Setting?

Combined sedimentary facies and architectural-element analysis indicate that the layered sulfate-bearing strata are formed using depositional processes influenced by both wind and water. Here, we discuss the possible depositional processes responsible for forming the ~100-m-thick succession exposed within Marker Band valley, arguing for a predominantly aeolian depositional model influenced by near surface water.

5.1.1. Establishing an Aeolian Paleoenvironment

The tabular, meter-scale cross-bedding with asymptotic bases (Figure 5) identified in the Contigo member (i.e., unit A) appears similar to cross-bedding formed by migrating simple dunes. Both fluvial and aeolian dunes can exhibit meter-scale low-angle cross-bedding with asymptotic bases (Collinson & Mountney, 2019). However, several architectural features along with other contextual facies observations lead us to prefer an aeolian depositional interpretation. The broad, sweeping, asymptotic downlapping relationships of the cross-sets onto the underlying bounding surfaces (Figure 5; Section 4.1) are characteristic of dune apron accumulation from reversing winds, wind-flow detachment, or sand suspension over dune crests (Brookfield, 1977; Clemmensen, 1988; Kocurek & Dott, 1981; Kocurek et al., 2007; Walker & Middleton, 1977). There is also a notable absence of other fluvial architectures such as downcutting erosional surfaces expected from fluvial cross-beds or paleochannel forms.

One of the more compelling features supporting an aeolian origin for the Contigo member is the prevalence of pinstripe laminae (Section 4.1). These laminae are planar, laterally extensive, and exhibit thin, dark-toned (Figure 17a) or indurated (Figures 9d and 18d) lines closely resembling a pinstripe pattern. Pinstripe laminae are a phenomenon directly attributed to inverse grading in wind ripples (Fryberger & Schenk, 1988; Mountney, 2006a). In wind-ripple deposition, fine particles accumulate in ripple troughs, shielded by coarser grains during ripple migration, producing distinctive thin lines that create this diagnostic pinstripe pattern preserved in the rock record (Fryberger & Schenk, 1988; Mountney, 2006a). Finer particles can retain moisture, undergoing preferential early cementation leading to the pinstripes becoming indurated (Fryberger & Schenk, 1988). While inverse grading is difficult to confirm on Mars as finer particles are smaller than image resolution limits

(e.g., Banham et al., 2022; Stack et al., 2019), we can use the pinstripe pattern to infer the presence of laminations produced by aeolian wind ripples (Roberts et al., 2025), supporting an aeolian interpretation for unit A.

The planar bedded lithofacies identified in the Catrimani and Chenapau members have shared lithofacies, indicative of the operation of broadly similar sedimentary processes. A number of depositional processes can form planar bedding comprised of the thin planar laminae—observed in the Catrimani and Chenapau members—including suspension settling through a water column, suspension settling of dust or ash through the atmosphere, and finally aeolian traction deposition (e.g., Anderson & Dean, 1988; Fryberger & Schenk, 1988; Hunter, 1977; Pécsi, 1990; Smiley, 1955). Suspension settling through a water column can deposit thin, laterally continuous laminae (e.g., Anderson & Dean, 1988; Smiley, 1955), considered for the Catrimani and Chenapau members by Schieber et al. (2025). However, we find that the Catrimani and Chenapau planar-bedded lithofacies appear distinct from the characteristic periodic bundling of planar laminae observed in the Amapari member (Section 4.3.1; Figure 11e), which more closely resemble classic lacustrine couplets from suspension settling (e.g., Anderson & Dean, 1988; Smiley, 1955). Moreover, low-angle truncations are common within the planar-bedded lithofacies, a geometry, that is, awkward to reconcile with suspension settling in a low-energy aqueous environment and instead supports repeated reworking by traction or migrating bedforms. Suspension settling through the atmosphere can also lead to planar bedding comprised of thin, laterally continuous laminae; however, this interpretation is less likely due to the absence of massive bedding which is typically observed in such deposits (e.g., Pécsi, 1990). Instead, the facies association of the Catrimani member with the underlying dune cross-stratification (Section 4.2.1), along with the diagnostic sedimentary textures as discussed in more detail below, favor deposition in an aeolian sandsheet environment dominated by aeolian traction processes. These lithofacies can be subdivided into light-toned (Catrimani member: unit B, and the Chenapau member: units G, I, and K) and dark-toned, planar bedded lithofacies (Chenapau member: units H and J).

The light-toned, planar-bedded units contain highly uniform, planar-parallel laminae. This uniformity is often a diagnostic of subcritically climbing translatent strata, formed by the migration of wind-ripples (Chakraborty & Chakraborty, 2001; Fryberger et al., 1979; Fryberger & Schenk, 1988; Hunter, 1977; Kocurek & Dott, 1981; Kocurek & Nielson, 1986). Their arrangement into broadly planar-bedded sets implies accumulation over a planar surface, consistent with an aeolian sandsheet environment (e.g., Kocurek & Nielson, 1986). The uniform thickness of laminae may reflect both the regular spacing of wind ripples in a given area at one time (Hunter, 1977; Trewin, 1993)--as observed on Mars (Durán et al., 2014)--and steady winds with near-constant deposition rates (Hunter, 1977; Trewin, 1993). While some units exhibit clear evidence of a pinstripe pattern from inverse grading of the migrating wind-ripples (units G; I; Figures 15d and 18d), pinstripe laminae are not as easily recognized in these lithofacies due to either poor outcrop exposure, different fluid-retention properties (Fryberger & Schenk, 1988), or a uniform grain size (Collinson & Mountney, 2019). Alternatively, some laminae could reflect aeolian planebed lamination, which forms under high wind velocities on flat, smooth surfaces (Clemmensen & Abrahamsen, 1983; Hunter, 1977; Kocurek & Dott, 1981; Ventra et al., 2017).

The dark-toned, planar-bedded lithofacies contain a variety of sedimentary textures that support aeolian deposition. The multiple occurrences of pinstripe laminae (Figures 17b and 20b; Sections 4.4.4 and 4.4.6) support continued aeolian sand-sheet deposition. Broad, u-shaped scours truncate the dark-toned planar-bedded lithofacies and are interpreted to represent erosion by intense, localized wind deflation (e.g., Roberts et al., 2025). There is also evidence that these lithofacies may contain occurrences of a damp aeolian sandsheet environment. Unit H contains potential adhesion ripples (Figure 17)—which form when sediment sticks to a slightly damp surface (Section 4.4.4; e.g., Goodall et al., 2000; Hunter, 1973; Kocurek & Fielder, 1982)—and needle/diamond shaped features resembling euhedral sulfate crystals (Mees et al., 2012)—suggesting syndepositional evaporite crystals that were either reworked or formed near the surface (Cohen et al., 2022; Kah et al., 2018; Kocurek & Nielson, 1986; Schieber et al., 2022).

5.1.2. Evidence for Episodic Surface Water

Mondro, Grotzinger, et al. (2025) identified symmetric ripples in the Amapari member and interpreted these ripples to have formed under oscillatory wave action in a shallow lake environment (see Section 4.3.1). The transition into repeated bundles of planar laminae in the uppermost section of this member (see Section 4.3.1) may also indicate that the lake became deeper over time (Gupta et al., 2023a, 2023b; Lewis et al., 2023; Mondro, Grotzinger, et al., 2025). As wind deflation can erode substantial lacustrine deposits (Clemmensen &

Tirsgaard, 1990; Kocurek, 1988), the abrupt transition into aeolian sandsheets in the Chenapau member after the Amapari member is therefore inferred to have occurred after some amount of wind deflation, indicating that the preserved ∼1 m thick unit is only a small portion of the original lacustrine deposits.

Further evidence for surface water is identified in the dark-toned lens embedded within unit E of the Chenapau member. Lithofacies comprised of cm-scale cross-bedding and a wing-shaped architectural feature are characteristic of fluvial dunes in a shallow stream (Roberts et al., 2025). This fluvial lens signifies that surface water was also periodically present during the accumulation of the aeolian sand-sheets in the Chenapau member.

5.1.3. What Were the Controls on Deposition and What Caused the Thick Succession of Sandsheets?

The planar bedded lithofacies represent an aeolian sandsheet deposit approximately 60 m thick—substantially thicker than typical sandsheets on Earth, which rarely exceed ∼20 m (Mountney, 2006a), with the thickest known succession reaching ∼50 m thick (Murton et al., 2025; Simplicio & Basilici, 2015). Accumulation and preservation of such an unusually thick deposit of sandsheets requires a sustained combination of conditions. First, net sediment input into the system must have occurred (Kocurek & Havholm, 1993a). Second, some mechanism must have limited the amount of loose sediment available, suppressing the ability of dunes to form (Kocurek & Nielson, 1986; Simplicio & Basilici, 2015). Third, the deposit must have been protected from erosion and reworking at the surface to allow for continued vertical aggradation (Kocurek & Havholm, 1993a). These conditions could have been satisfied by a number of factors including a rising water table, periodic flooding, surface cementation, coarse grain sizes, or ice (Basilici & Dal'Bó, 2010; Bristow et al., 2010; Chakraborty & Chakraborty, 2001; Clemmensen & Dam, 1993; Lea & Waythomas, 1990; Simplicio & Basilici, 2015).

Water played a significant role in both the accumulation and preservation of the aeolian sandsheets. Evidence for periodic surface water—in the form of the Amapari member (Gupta, Dietrich, Lewis, Kite, et al., 2023; Mondro, Grotzinger, et al., 2025) and the ephemeral stream in unit E—suggests that deposition occurred at or close to the water table (e.g., Mountney & Russell, 2009). In aeolian sandsheets, a high water table promotes a flat depositional surface ideal for the accumulation of highly planar and parallel wind-ripple laminae (Kocurek & Nielson, 1986), closely resembling those in the planar-bedded lithofacies of the Catrimani and Chenapau members. Potential adhesion ripples in unit H further suggest that the water table or its capillary fringe intersected the Martian surface, dampening the sediment enough for the adhesion of sediments in transport (Clemmensen et al., 1989; Goodall et al., 2000; Grotzinger et al., 2005; Jones et al., 2016). Since damp sand has a much higher threshold velocity for entrainment due to capillary tension, a high or rising water table is an effective mechanism that can continuously limit the quantity of entrained sand, suppressing dune formation and promoting sand sheet accretion (Kocurek & Nielson, 1986). Lenticular crystal formation in unit H may also indicate syndepositional sulfate precipitation at or near the surface (Cohen et al., 2022; Kah et al., 2018; Kocurek & Nielson, 1986; Schieber et al., 2022), potentially acting as a cement and further increasing the threshold velocity required for sediment mobilization.

5.1.4. What Caused the Dark- and Light-Toned Appearing Stratigraphic Intervals?

The vertical variations between the dark-toned planar bedded lithofacies and the light-toned planar bedded lithofacies may be governed by variations in water table rise, surface cementation, wind energy, and the depositional rate. Fryberger et al. (1979) and Schwan (1988) showed that lithofacies from aeolian sandsheets deposited under steady wind regimes and a consistent sand supply can differ from those deposited under more variable conditions (also see Kocurek, 1981). The light-toned, planar bedded lithofacies of the Catrimani and Chenapau members are texturally homogenous, consisting of planar-parallel, uniform laminae with rare truncations, consistent with deposition under continuous wind conditions with readily available sand (Hunter, 1977; Trewin, 1993). Comparable terrestrial accumulations have been hypothesized to reach vertical thicknesses similar to unit I from a single storm event (Fryberger et al., 1979; Lea & Waythomas, 1990; Schwan, 1988). Deposition under these conditions would have required a continuously rising water table to account for their accumulation (Basilici et al., 2021; Havholm & Kocurek, 1994; Kifumbi et al., 2022; Mountney, 2006b; Mountney & Jagger, 2004), but the rate of deposition would have been sufficiently high enough that the water table never intersected the surface to cause wet or damp surface conditions during the formation of the light-toned, planar-bedded units but not long enough to mobilize sediment into larger bedforms.

The dark-toned, planar bedded units, however, appear more texturally heterogeneous and record abundant truncation surfaces, which could perhaps be attributed to more varying wind conditions and less available sand (Fryberger et al., 1979; Kocurek, 1981; Lea & Waythomas, 1990; Mountney, 2006b; Schwan, 1988). As the dark-toned planar bedded lithofacies contain evidence for potential adhesion ripples and potential syndepositional sulfate precipitation, and because surface water—in the form of the lacustrine Amapari member and the fluvial lens in unit E—previously existed in this sedimentary succession, it is likely that episodic rises in surface water and surface cementation reduced the availability of loose sediment, leading to sediment bypass or even erosion producing a large number of bounding surfaces (e.g., Kocurek & Havholm, 1993a). Rare preservation of dune forms—as seen in unit J—is also not uncommon in this environment (Clemmensen & Abrahamsen, 1983). The resistant laminae interbedded between the light-toned wind-ripple sets appear analogous to "horizontal alternating beds" associated with alternating wet and dry conditions in modern and ancient sand sheet deposits, where fine sand from suspension adheres to a slightly damp truncation surface before being overlain by tractional wind-ripple sets (Lea & Waythomas, 1990; Murton et al., 2025). Alternate explanations such as deflation to the water table accompanied by brief deposition from surface ponding could also be responsible (Chakraborty & Chakraborty, 2001; Clemmensen & Abrahamsen, 1983). Regardless, early diagenesis would preferentially exploit the subtle textural differences between these wind-ripple sets—in a similar fashion to cementation of pinstripe laminae (e.g., Fryberger & Schenk, 1988), leading to induration of the resistant laminae. These resistant laminae were then made more pronounced through wind etching (Fryberger & Schenk, 1988; Murton et al., 2025) creating deep shadows and perhaps acting as traps to accumulate dark basaltic sand, leading to the dark-toned appearance from farfield images and orbit.

5.1.5. Do the Alternating Light-to Dark-Toned Planar Bedded Lithofacies Record Fluctuations in the Climate?

The repetitive transitions from light to dark-toned planar bedded lithofacies, aeolian scours, and back to light-toned planar bedded lithofacies may have arisen from more long-term changes in the balance between relative water-table level, surface cementation, wind energy, and sediment supply. These factors could have been impacted by changes in the regional climate (Figure 22; Mountney, 2012). A warmer, humid climate would lead to a rise in the water table and result in damp surface conditions. A more arid climate would lead to water table level fall and result in either dry surface conditions or deflation depending on the sedimentation rate. The gradational change from the light-toned to dark-toned lithofacies in Marker Band valley succession may suggest a gradually humidifying and warming climate to explain the decrease in sediment input relative to the rate of water table rise over time. The overlying broad aeolian scours which truncate the dark-toned planar bedded lithofacies could indicate a more arid climate and a fall in the relative water table, triggering intense erosion and the local deflation of partially cemented sandsheets into blowout structures (Roberts et al., 2025). A large increase in sediment availability, compared to the relative water table, would lead to sustained deposition of the dry sandsheets (Figure 22). This same gradational change from light-to dark-toned planar-bedded lithofacies followed by subsequent scouring was also noted in sandsheet deposits on Mars by Grotzinger et al. (2005) in Meridiani Planum and also attributed to a regional climate potentially influencing the relative water table level.

Alternatively, the coeval presence of blowouts, isolated dunes, and both dry and damp sandsheets in terrestrial desert environments (Mountney, 2006b) raises the possibility that the observed light and dark-toned planar bedded lithofacies could also be attributed to the impact of internal processes affecting the balance between wet and dry deposition and erosion over space rather than time (Figure 22; Mountney, 2012). Sediment transport and deposition depend on whether wind is over- or under-saturated with sediment (e.g., Kocurek, 1996). As wind moves across areas with sediment trapped by a high-water table or surface cementation, sediment mobilization thresholds are increased, potentially causing winds to become undersaturated. Then, as this wind encounters drier, or less-cemented zones, localized erosion may occur in the form of blowouts (Hesp, 2002; Smyth et al., 2019). Deflation and entrainment of sediment within the blowout could lead to a modest rise in sediment supply. The saturated wind—accompanied by flow deceleration over blowout rims (e.g., Smyth et al., 2019)—would lead to deposition and the accumulation of dry, aeolian sandsheets. In this hypothesis, co-existing dry to damp to erosional desert environments may have accumulated as this sand sea migrated, without needing a changing climate to explain vertical transitions. However, further work on integrated sandsheet and blowout fields is needed to assess how spatial heterogeneity in these systems can influence wind saturation and sediment transport.

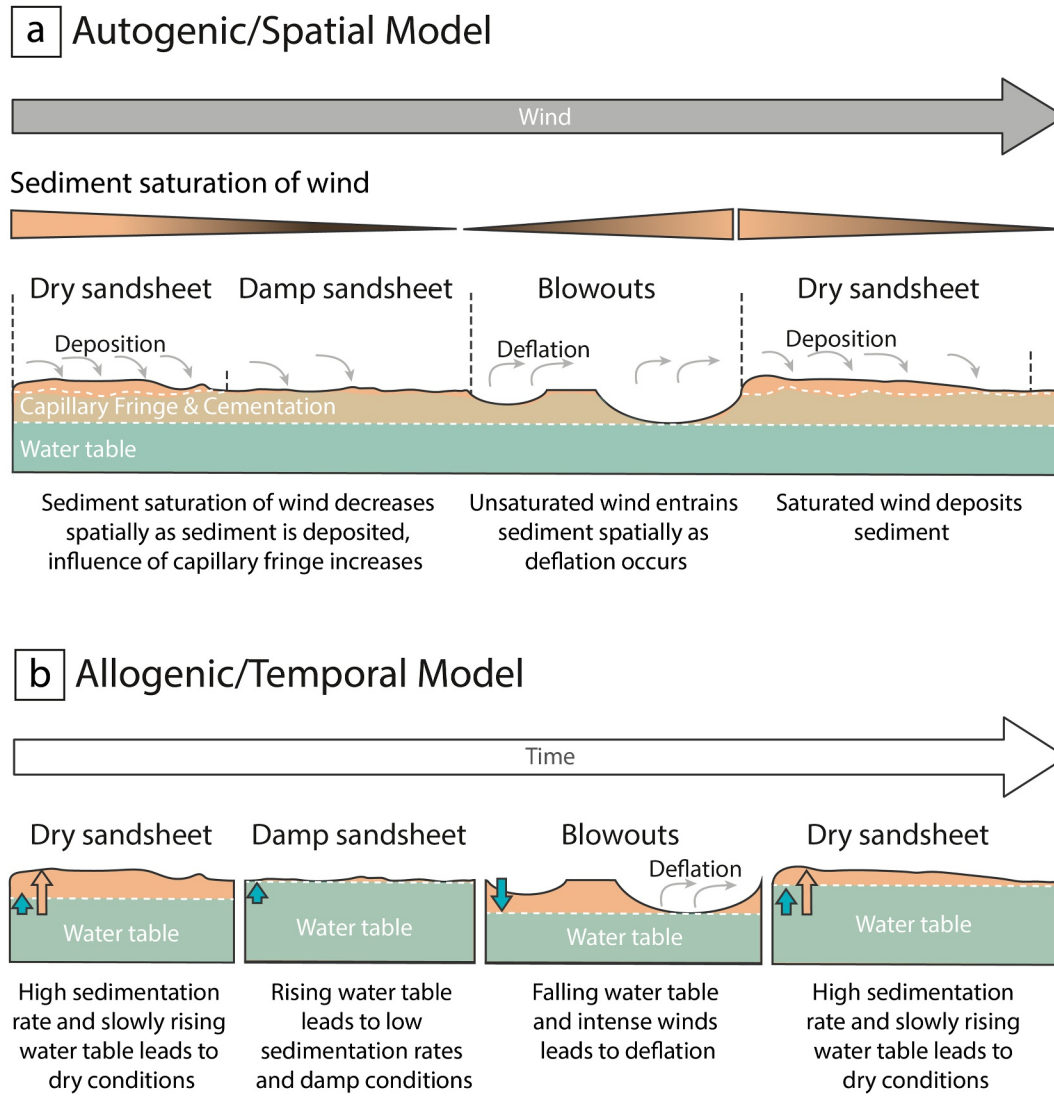

Figure 22. Proposed models showing how the occurrence of dry sandsheets, damp sandsheets, and aeolian deflation can occur through internal system dynamics or external factors. (a) Model showing the spatial complexity of co-existing environments in a sand sea impacting the sediment saturation of a given wind, which in turn impacts the depositional environment. (b) Alternate dynamic model showing how a climate-controlled relative water table height can impact depositional environments over time.

5.1.6. Stratigraphic Synthesis and a Record of a Changing Climate at the Base of the Layered Sulfates

We construct the following scenario as a possible sequence of events in the depositional history of the basal succession of the Layered Sulfate unit (Figure 23):

1. Deposition in the orbitally defined Layered Sulfate unit began with the accumulation of simple aeolian dunes migrating over a potential regionally extensive supersurface in the upper section of the Contigo member (see Section 5.1), indicative of a dry aeolian system with high sediment availability. Minimal influence of the water-table may have generated the flat accumulation surfaces (e.g., Kocurek & Day, 2018; Kocurek & Havholm, 1993b; Veiga et al., 2002).
2. A reduction in sedimentation rate relative to a gradual rise in the water table led to the inhibition of dune development and promoted the formation of laterally continuous sandsheets.
3. Further decline in sediment input resulted in a depositional hiatus, enabling deflation down to the capillary fringe of the water table and development of a regional deflationary supersurface (Mondro, Grotzinger,

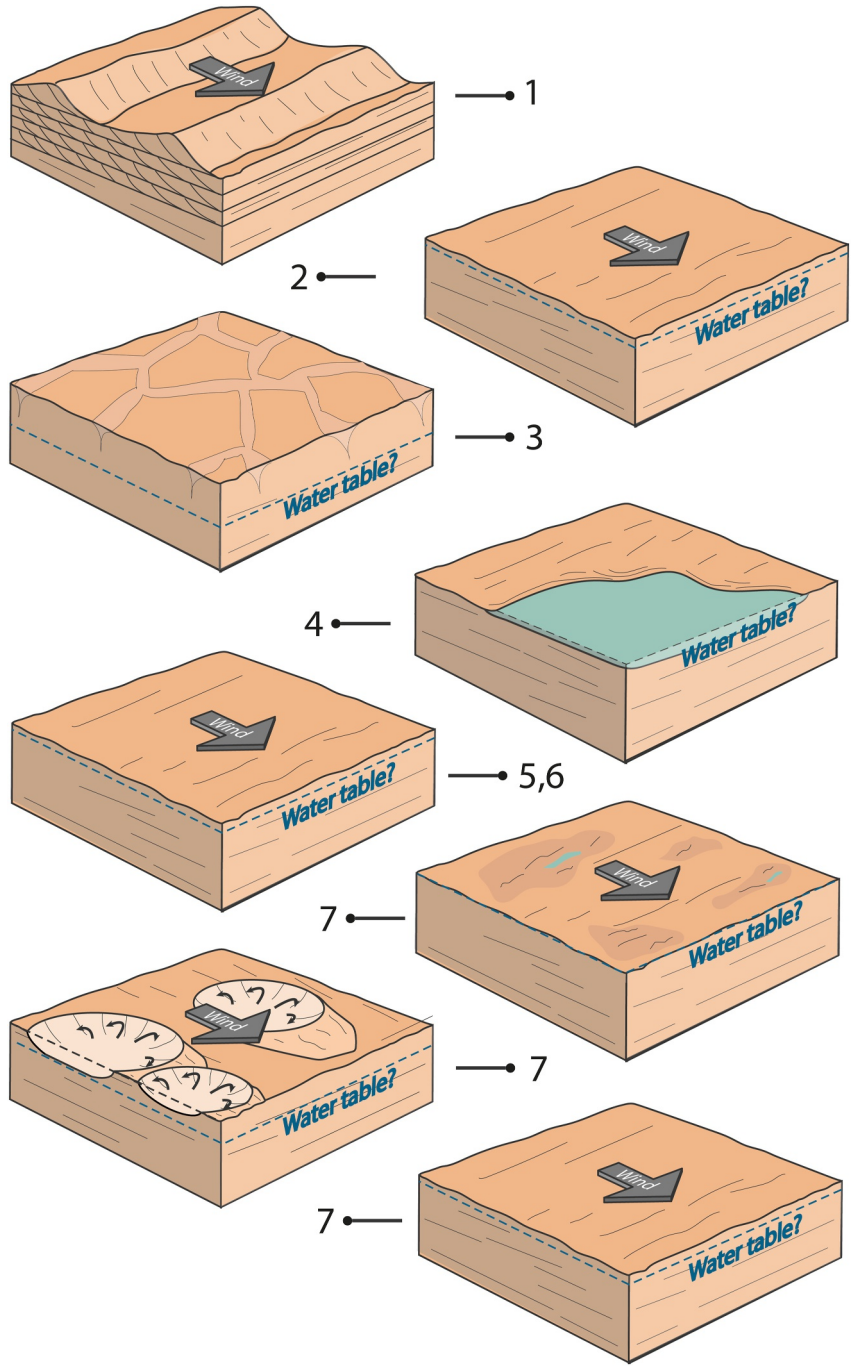

Figure 23. Dynamic model showing the stratigraphic synthesis and evolution of facies in Marker Band valley recorded in the Contigo (1), Catrimani (2–3), Amapari (4), and Chenapau (5–7) members as described in Section 5.1.6.

et al., 2025; Rapin et al., 2021). This surface was modified by surface alteration (Farrand et al., 2025; Thompson et al., 2024) and contraction-expansion features attributed to thermal contraction of partially cemented sand (e.g., Kocurek & Hunter, 1986; Simpson & Loope, 1985).

4. A modest rise in the water table facilitated the formation of a shallow, regionally extensive lake under ice-free conditions, leading to low-energy subaqueous sedimentation in the Amapari member (Mondro, Fedo, et al., 2025; Mondro, Grotzinger, et al., 2025).

5. Subsequent lake-level fall exposed the subaqueous deposits to aeolian activity. Undersaturated winds reworked or removed these fine-grained lacustrine sediments (e.g., Clemmensen & Tirsgaard, 1990), leading to inferred deflation prior to the accumulation of the Chenapau member.
6. A rise in sediment flux reinitiated subaerial deposition. Surface water was still present as localized runoff in small, fluvial streams, as seen by the lens in unit E of the Chenapau member.
7. A net rise in the water table—at the same pace as sediment deposition—led to the accumulation of the thick succession of sandsheets. Short-term climatic variability or autogenic processes drove repeated transitions between damp sandsheet formation, localized deflation, and dry sandsheet accumulation. These cycles reflect fluctuations in the balance between the water table, sedimentation rate, and wind strength.

5.2. Implications

The orbital-scale transition from clay-bearing strata to a mixed clay- and sulfate-bearing unit, and thence to the layered sulfate-bearing unit within the stratigraphy of Aeolis Mons (e.g., Fraeman et al., 2016; Sheppard et al., 2021), has been widely interpreted as a record of a progressive aridification of Gale crater (e.g., Milliken et al., 2010) during the Hesperian, 200–500 Myr after the Gale crater formed (Grant et al., 2014; Grotzinger et al., 2015; Thomson et al., 2011). Similarly, the transition from lacustrine (Grotzinger et al., 2014, 2015) to shoreline (Gwizd et al., 2024) environments recorded in clay-bearing strata, and finally to aeolian dune environments punctuated by brief episodes of flooding (Edgar et al., 2024; Gupta, Dietrich, Lewis, Kite, et al., 2023) recorded in the mixed clay- and sulfate-bearing unit, implies a climatic shift from wetter to drier conditions. However, our depositional model for the layered sulfates challenges this monotonic aridification trend.

The transition from aeolian simple dunes to aeolian sandsheets indicates that, rather than a simple decline in the water table due to continuous evaporation, conditions involved an overall *rise* in the water table relative to the depositional surface (e.g., Kocurek & Havholm, 1993a; Mountney & Thompson, 2002). On Earth, a relative rise in water table results from subsidence of the sediment column through a fixed water table or an absolute increase in groundwater level (Mountney, 2006a). As Gale crater lacks a mechanism for sustained tectonic subsidence (Grotzinger et al., 2015), the most likely scenario for aeolian sandsheet accumulation and preservation is an absolute—but slowly and maybe intermittently—increase in groundwater level that kept pace with the accumulation of the aeolian sandsheets.

Another possible implication our depositional model has for the regional paleoclimate is that this water table rise might have been intermittent. The multiple examples of wet, damp, and dry deposition, and aeolian deflation in the basal section of the LSu could be explained by periods of relative water table rise and fall compared to the accumulation surface (Section 5.1.5). These periods of apparent relative water table level rise and fall may reflect temporal complexities in the regional water table level, potentially impacted by seasonal melting (e.g., Kite, Halevy, et al., 2013), However, these periods of apparent relative water table rise and fall could also be explained by spatial complexities in the sand-sheet system leading to changing accommodation space and internal wind dynamics affecting the local depositional environment without the need for regional fluctuations in the paleoclimate (Section 5.1.5).

Geomorphic evidence and modeling indicate that Gale once had a larger groundwater system extending across northern Aeolis (Putnam & Palucis, 2021). The depth at which the Marker Band valley succession accumulated—several kilometres below the regional topography—suggests depositional environments with near-surface groundwater may have been restricted to topographic lows, with most of the surrounding terrain arid. However, these topographic lows—with persistent ground water and intermittent surface water—may have acted as localized, sustained habitable niches.

6. Conclusions

This study provides a detailed stratigraphic analysis of the ∼100 m thick sedimentary succession of the lower layered sulfate-bearing unit comprising the Contigo, Catrimani, Amapari, and Chenapau members of the Mirador formation. The succession is predominantly deposited by aeolian processes dominated by meter-scale tabular cross-bedding in the Contigo member interpreted as aeolian dunes and a light- and dark-toned planar-bedded lithofacies in the Catrimani and Chenapau members predominantly comprised of pinstripe laminae interpreted as aeolian sandsheets. A high-water table would have promoted a flat depositional surface ideal for the accumulation of highly planar and parallel wind-ripple laminae. Evidence for episodic surface water,

including the lacustrine environment recorded in the Amapari member and a small fluvial lens embedded in the Chenapau member further support a high-water table during the accumulation of the lower layered sulfates. Variations between the light- and dark-toned planar-bedded lithofacies in the Chenapau member reflect differences in sediment availability, moisture content, wind energy, and depositional rate. Darker units are interpreted to record wetter conditions with intermittent deposition and potential adhesion structures, while lighter units reflect drier and more continuous aeolian deposition. The ∼60 m thickness of aeolian sandsheets far exceeds typical terrestrial analogs. This thickness likely resulted from a slowly rising water table that limited sediment mobilization. Rather than a steady drying trend, the Layered Sulfate unit of the Gale crater records intervals of rising water table and persistent subsurface water at the time of deposition. While surface conditions were still overall drier than during deposition of the clay-bearing stratigraphy, the persistence of groundwater suggests that habitable niches may have endured longer than a straightforward aridification model would imply.

Conflict of Interest

The authors declare no conflicts of interest relevant to this study.

Availability Statement

The HiRISE mosaic used in this research is available through Calef and Parker (2016; https://astrogeology.usgs.gov/search/map/mars_msl_gale_merged_orthophoto_mosaic_25cm). Additional data from HiRISE (McEwen et al., 2007; https://doi.org/10.1029/2005JE002605) and CTX (Malin et al., 2017; https://doi.org/10.1029/2006JE002808) images can be accessed at the NASA Planetary Data System Geosciences Node (https://pds-geosciences.wustl.edu/missions/mro/default.htm). All Mastcam (Malin et al., 2017; https://doi.org/10.1002/2016EA000252) and MAHLI (Edgett et al., 2012; https://doi.org/10.1007/s11214-012-9910-4) images referenced in this manuscript can be found at the NASA Planetary Data System Cartography and Imaging Sciences Node (https://pds-imaging.jpl.nasa.gov/volumes/msl.html).

Acknowledgments

We would like to thank the efforts made by the NASA Mars Science Laboratory (MSL) Project's engineering, science, and management teams in making this research possible. We are also grateful to the many MSL team members who participated in tactical and strategic operations during the traverse up to and through Marker Band valley. Special thanks go to Malin Space Science Systems for providing operation support to acquire these images and to Mike Malin for the processing of Mastcam mosaic products used herein. This work was supported by the Science and Technology Facilities Council (STFC), ST/W507520/1 (A. Roberts); ST/X002373/1, ST/S001492/1 (S. Gupta); the U.K. Space Agency, ST/Y000137/1, ST/S001506/1 (S.G. Banham); and ST/W002566/2 (J. Davis); and by the National Aeronautics and Space Administration (NASA), NNH22OB34A (L. Edgar), 80NSSC22K0731 (E. Kite), 80NSSC22K0779 (J. R. Johnson). VRVis are acknowledged for the ongoing support and development of the PRo3D software. Joanneum Research are acknowledged for processing of key data products which made this research possible. VRVis and JOANNEUM RESEARCH activities were funded by FFG ASAP Contract 911911. The data presented in this research are archived with the NASA Planetary Data System (pds.nasa.gov) and can be accessed through the MSL Curiosity Analyst's Notebook (https://an.rsl.wustl.edu/msl). Parts of this research were conducted at the Jet Propulsion Laboratory, California Institute of Technology, under a contract with the National Aeronautics and Space Administration (80NM0018D0004).

References

Ahlbrandt, T. S., & Fryberger, S. G. (1981). Sedimentary features and significance of interdune deposits.

Ahmad, N. (1996). Occurrence and distribution of Vertisols. In *Developments in soil science* (Vol. 24, pp. 1–41). Elsevier. https://doi.org/10.1016/s0166-2481(96)80003-1

Alexander, D. A., Deen, R. G., Andres, P. M., Zamani, P., Mortensen, H. B., Chen, A. C., et al. (2006). Processing of Mars Exploration Rover imagery for science and operations planning. *Journal of Geophysical Research*, *111*(E2). https://doi.org/10.1029/2005je002462

Anderson, R., & Bell, J. III. (2010). Geologic mapping and characterization of Gale crater and implications for its potential as a Mars Science Laboratory landing site. *Mars J*, *5*, 76–128.

Anderson, R. S. (1990). Eolian ripples as examples of self-organization in geomorphological systems. *Earth-Science Reviews*, *29*(1–4), 77–96. https://doi.org/10.1016/0012-8252(0)90029-u

Anderson, R. Y., & Dean, W. E. (1988). Lacustrine varve formation through time. *Palaeogeography, Palaeoclimatology, Palaeoecology*, *62*(1–4), 215–235. https://doi.org/10.1016/0031-0182(88)90055-7

Anderson, W., & Day, M. (2017). Turbulent flow over craters on Mars: Vorticity dynamics reveal aeolian excavation mechanism. *Physical Review E*, *96*(4), 043110. https://doi.org/10.1103/physreve.96.043110

Banham, S., Gupta, S., Roberts, A., Davis, J., Cowart, A., Schieber, J., et al. (2024a). Diagenesis is controlled by primary aeolian depositional processes in the Mirador formation (Gale crater, Mars). In *The 55th lunar and planetary science conference: The Woodlands, Texas*.

Banham, S., Roberts, A., Gupta, S., Davis, J., Thompson, C. K., Rubin, D., et al. (2024b). Ice? Salt? Pressure? Sediment deformation structures as evidence of late-stage shallow ground water in Gale crater, Mars. *Geology*, *52*(7), 492–496. https://doi.org/10.1130/G51849.1

Banham, S. G., Gupta, S., Rubin, D. M., Bedford, C. C., Edgar, L. A., Bryk, A. B., et al. (2022). Evidence for fluctuating wind in shaping an Ancient Martian Dune field: The Stimson formation at the Greenheugh pediment, Gale crater. *Journal of Geophysical Research: Planets*, *127*(9), e2021JE007023. https://doi.org/10.1029/2021je007023

Banham, S. G., Gupta, S., Rubin, D. M., Watkins, J. A., Sumner, D. Y., Edgett, K. S., et al. (2018). Ancient Martian aeolian processes and palaeomorphology reconstructed from the Stimson formation on the lower slope of Aeolis Mons, Gale crater, Mars. *Sedimentology*, *65*(4), 993–1042. https://doi.org/10.1111/sed.12469

Basilici, G., & Dal'Bó, P. F. F. (2010). Anatomy and controlling factors of a Late Cretaceous Aeolian sand sheet: The Marília and the Adamantina formations, NW Bauru Basin, Brazil. *Sedimentary Geology*, *226*(1–4), 71–93. https://doi.org/10.1016/j.sedgeo.2010.02.010

Basilici, G., & Dal'Bó, P. F. F. (2014). Influence of subaqueous processes on the construction and accumulation of an aeolian sand sheet. *Earth Surface Processes and Landforms*, *39*(8), 1014–1029. https://doi.org/10.1002/esp.3498

Basilici, G., Mesquita, Á. F., Soares, M. V. T., Janočko, J., Mountney, N. P., & Colombera, L. (2021). A Mesoproterozoic hybrid dry-wet aeolian system: Galho do Miguel formation, SE Brazil. *Precambrian Research*, *359*, 106216. https://doi.org/10.1016/j.precamres.2021.106216

Basma, A. A., AlHomoud, A. S., Malkawi, A. I. H., & AlBashabsheh, M. A. (1996). Swelling-shrinkage behavior of natural expansive clays. *Applied Clay Science*, *11*(2–4), 211–227. https://doi.org/10.1016/s0169-1317(96)00009-9

Bedford, C. C., Schwenzer, S. P., Bridges, J. C., Banham, S., Wiens, R. C., Gasnault, O., et al. (2020). Geochemical variation in the Stimson formation of Gale crater: Provenance, mineral sorting, and a comparison with modern Martian dunes. *Icarus*, *341*, 113622. https://doi.org/10.1016/j.icarus.2020.113622

Bell, J. F., Godber, A., McNair, S., Caplinger, M. A., Maki, J. N., Lemmon, M. T., et al. (2017). The Mars Science Laboratory rover Mastcam instruments: Preflight and in-flight calibration, validation, and data archiving. *Earth and Space Science*, *4*(7), 396–452. https://doi.org/10.1002/2016ea000219

Benison, K. C. (2019). The physical and chemical sedimentology of two high-altitude acid salars in Chile: Sedimentary processes in an extreme environment. *Journal of Sedimentary Research*, *89*(2), 147–167. https://doi.org/10.2110/jsr.2019.9

Besly, B., Romain, H. G., & Mountney, N. P. (2018). Reconstruction of linear dunes from ancient aeolian successions using subsurface data: Permian Auk formation, Central North Sea, UK. *Marine and Petroleum Geology*, *91*, 1–18. https://doi.org/10.1016/j.marpetgeo.2017.12.021

Bibring, J. P., Langevin, Y., Mustard, J. F., Poulet, F., Arvidson, R., Gendrin, A., et al. (2006). Global mineralogical and aqueous Mars history derived from OMEGA/Mars express data. *Science*, *312*(5772), 400–404. https://doi.org/10.1126/science.1122659

Bristow, C. S., Augustinus, P., Wallis, I., Jol, H., & Rhodes, E. (2010). Investigation of the age and migration of reversing dunes in Antarctica using GPR and OSL, with implications for GPR on Mars. *Earth and Planetary Science Letters*, *289*(1–2), 30–42. https://doi.org/10.1016/j.epsl.2009.10.026

Brookfield, M. E. (1977). Origin of bounding surfaces in Ancient aeolian sandstones. *Sedimentology*, *24*(3), 303–332. https://doi.org/10.1111/j.1365-3091.1977.tb00126.x

Calef, F., & Parker, T. (2016). *MSL Gale merged Orthophoto Mosaic: PDS annex*. U.S. Geological Survey.

Caravaca, G., Gupta, S., Rapin, W., Schieber, J., Le Deit, L., Mangold, N., et al. (2025). Prow & co.: Inside the fluvial lenses of Gale's layered sulfate unit. In *Proceedings 56th lunar and planetary science conference* (p. 1389).

Caravaca, G., Le Mouelic, S., Gupta, S., Mangold, N., Rapin, W., Schieber, J., et al. (2022). The Prow outcrop: An "open catalog" of multiscale 3D fluvial sedimentary structures in the lower sulfate unit of Gale crater (Mars). In *Proceedings europlanet science congress*.

Caravaca, G., Mangold, N., Dehouck, E., Schieber, J., Zaugg, L., Bryk, A. B., et al. (2022). From Lake to River: Documenting an environmental transition across the Jura/Knockfarril hill members boundary in the Glen Torridon Region of Gale crater (Mars). *Journal of Geophysical Research-Planets*, *127*(9), e2021JE007093. https://doi.org/10.1029/2021je007093

Cardenas, B. T., Grotzinger, J. P., Lamb, M. P., Lewis, K. W., Fedo, C. M., Bryk, A. B., et al. (2022). Barform deposits of the Carolyn Shoemaker formation, Gale crater, Mars. *Journal of Sedimentary Research*, *92*(12), 1071–1092. https://doi.org/10.2110/jsr.2022.032

Carr-Crabaugh, M., & Dunn, T. L. (1996). Reservoir heterogeneity as a function of accumulation and preservation dynamics, tensleep sandstone, bighorn and Wind River basins. In *AAPG Bulletin* (Vol. 79).

Chakraborty, T., & Chakraborty, C. (2001). Eolian-aqueous interactions in the development of a proterozoic sand sheet: Shikaoda formation, Hosangabad, India. *Journal of Sedimentary Research*, *71*(1), 107–117. https://doi.org/10.1306/031700710107

Chipera, S., Vaniman, D., Rampe, E., Bristow, T., Martínez, G., Tu, V., et al. (2023). Mineralogical investigation of mg-sulfate at the Canaima drill site, Gale crater, Mars. *Journal of Geophysical Research: Planets*, *128*(11), e2023JE008041. https://doi.org/10.1029/2023je008041

Clemmensen, L. B. (1988). Aeolian morphology preserved by lava cover, the Precambrian Mussartut member, Eriksfjord formation, South Greenland. *Bulletin of the Geological Society of Denmark*, *37*(1–2), 105–116. https://doi.org/10.37570/bgsd-1988-37-09

Clemmensen, L. B., & Abrahamsen, K. (1983). Aeolian stratification and facies association in desert sediments, Arran basin (Permian), Scotland. *Sedimentology*, *30*(3), 311–339. https://doi.org/10.1111/j.1365-3091.1983.tb00676.x

Clemmensen, L. B., & Dam, G. (1993). Aeolian sand-sheet deposits in the Lower Cambrian Nekso Sandstone formation, Bornholm, Denmark—Sedimentary architecture and genesis. *Sedimentary Geology*, *83*(1–2), 71–85. https://doi.org/10.1016/0037-0738(93)90183-6

Clemmensen, L. B., Olsen, H., & Blakey, R. C. (1989). Erg-margin deposits in the Lower Jurassic Moenave formation and Wingate Sandstone, southern Utah. *Geological Society of America Bulletin*, *101*(6), 759–773. https://doi.org/10.1130/0016-7606(1989)101<0759:emditl>2.3.co;2

Clemmensen, L. B., & Tirsgaard, H. (1990). Sand-drift surfaces: A neglected type of bounding surface: Geology. *Geology*, *18*(11), 1142–1145. https://doi.org/10.1130/0091-7613(1990)018<1142:sdsant>2.3.co;2

Cohen, T. J., Arnold, L. J., Gázquez, F., May, J.-H., Marx, S. K., Jankowski, N. R., et al. (2022). Late quaternary climate change in Australia's arid interior: Evidence from Kati Thanda–Lake Eyre. *Quaternary Science Reviews*, *292*, 107635. https://doi.org/10.1016/j.quascirev.2022.107635

Collinson, J., & Mountney, N. (2019). *Sedimentary structures*. Liverpool University Press.

Dal Bó, P. F. F., Basilici, G., & Angélica, R. S. (2010). Factors of paleosol formation in a Late Cretaceous eolian sand sheet paleoenvironment, Marilia formation. *Southeastern Brazil: Palaeogeography, Palaeoclimatology, Palaeoecology*, *292*(1–2), 349–365. https://doi.org/10.1016/j.palaeo.2010.04.021

Davis, J., Wilson, S., Williams, R. M. E., Dietrich, W., Thompson, L., Bryk, A., et al. (2025). In-Situ characterization of candidate debris flow deposits in Gediz Vallis Ridge, Gale crater, Mars. In *56th lunar and planetary science conference: The Woodlands, Texas*.

Day, M., & Kocurek, G. (2016). Observations of an aeolian landscape: From surface to orbit in Gale crater. *Icarus*, *280*, 37–71. https://doi.org/10.1016/j.icarus.2015.09.042

Dickson, J. L., Kerber, L. A., Fassett, C. I., & Ehlmann, B. L. (2018). A global, blended CTX mosaic of Mars with vectorized seam mapping: A new mosaicking pipeline using principles of non-destructive image editing. In *49th lunar and planetary science conference: The Woodlands, Texas*.

Dietrich, W. E., Bryk, A. B., Cowart, A., Fedo, C., Fau, A., Gasnault, O., et al. (2024). First contact with a rock avalanche deposit on Mars. In *Proceedings international conference on Mars, Pasadena (CA), United States* (Vol. 3007, p. 3101). Retrieved from https://hal.science/hal-04800331v1/file/3101.pdf, https://hal.science/hal-04800331v1/document https://hal.science/hal-04800331v1/file/3101.pdf, https://hal.science/hal-04800331v1/document, https://hal.science/hal-04800331v1/file/3101.pdf

Dromart, G., Le Deit, L., Rapin, W., Gasnault, O., Le Mouélic, S., Quantin-Nataf, C., et al. (2021). Deposition and erosion of a Light-Toned Yardang-forming unit of Mt Sharp, Gale crater, Mars. *Earth and Planetary Science Letters*, *554*, 116681. https://doi.org/10.1016/j.epsl.2020.116681

Durán, O., Claudin, P., & Andreotti, B. (2014). Direct numerical simulations of aeolian sand ripples. *Proceedings of the National Academy of Sciences*, *111*(44), 15665–15668. https://doi.org/10.1073/pnas.1413058111

Edgar, L., Grotzinger, J., Fedo, C. M., Meyer, M., Rapin, W., Dietrich, W. E., et al. (2024). Wet to dry depositional environments recorded in the clay-sulfate transition region in Gale crater, Mars: Overview and stratigraphic context for Curiosity's exploration campaign. In *55th lunar and planetary science conference: The Woodlands, Texas*.

Edgar, L. A., Fedo, C. M., Gupta, S., Banham, S. G., Fraeman, A. A., Grotzinger, J. P., et al. (2020). A lacustrine paleoenvironment recorded at Vera Rubin Ridge, Gale crater: Overview of the sedimentology and stratigraphy observed by the Mars science laboratory curiosity rover. *Journal of Geophysical Research-Planets*, *125*(3), e2019JE006307. https://doi.org/10.1029/2019je006307

Edgett, K. S., Caplinger, M. A., Maki, J. N., Ravine, M. A., Ghaemi, F. T., McNair, S., et al. (2015). Curiosity's robotic arm-mounted Mars Hand Lens Imager (MAHLI): Characterization and calibration status: Msl mahli technical report.

Edgett, K. S., & Sarkar, R. (2021). Recognition of sedimentary rock occurrences in satellite and aerial images of other worlds-insights from Mars. *Remote Sensing*, *13*(21), 4296. https://doi.org/10.3390/rs13214296

Edgett, K. S., Yingst, R. A., Ravine, M. A., Caplinger, M. A., Maki, J. N., Ghaemi, F. T., et al. (2012). Curiosity's Mars Hand Lens Imager (MAHLI) investigation. *Space Science Reviews*, *170*(1–4), 259–317. https://doi.org/10.1007/s11214-012-9910-4

Ehlmann, B. L., & Edwards, C. S. (2014). Mineralogy of the martian surface. *Annual Review of Earth and Planetary Sciences*, *42*(42), 291–315. https://doi.org/10.1146/annurev-earth-060313-055024

Fairén, A. G. (2010). A cold and wet Mars. *Icarus*, *208*(1), 165–175. https://doi.org/10.1016/j.icarus.2010.01.006

Farrand, W., Eng, A., Trussell, A., Johnson, J., Bell, J. III., Banham, S., et al. (2025). Multispectral properties of rocks in Marker Band Valley, and evidence for an alteration unit below the Amapari Marker Band at Gale crater, Mars. *Journal of Geophysical Research: Planets*, *130*(4), e2024JE008645. https://doi.org/10.1029/2024je008645

Fedo, C. M., Bryk, A. B., Edgar, L. A., Bennett, K. A., Fox, V. K., Dietrich, W. E., et al. (2022). Geology and stratigraphic correlation of the Murray and Carolyn shoemaker formations across the Glen Torridon Region, Gale crater, Mars. *Journal of Geophysical Research-Planets*, *127*(9), e2022JE007408. https://doi.org/10.1029/2022je007408

Ferronatto, J. P. F., Scherer, C. M. D., de Souza, E. G., dos Reis, A. D., & de Mello, R. G. (2019). Genetic units and facies architecture of a Lower Cretaceous fluvial-aeolian succession, Sao Sebastiao formation, Jatoba Basin, Brazil. *Journal of South American Earth Sciences*, *89*, 158–172. https://doi.org/10.1016/j.jsames.2018.11.009

Fischer, C., Dunkl, I., von Eynatten, H., Wijbrans, J. R., & Gaupp, R. (2012). Products and timing of diagenetic processes in upper Rotliegend sandstones from Bebertal (North German Basin, Parchim formation, Flechtingen High, Germany). *Geological Magazine*, *149*(5), 827–840. https://doi.org/10.1017/s0016756811001087

Fraeman, A. A., Ehlmann, B. L., Arvidson, R. E., Edwards, C. S., Grotzinger, J. P., Milliken, R. E., et al. (2016). The stratigraphy and evolution of lower Mount Sharp from spectral, morphological, and thermophysical orbital data sets. *Journal of Geophysical Research-Planets*, *121*(9), 1713–1736. https://doi.org/10.1002/2016je005095

Fryberger, S. G., Ahlbrandt, T. S., & Andrews, S. (1979). Origin, sedimentary features, and significance of low-angle eolian sand sheet deposits, great sand dunes National monument and vicinity, Colorado. *Journal of Sedimentary Petrology*, *49*(3), 733–746. https://doi.org/10.1306/212f782e-2b24-11d7-8648000102c1865d

Fryberger, S. G., & Schenk, C. J. (1988). Pin stripe lamination—A distinctive feature of modern and Ancient eolian sediments. *Sedimentary Geology*, *55*(1–2), 1–15. https://doi.org/10.1016/0037-0738(88)90087-5

Galanin, A. (2021). Late quaternary sand covers of Central Yakutia (Eastern Siberia): Structure, facies composition and paleo-environment significance: Kriosfera Zemli. *Earth's Cryosphere*, *25*(1), 3–34.

Gendrin, A., Mangold, N., Bibring, J.-P., Langevin, Y., Gondet, B., Poulet, F., et al. (2005). Sulfates in Martian layered terrains: The OMEGA/Mars Express view. *Science*, *307*(5715), 1587–1591. https://doi.org/10.1126/science.1109087

Golombek, M., Grant, J., Kipp, D., Vasavada, A., Kirk, R., Fergason, R., et al. (2012). Selection of the Mars science laboratory landing site. *Space Science Reviews*, *170*(1), 641–737. https://doi.org/10.1007/s11214-012-9916-y

Goodall, T. M., North, C. P., & Glennie, K. W. (2000). Surface and subsurface sedimentary structures produced by salt crusts. *Sedimentology*, *47*(1), 99–118. https://doi.org/10.1046/j.1365-3091.2000.00279.x

Grant, J. A., Wilson, S. A., Mangold, N., Calef, F., & Grotzinger, J. P. (2014). The timing of alluvial activity in Gale crater, Mars. *Geophysical Research Letters*, *41*(4), 1142–1148. https://doi.org/10.1002/2013gl058909

Grotzinger, J. P., Arvidson, R. E., Bell, J. F., Calvin, W., Clark, B. C., Fike, D. A., et al. (2005). Stratigraphy and sedimentology of a dry to wet eolian depositional system, Burns formation, Meridiani Planum, Mars. *Earth and Planetary Science Letters*, *240*(1), 11–72. https://doi.org/10.1016/j.epsl.2005.09.039

Grotzinger, J. P., Gupta, S., Malin, M. C., Rubin, D. M., Schieber, J., Siebach, K., et al. (2015). Deposition, exhumation, and paleoclimate of an ancient lake deposit, Gale crater, Mars. *Science*, *350*, 6257. https://doi.org/10.1126/science.aac7575

Grotzinger, J. P., Sumner, D. Y., Kah, L. C., Stack, K., Gupta, S., Edgar, L., et al. (2014). A habitable fluvio-lacustrine environment at Yellowknife Bay, Gale crater, Mars. *Science*, *343*, 6169. https://doi.org/10.1126/science.1242777

Gupta, S., Dietrich, W., Lewis, K., Mondro, C. A., Kite, E. S., Weitz, C. M., et al. (2023). Rippled to bits: Tales of transient Lakes in a Martian desert. AGU Fall Meeting 2023: San Francisco, CA.

Gupta, S., Dietrich, W. E., Lewis, K., Kite, E. S., Mondro, C. A., Schieber, J., et al. (2023). 'High' but not so dry on Aeolis Mons. In *54th lunar and planetary science conference: The Woodlands (Texas), United States*.

Gupta, S., Edgar, L., Yingst, R., Bryk, A., Caravaca, G., Dietrich, W., et al. (2022). Episodic aqueous conditions punctuated dominantly aeolian deposition within the layered sulphate-bearing unit, Gale crater (Mars). In *Proceedings europlanet Science Congress* (p. 963).

Gwizd, S., Fedo, C., Grotzinger, J., Banham, S., Rivera-Hernández, F., Gupta, S., et al. (2024). Evolution of a Lake Margin recorded in the Sutton Island member of the Murray formation, Gale crater, Mars. *Journal of Geophysical Research-Planets*, *129*(1), e2023JE007919. https://doi.org/10.1029/2023je007919

Gwizd, S., Fedo, C., Grotzinger, J., Banham, S., Rivera-Hernández, F., Stack, K. M., et al. (2022). Sedimentological and geochemical perspectives on a marginal lake environment recorded in the Hartmann's Valley and Karasburg members of the Murray formation, Gale crater, Mars. *Journal of Geophysical Research: Planets*, *127*(8), e2022JE007280. https://doi.org/10.1029/2022je007280

Harianto, T., Hayashi, S., Du, Y. J., & Suetsugu, D. (2008). Effects of fiber additives on the desiccation crack behavior of the compacted Akaboku soil as a material for landfill cover barrier. *Water Air and Soil Pollution*, *194*(1–4), 141–149. https://doi.org/10.1007/s11270-008-9703-2

Havholm, K. G., & Kocurek, G. (1994). Factors controlling aeolian sequence stratigraphy: Clues from super bounding surface features in the Middle Jurassic Page Sandstone. *Sedimentology*, *41*(5), 913–934. https://doi.org/10.1111/j.1365-3091.1994.tb01432.x

Heidsiek, M., Butscher, C., Blum, P., & Fischer, C. (2020). Small-scale diagenetic facies heterogeneity controls porosity and permeability pattern in reservoir sandstones. *Environmental Earth Sciences*, *79*(18), 425. https://doi.org/10.1007/s12665-020-09168-z

Hesp, P. (2002). Foredunes and blowouts: Initiation, geomorphology and dynamics. *Geomorphology*, *48*(1–3), 245–268. https://doi.org/10.1016/s0169-555x(02)00184-8

Hesp, P. A., & Hyde, R. (1996). Flow dynamics and geomorphology of a trough blowout. *Sedimentology*, *43*(3), 505–525. https://doi.org/10.1046/j.1365-3091.1996.d01-22.x

Hugenholtz, C. H., & Wolfe, S. A. (2006). Morphodynamics and climate controls of two aeolian blowouts on the northern Great Plains, Canada. *Earth Surface Processes and Landforms*, *31*(12), 1540–1557. https://doi.org/10.1002/esp.1367

Hugenholtz, C. H., & Wolfe, S. A. (2009). Form-flow interactions of an aeolian saucer blowout. *Earth Surface Processes and Landforms*, *34*(7), 919–928. https://doi.org/10.1002/esp.1776

Hunter, R. E. (1973). Pseudo-crosslamination formed by climbing adhesion ripples. *Journal of Sedimentary Research*, *43*(4).

Hunter, R. E. (1977). Basic types of stratification in small eolian dunes. *Sedimentology*, *24*(3), 361–387. https://doi.org/10.1111/j.1365-3091.1977.tb00128.x

Hurowitz, J. A., Grotzinger, J. P., Fischer, W. W., McLennan, S. M., Milliken, R. E., Stein, N., et al. (2017). Redox stratification of an ancient lake in Gale crater, Mars. *Science*, *356*(6341), eaah6849. https://doi.org/10.1126/science.aah6849

Jones, F. H., dos Santos Scherer, C. M., & Kuchle, J. (2016). Facies architecture and stratigraphic evolution of aeolian dune and interdune deposits, Permian Caldeirão Member (Santa Brígida formation). *Brazil: Sedimentary Geology*, *337*, 133–150. https://doi.org/10.1016/j.sedgeo.2016.03.018

Kah, L. C., Stack, K. M., Eigenbrode, J. L., Yingst, R. A., & Edgett, K. S. (2018). Syndepositional precipitation of calcium sulfate in Gale crater, Mars. *Terra Nova*, *30*(6), 431–439. https://doi.org/10.1111/ter.12359

Kifumbi, C., Scherer, C. M. D., de Souza, E. G., dos Reis, A. D., Ferronatto, J. P. F., & Michel, R. D. (2022). Late Pennsylvanian aridification in Gondwana mid-latitudes contemporaneous to high-latitudes ice cap expansion, upper Piaui formation. *Journal of South American Earth Sciences*, *117*, 103840. https://doi.org/10.1016/j.jsames.2022.103840

Kite, E. S., Halevy, I., Kahre, M. A., Wolff, M. J., & Manga, M. (2013). Seasonal melting and the formation of sedimentary rocks on Mars, with predictions for the Gale crater mound. *Icarus*, *223*(1), 181–210. https://doi.org/10.1016/j.icarus.2012.11.034

Kite, E. S., Lewis, K. W., Lamb, M. P., Newman, C. E., & Richardson, M. I. (2013). Growth and form of the mound in Gale crater, Mars: Slope wind enhanced erosion and transport: Geology. *Geology*, *41*(5), 543–546. https://doi.org/10.1130/g33909.1

Kocurek, G. (1981). Significance of interdune deposits and bounding surfaces in aeolian Dune sands. *Sedimentology*, *28*(6), 753–780. https://doi.org/10.1111/j.1365-3091.1981.tb01941.x

Kocurek, G. (1986). Origins of low-angle stratification in aeolian deposits. In W. G. Nickling (Ed.), *Aeolian geomorphology*.

Kocurek, G. (1988). 1st-Order and super bounding surfaces in Eolian Sequences—Bounding surfaces revisited. *Sedimentary Geology*, *56*(1–4), 193–206. https://doi.org/10.1016/0037-0738(88)90054-1

Kocurek, G. (1996). Desert aeolian systems. In H. G. Reading (Ed.), *Sedimentary environments: Processes, facies and stratigraphy* (pp. 125–153). Blackwell Science.

Kocurek, G. (1998). Aeolian system response to external forcing factors—A sequence stratigraphic view of the Saharan region. *Quaternary Deserts and Climatic Change*, 327–337.

Kocurek, G., Carr, M., Ewing, R., Havholm, K. G., Nagar, Y., & Singhvi, A. (2007). White Sands Dune Field, New Mexico: Age, dune dynamics and recent accumulations. *Sedimentary Geology*, *197*(3–4), 313–331. https://doi.org/10.1016/j.sedgeo.2006.10.006

Kocurek, G., & Day, M. (2018). What is preserved in the aeolian rock record? A Jurassic Entrada Sandstone case study at the Utah-Arizona border. *Sedimentology*, *65*(4), 1301–1321. https://doi.org/10.1111/sed.12422

Kocurek, G., & Dott, R. H. (1981). Distinctions and uses of stratification types in the interpretation of eolian sand. *Journal of Sedimentary Research*, *51*(2), 579–595.

Kocurek, G., & Fielder, G. (1982). Adhesion structures. *Journal of Sedimentary Research*, *52*(4), 1229–1241.

Kocurek, G., & Havholm, K. G. (1993a). Eolian sequence Stratigraphy--A conceptual framework: Chapter 16: Recent developments in siliciclastic sequence stratigraphy, siliciclastic sequence stratigraphy: Recent developments and applications (pp. 393–409).

Kocurek, G., & Havholm, K. G. (1993b). Eolian sequence stratigraphy – A conceptual framework: Chapter 16: Recent Developments in Siliciclastic Sequence Stratigraphy. In P. Weimer & H. W. Posamentier (Eds.), *Siliciclastic sequence stratigraphy: Recent developments and applications* (Vol. 52, pp. 393–403). Society of Economic Paleontologists and Mineralogists Special Publication.

Kocurek, G., & Hunter, R. E. (1986). Origin of polygonal fractures in sand, uppermost Navajo and page sandstones. *Journal of Sedimentary Petrology*, *56*, 895–904.

Kocurek, G., & Lancaster, N. (1999). Aeolian system sediment state: Theory and Mojave Desert Kelso dune field example. *Sedimentology*, *46*(3), 505–515. https://doi.org/10.1046/j.1365-3091.1999.00227.x

Kocurek, G., & Nielson, J. (1986). Conditions favorable for the formation of warm-climate aeolian sand sheets. *Sedimentology*, *33*(6), 795–816. https://doi.org/10.1111/j.1365-3091.1986.tb00983.x

Langford, R. P., & Chan, M. A. (1989). Fluvial-Aeolian Interactions 2. Ancient Systems. *Sedimentology*, *36*(6), 1037–1051. https://doi.org/10.1111/j.1365-3091.1989.tb01541.x

Langford, R. P., Pearson, K. M., Duncan, K. A., Tatum, D. M., Adams, L., & Depret, P. A. (2008). Eolian topography as a control on deposition incorporating lessons from modern dune seas: Permian Cedar Mesa Sandstone, SE Utah, USA. *Journal of Sedimentary Research*, *78*(5–6), 410–422. https://doi.org/10.2110/jsr.2008.045

Lea, P. D., & Waythomas, C. F. (1990). Late-Pleistocene eolian sand sheets in Alaska. *Quaternary Research*, *34*(3), 269–281. https://doi.org/10.1016/0033-5894(90)90040-r

Le Deit, L., Hauber, E., Fueten, F., Pondrelli, M., Rossi, A. P., & Jaumann, R. (2013). Sequence of infilling events in Gale crater, Mars: Results from morphology, stratigraphy, and mineralogy. *Journal of Geophysical Research-Planets*, *118*(12), 2439–2473. https://doi.org/10.1002/2012je004322

Le Mouelic, S., Gasnault, O., Herkenhoff, K., Bridges, N., Langevin, Y., Mangold, N., et al. (2015). The ChemCam Remote Micro-Imager at Gale crater: Review of the first year of operations on Mars. *Icarus*, *249*, 93–107. https://doi.org/10.1016/j.icarus.2014.05.030

Le Mouelic, S., Gasnault, O., Herkenhoff, K., Newsom, H., Gallegos, Z., Rapin, W., et al. (2019). Correction of stray light in CHEMCAM Remote Micro-Imager long distance images. *Lunar and Planetary Science Conference*.

Lewis, K. W., Kite, E. S., Weitz, C. M., Cowart, A., Dietrich, W. E., Gupta, S., et al. (2023). Rhythmic stratigraphy at the orbital marker bed at mount sharp, Gale crater, Mars. *54th lunar and planetary science conference 2023: The Woodlands, Texas*.

Loope, D. B., & Simpson, E. L. (1992). Significance of thin sets of Eolian cross-strata. *Journal of Sedimentary Petrology*, *62*(5), 849–859.

Maki, J. (2018). In N. P. D. System (Ed.), *MSL Mars Navigation Camera 5 RDR V2.0*.

Maki, J., Thiessen, D., Pourangi, A., Kobzeff, P., Litwin, T., Scherr, L., et al. (2012). The Mars science laboratory engineering cameras. *Space Science Reviews*, *170*(1–4), 77–93. https://doi.org/10.1007/s11214-012-9882-4

Malin, M. C., & Edgett, K. S. (2000). Sedimentary rocks of early Mars. *Science*, *290*(5498), 1927–1937. https://doi.org/10.1126/science.290.5498.1927

Malin, M. C., Ravine, M. A., Caplinger, M. A., Ghaemi, F. T., Schaffner, J. A., Maki, J. N., et al. (2017). The Mars Science Laboratory (MSL) Mast cameras and Descent imager: Investigation and instrument descriptions. *Earth and Space Science*, *4*(8), 506–539. https://doi.org/10.1002/2016ea000252

Maurice, S., Clegg, S., Wiens, R., Gasnault, O., Rapin, W., Forni, O., et al. (2016). ChemCam activities and discoveries during the nominal Mission of Mars science laboratory in Gale crater, Mars. *Journal of Analytical Atomic Spectrometry*, *31*.

McEwen, A. S., Eliason, E. M., Bergstrom, J. W., Bridges, N. T., Hansen, C. J., Delamere, W. A., et al. (2007). Mars reconnaissance orbiter's high resolution imaging science experiment (HiRISE). *Journal of Geophysical Research*, *112*, E5. https://doi.org/10.1029/2005je002605

McMahon, S., van Smeerdijk Hood, A., & McIlroy, D. (2017). The origin and occurrence of subaqueous sedimentary cracks. https://doi.org/10.1144/SP448.15

Mees, F., Casteneda, C., Herrero, J., & Van Ranst, E. (2012). The nature and significance of variations in gypsum crystal morphology in dry lake basins. *Journal of Sedimentary Research*, *82*(1), 37–52. https://doi.org/10.2110/jsr.2012.3

Mescolotti, P. C., Varejao, F. G., Warren, L. V., Ladeira, F. S. B., Giannini, P. C. F., & Assine, M. L. (2019). The sedimentary record of wet and dry eolian systems in the Cretaceous of Southeast Brazil: Stratigraphic and paleogeographic significance. *Brazilian Journal of Geology*, *49*(3), e20190057. https://doi.org/10.1590/2317-4889201920190057

Mesquita, A. F., Basilici, G., Soares, M. V. T., Janocko, J., Mountney, N. P., Colombera, L., & de Souza, C. R. (2021). Hybrid dry-wet interdune deposition. In *Precambrian aeolian systems: Galho do Miguel formation, SE Brazil: Sedimentary geology* (Vol. 425).

Meyer, M. J., Milliken, R. E., Stack, K. M., Edgar, L. A., Rampe, E. B., Turner, M. L., et al. (2025). Geological context and significance of the clay-sulfate transition region in Mount Sharp, Gale crater, Mars: An integrated assessment based on orbiter and rover data. *Geological Society of America Bulletin*, *137*(1–2), 82–115. https://doi.org/10.1130/b37355.1

Milliken, R. E., Ewing, R. C., Fischer, W. W., & Hurowitz, J. (2014). Wind-blown sandstones cemented by sulfate and clay minerals in Gale crater, Mars. *Geophysical Research Letters*, *41*(4), 1149–1154. https://doi.org/10.1002/2013gl059097

Milliken, R. E., Grotzinger, J. P., & Thomson, B. J. (2010). Paleoclimate of Mars as captured by the stratigraphic record in Gale crater. *Geophysical Research Letters*, *37*(4). https://doi.org/10.1029/2009gl041870

Mondro, C. A., Grotzinger, J., Fedo, C. M., Lamb, M. P., Gupta, S., Dietrich, W. E., et al. (2025). Depositional environment of the Amapari Marker Band: Rising water levels formed kilometer-scale lake in Gale crater, Mars. *Journal of Geophysical Research: Planets*. https://doi.org/10.1029/2024JE008606

Mondro, C. A., Fedo, C. M., Grotzinger, J. P., Lamb, M. P., Gupta, S., Dietrich, W. E., et al. (2025). Wave ripples formed in ancient, ice-free lakes in Gale crater, Mars. *Science Advances*, *11*(3), eadr0010. https://doi.org/10.1126/sciadv.adr0010

Mountney, N. P. (2006a). *Eolian facies models, facies models revisited*. SEPM Society for Sedimentary Geology.

Mountney, N. P. (2006b). Periodic accumulation and destruction of aeolian erg sequences in the Permian Cedar Mesa Sandstone, White Canyon, southern Utah, USA. *Sedimentology*, *53*(4), 789–823. https://doi.org/10.1111/j.1365-3091.2006.00793.x

Mountney, N. P. (2012). A stratigraphic model to account for complexity in aeolian dune and interdune successions. *Sedimentology*, *59*(3), 964–989. https://doi.org/10.1111/j.1365-3091.2011.01287.x

Mountney, N. P., & Howell, J. (2000). Aeolian architecture, bedform climbing and preservation space in the Cretaceous Etjo formation, NW Namibia. *Sedimentology*.

Mountney, N. P., & Jagger, A. (2004). Stratigraphic evolution of an aeolian erg margin system: The Permian Cedar Mesa Sandstone, SE Utah, USA. *Sedimentology*, *51*(4), 713–743. https://doi.org/10.1111/j.1365-3091.2004.00646.x

Mountney, N. P., & Russell, A. J. (2009). Aeolian dune-field development in a water table-controlled system: Skeidararsandur, Southern Iceland. *Sedimentology*, *56*(7), 2107–2131. https://doi.org/10.1111/j.1365-3091.2009.01072.x

Mountney, N. P., & Thompson, D. B. (2002). Stratigraphic evolution and preservation of aeolian dune and damp/wet interdune strata: An example from the Triassic Helsby Sandstone formation, Cheshire Basin, UK. *Sedimentology*, *49*(4), 805–833. https://doi.org/10.1046/j.1365-3091.2002.00472.x

Murton, J. B., Opel, T., Toms, P., Wood, J., Boxleitner, K., Savvinov, G., et al. (2025). Preliminary paleoenvironmental analysis and luminescence dating of upper Middle Pleistocene permafrost deposits of the Ulakhan Sular formation, Adycha River, east Siberia. *Quaternary Research*, *124*, 1–25. https://doi.org/10.1017/qua.2024.36

Nickling, W. G. (1984). The stabilizing role of bonding agents on the entrainment of sediment by wind. *Sedimentology*, *31*(1), 111–117. https://doi.org/10.1111/j.1365-3091.1984.tb00726.x

O'Connell-Cooper, C. D., Thompson, L. M., Spray, J. G., VanBommel, S. J., Berger, J. A., Gellert, R., et al. (2025). APXS derived geochemistry of shallow water lens bodies within the Mirador formation, Gale crater, Mars—Evidence for intermittent wet periods and implications for the water record. *Journal of Geophysical Research: Planets*, *130*(11), e2025JE009001. https://doi.org/10.1029/2025je009001

Pécsi, M. (1990). Loess is not just the accumulation of dust. *Quaternary International*, *7*, 1–21. https://doi.org/10.1016/1040-6182(90)90034-2

Putnam, A. R., & Palucis, M. C. (2021). The hydrogeomorphic history of garu crater: Implications and constraints on the timing of large late-stage Lakes in the Gale crater region. *Journal of Geophysical Research-Planets*, *126*(5), e2020JE006688. https://doi.org/10.1029/2020je006688

Rankin, A., Maimone, M., Biesiadecki, J., Patel, N., Levine, D., & Toupet, O. (2020). Driving curiosity: Mars rover mobility trends during the first seven years. In *Proceedings 2020 IEEE aerospace conference* (pp. 1–19). IEEE.

Rapin, W., Dromart, G., Clark, B., Schieber, J., Kite, E., Kah, L., et al. (2023a). Sustained wet–dry cycling on early Mars. *Nature*, *620*(7973), 299–302. https://doi.org/10.1038/s41586-023-06220-3

Rapin, W., Dromart, G., Rubin, D., Le Deit, L., Mangold, N., Edgar, L. A., et al. (2021). Alternating wet and dry depositional environments recorded in the stratigraphy of Mount Sharp at Gale crater, Mars: Geology. *Geology*, *49*(7), 842–846. https://doi.org/10.1130/g48519.1

Rapin, W., Dromart, G., Schieber, J., Clark, A. H., Kah, L. C., Rubin, D., et al. (2023b). *Aridification sequence and formation of sulfates in Aeolis Mons, Gale crater, FAIRPLAY Workshop*. European Space Research and Technology Centre.

Rapin, W., Ehlmann, B. L., Dromart, G., Schieber, J., Thomas, N. H., Fischer, W. W., et al. (2019). An interval of high salinity in ancient Gale crater lake on Mars. *Nature Geoscience*, *12*(11), 889–895. https://doi.org/10.1038/s41561-019-0458-8

Rapin, W., Loche, M., Beck, P., Meslin, P.-Y., Caravaca, G., Magnin, T., et al. (2025). Siderite-rich laminae at the marker band contact in Gale crater. In *Proceedings 56th lunar and planetary science conference* (p. 2127).

Rivera-Hernández, F., Sumner, D. Y., Mangold, N., Stack, K. M., Forni, O., Newsom, H., et al. (2019). Using ChemCam LIBS data to constrain grain size in rocks on Mars: Proof of concept and application to rocks at Yellowknife Bay and Pahrump Hills, Gale crater. *Icarus*, *321*, 82–98. https://doi.org/10.1016/j.icarus.2018.10.023

Rice, M. S., Gupta, S., Treiman, A. H., Stack, K. M., Calef, F., Edgar, L. A., et al. (2017). Geologic overview of the Mars Science Laboratory rover mission at the Kimberley, Gale crater, Mars. *Journal of Geophysical Research-Planets*, *122*(1), 2–20. https://doi.org/10.1002/2016je005200

Roberts, A. L., Gupta, S., Banham, S. G., Cowart, A., Edgar, L. A., Rapin, W., et al. (2025). Paleo-Scours within the layered sulfate-bearing unit at Gale crater, Mars: Evidence for intense wind erosion. *Journal of Geophysical Research: Planets*, *130*(5), e2024JE008680. https://doi.org/10.1029/2024je008680

Roberts, A. L., Gupta, S., Dietrich, W. E., Edgar, L., Rapin, W., Banham, S., et al. (2023). What depositional processes and palaeoenvironments formed the layered sulfate unit in Gale crater Mars. In *54th lunar and planetary science conference: The woodlands, Texas*.

Rodríguez-López, J. P., Meléndez, N., de Boer, P. L., & Soria, A. R. (2010). The action of wind and water in a mid-cretaceous subtropical erg-margin system close to the Variscan Iberian Massif, Spain. *Sedimentology*, *57*(5), 1315–1356. https://doi.org/10.1111/j.1365-3091.2010.01147.x

Rodríguez-López, J. P., Wu, C., Vishnivetskaya, T. A., Murton, J. B., Tang, W., & Ma, C. (2022). Permafrost in the Cretaceous supergreenhouse. *Nature Communications*, *13*(1), 7946. https://doi.org/10.1038/s41467-022-35676-6

Rubin, D. (1987). Cross-bedding, bedforms, and paleocurrents, Tulsa, Oklahoma, U. S. A, Society of Economic paleontologists and mineralogists, concepts in sedimentology and paleontology.
Rubin, D. M., & Hunter, R. E. (1982). Bedform climbing in theory and nature. *Sedimentology*, *29*(1), 121–138. https://doi.org/10.1111/j.1365-3091.1982.tb01714.x
Schieber, J., Bohacs, K., Coleman, M., Bish, D., Reed, M., Thompson, L., et al. (2025). Mostly aeolian or lacustrine? A sedimentary and petrographic perspective on the depositional setting of upper contigo through Chenapau strata (Mirador formation), Gale crater, Mars. *LPI Contributions*, *3090*, 1150.
Schieber, J., Bohacs, K. M., Bish, D., Coleman, M., Thompson, L., Rapin, W., & Yawar, Z. (2024). Evaporitic–lacustrine mudstone laminites and prodelta mudlobes – Continuity and change in the Hartmann's Valley interval, Murray formation, Gale crater, Mars. *Sedimentology*, *71*(7), 2071–2118. https://doi.org/10.1111/sed.13242
Schieber, J., Bohacs, K. M., Coleman, M., Bish, D., Reed, M. H., Thompson, L., et al. (2022). Mars is a mirror–understanding the Pahrump Hills mudstones from a perspective of Earth analogues. *Sedimentology*, *69*(6), 2371–2435. https://doi.org/10.1111/sed.13024
Schneider, C. A., Rasband, W. S., & Eliceiri, K. W. (2012). NIH Image to ImageJ: 25 years of image analysis. *Nature Methods*, *9*(7), 671–675. https://doi.org/10.1038/nmeth.2089
Schwan, J. (1988). The structure and genesis of Weichselian to early hologene aeolian sand sheets in western Europe. *Sedimentary Geology*, *55*(3–4), 197–232. https://doi.org/10.1016/0037-0738(88)90132-7
Seeger, C., & Grotzinger, J. (2024). Diagenesis of the clay-sulfate stratigraphic transition, Mount sharp group, Gale crater, Mars. *Journal of Geophysical Research: Planets*, *129*(12), e2024JE008531. https://doi.org/10.1029/2024je008531
Sheppard, R. Y., Thorpe, M. T., Fraeman, A. A., Fox, V. K., & Milliken, R. E. (2021). Merging perspectives on secondary minerals on Mars: A review of Ancient water-rock interactions in Gale crater inferred from orbital and In-Situ observations. *Minerals*, *11*(9), 986. https://doi.org/10.3390/min11090986
Simplicio, F., & Basilici, G. (2015). Unusual thick eolian sand sheet sedimentary succession: Paleoproterozoic Bandeirinha formation, Minas Gerais. *Brazilian Journal of Geology*, *45*(suppl 1), 3–11. https://doi.org/10.1590/2317-4889201530133
Simpson, E. L., & Loope, D. B. (1985). Amalgamated interdune deposits, White Sands, New Mexico. *Journal of Sedimentary Research*, *55*(3), 361–365.
Smiley, T. (1955). Varve studies. *Geochronology*, *2*, 135–150.
Smith, D. E., Zuber, M. T., Frey, H. V., Garvin, J. B., Head, J. W., Muhleman, D. O., et al. (2001). Mars Orbiter Laser Altimeter: Experiment summary after the first year of global mapping of Mars. *Journal of Geophysical Research*, *106*(E10), 23689–23722. https://doi.org/10.1029/2000je001364
Smyth, T. A. G., Hesp, P. A., Walker, I. J., Wasklewicz, T., Gares, P. A., & Smith, A. B. (2019). Topographic change and numerically modelled near surface wind flow in a bowl blowout. *Earth Surface Processes and Landforms*, *44*(10), 1988–1999. https://doi.org/10.1002/esp.4625
Stack, K. M., Edwards, C. S., Grotzinger, J. P., Gupta, S., Sumner, D. Y., Calef, F. J., et al. (2016). Comparing orbiter and rover image-based mapping of an ancient sedimentary environment, Aeolis Palus, Gale crater, Mars. *Icarus*, *280*, 3–21. https://doi.org/10.1016/j.icarus.2016.02.024
Stack, K. M., Grotzinger, J. P., Lamb, M. P., Gupta, S., Rubin, D. M., Kah, L. C., et al. (2019). Evidence for plunging river plume deposits in the Pahrump Hills member of the Murray formation, Gale crater, Mars. *Sedimentology*, *66*(5), 1768–1802. https://doi.org/10.1111/sed.12558
Stein, N. T., Quinn, D. P., Grotzinger, J. P., Fedo, C. M., Ehlmann, B. L., Stack, K. M., et al. (2020). Regional structural orientation of the Mount Sharp Group revealed by in situ dip measurements and stratigraphic correlations on the vera rubin ridge. *Journal of Geophysical Research-Planets*, *125*(5), e2019JE006298. https://doi.org/10.1029/2019je006298
Thompson, L. M., Spray, J. G., VanBommel, S. J., O'Connell-Cooper, C. D., Berger, J. A., Gellert, R., et al. (2024). Amapari marker band, Gale crater, Mars: Event horizon with highest bedrock iron and zinc concentrations detected by curiosity's alpha particle x-ray spectrometer. *Geophysical Research Letters*, *51*(23), e2024GL111113. https://doi.org/10.1029/2024gl111113
Thomson, B. J., Bridges, N. T., Milliken, R., Baldridge, A., Hook, S. J., Crowley, J. K., et al. (2011). Constraints on the origin and evolution of the layered mound in Gale crater, Mars using Mars Reconnaissance Orbiter data. *Icarus*, *214*(2), 413–432. https://doi.org/10.1016/j.icarus.2011.05.002
Trewin, N. H. (1993). Mixed aeolian sandsheet and fluvial deposits in the Tumblagooda Sandstone. *Geological Society, London, Special Publications*, *73*, 219–230. https://doi.org/10.1144/gsl.sp.1993.073.01.13
Turner, M., & Lewis, K. (2023). Geologic structure of the Vera Rubin Ridge, Gale crater, Mars. *Journal of Geophysical Research-Planets*, *128*(9), e2022JE007237. https://doi.org/10.1029/2022je007237
Vasavada, A. R. (2022). Mission overview and scientific contributions from the Mars science laboratory curiosity rover after eight years of surface operations. *Space Science Reviews*, *218*(3), 14. https://doi.org/10.1007/s11214-022-00882-7
Veiga, G. D., & Spalletti, L. A. (2007). The Upper Jurassic (Kimmeridgian) fluvial-aeolian systems of the southern Neuquen Basin, Argentina. *Gondwana Research*, *11*(3), 286–302. https://doi.org/10.1016/j.gr.2006.05.002
Veiga, G. D., Spalletti, L. A., & Flint, S. (2002). Aeolian/fluvial interactions and high-resolution sequence stratigraphy of a non-marine lowstand wedge: The Avile Member of the Agrio formation (Lower Cretaceous), central Neuquen Basin, Argentina. *Sedimentology*, *49*(5), 1001–1019. https://doi.org/10.1046/j.1365-3091.2002.00487.x
Ventra, D., Rodríguez-López, J. P., & de Boer, P. L. (2017). Sedimentology and preservation of aeolian sediments on steep terrains: Incipient sand ramps on the Atacama coast (northern Chile). *Geomorphology*, *285*, 162–185. https://doi.org/10.1016/j.geomorph.2017.02.016
Virtanen, P., Gommers, R., Oliphant, T. E., Haberland, M., Reddy, T., Cournapeau, D., et al. (2020). SciPy 1.0: Fundamental algorithms for scientific computing in Python. *Nature Methods*, *17*(3), 261–272. https://doi.org/10.1038/s41592-019-0686-2
Walker, R. G., & Middleton, G. V. (1977). *Facies models 9. Eolian sands*. Geoscience Canada.
Watkins, J. A., Grotzinger, J. P., Stein, N. T., Banham, S. G., Gupta, S., Rubin, D. M., et al. (2022). Burial and exhumation of sedimentary rocks revealed by the base stimson erosional unconformity, Gale crater, Mars. *Journal of Geophysical Research-Planets*, *127*(7), e2022JE007293. https://doi.org/10.1029/2022je007293
Weitz, C. M., Lewis, K., Kite, E. S., Dietrich, W. E., Thompson, L. M., O'connell-cooper, C., et al. (2023). The Marker Band in Gale crater. In *54th lunar and planetary science conference: The woodlands, Texas, United States*.
Weitz, C. M., Lewis, K. W., Bishop, J. L., Thomson, B. J., Arvidson, R. E., Grant, J. A., et al. (2022). Orbital observations of a marker horizon at Gale crater. *Journal of Geophysical Research: Planets*, *127*(4), e2022JE007211. https://doi.org/10.1029/2022je007211
Williams, R. M. E., Grotzinger, J. P., Dietrich, W. E., Gupta, S., Sumner, D. Y., Wiens, R. C., et al. (2013). Martian fluvial conglomerates at Gale crater. *Science*, *340*(6136), 1068–1072. https://doi.org/10.1126/science.1237317

Yingst, R., Cowart, A., Kah, L., Gupta, S., Stack, K., Fey, D., et al. (2023). Depositional and diagenetic processes of martian lacustrine sediments as revealed at Pahrump Hills by the Mars Hand Lens Imager, Gale crater, Mars. *Journal of Geophysical Research: Planets*, *128*(5), e2022JE007394. https://doi.org/10.1029/2022je007394

Yingst, R. A., Edgett, K. S., Kennedy, M. R., Krezoski, G. M., McBride, M. J., Minitti, M. E., et al. (2016). MAHLI on Mars: Lessons learned operating a geoscience camera on a landed payload robotic arm. *Geoscientific Instrumentation, Methods and Data Systems*, *5*(1), 205–217. https://doi.org/10.5194/gi-5-205-2016

Zhou, D. Y., Turner, M. L., Rapin, W., Schieber, J., Roberts, A. L., Cowart, A. C., et al. (2025). How does topography affect wind abrasion on Mars? Recently observed shifts in ventifact orientation at Gale crater. *Icarus*, *437*, 116605. https://doi.org/10.1016/j.icarus.2025.116605